Investigation of Flow and Local Scour Characteristics around Permeable WSDOT Dolotimber Engineered Logjams (ELJ)

WA-RD 821.2

A.N. (Thanos) Papanicolaou
Micah A. Wyssmann
Adam Merook
Sevin Mohammadi

August 2018

Washington State
Department of Transportation
Office of Research & Library Services

WSDOT Research Report

18-11-0489

INVESTIGATION OF FLOW AND LOCAL SCOUR CHARACTERISTICS AROUND PERMEABLE WSDOT DOLOTIMBER ENGINEERED LOGJAMS (ELJ)

FINAL REPORT

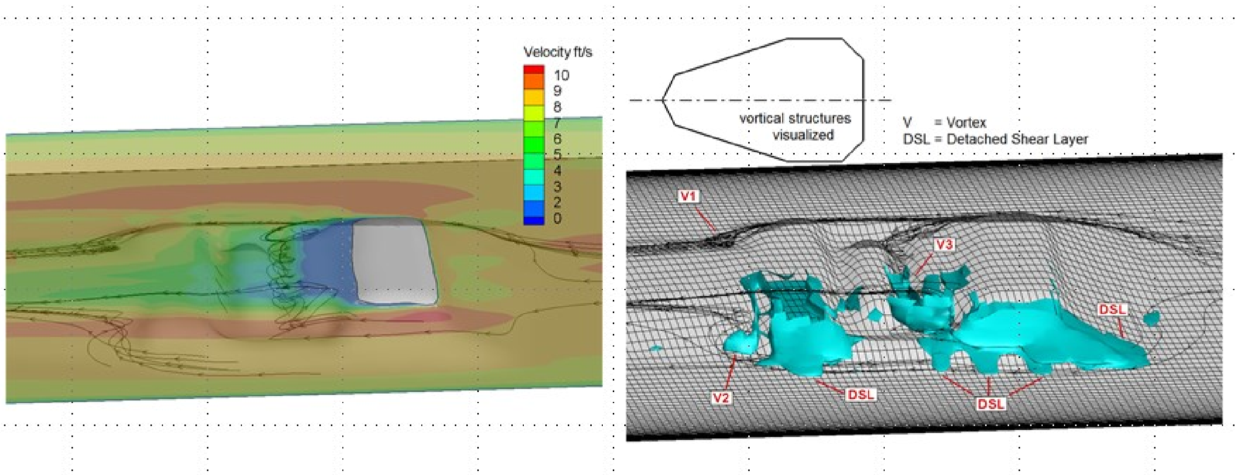

Submitted to:
Washington State Department of Transportation, Research Program
Washington State Highway Research Board
310 Maple Park Ave SE
Olympia, WA 98504-7329

Submitted by:
Dr. Thanos Papanicolaou
Hydraulics and Sedimentation Laboratory (HSL)
Department of Civil and Environmental Engineering
College of Engineering
The University of Tennessee
Knoxville, Tennessee 37996
August 2018

About the University of Tennessee

The University of Tennessee's College of Engineering was established in 1838 and has an on-going commitment to excellence in scientific research and engineering education. However, it has recently experienced significant growth in enrollment, faculty, and national prominence. Enrollment has increased by nearly 50% since 2007, while the college faculty has added ten prestigious Governor's Chairs, eight endowed fellowships and professorships, and one endowed chair since 2009. The college's national rankings have also improved with both the undergraduate and graduate programs currently being ranked 32nd in the nation. Along with this growth, the new John D. Tickle Building, which houses the Department of Civil and Environmental Engineering (CEE), was dedicated in October 2013 and the Hydraulics and Sedimentation Lab (HSL) in May 2015. The Tickle building has 24 laboratories, three conventional classrooms, one lecture hall, three student work spaces, and 63 faculty and graduate student offices, along with a high-bay area, where environmental and geotechnical experiments are performed. HSL provides advanced instrumentation and infrastructure, including 4 flumes, for fundamental research in the areas of water resources, environmental fluid mechanics, and watershed processes.

Disclaimer

The opinions, findings, and conclusions expressed in this report are those of the authors and not necessarily those of the sponsors. The views and conclusions contained in this document are those of the authors and should not be interpreted as necessarily representing the official policies, either expressed or implied, of the Washington State Department of Transportation.

The sponsors assume no liability for the contents or use of the information contained in this document. This report does not constitute a standard, specification, or regulation. Additionally, the sponsors do not endorse products or manufacturers mentioned in this report. Trademarks or manufacturers' names appear in this report only because they are considered essential to the objective of the document.

Non-Discrimination Statement

The University of Tennessee does not discriminate on the basis of race, color, age, religion, national origin, sexual orientation, gender identity, sex, marital status, disability, or status as a U.S. veteran. Inquiries can be directed to the Office of Equity and Diversity at the University of Tennessee, (865) 974-2498.

Technical Report Documentation Page

1. REPORT NO. WA-RD 821.2	2. GOVERNMENT ACCESSION NO.	3. RECIPIENT'S CATALOG NO.

4. TITLE AND SUBTITLE Investigation of Flow and Local Scour Characteristics around Permeable WSDOT Dolotimber Engineered Logjams (ELJ)	5. REPORT DATE August 2018 6. PERFORMING ORGANIZATION CODE
7. AUTHOR(S) Prof. A.N. (Thanos) Papanicolaou, Micah A. Wyssmann, Adam Merook, Sevin Mohammadi	8. PERFORMING ORGANIZATION REPORT NO.
9. PERFORMING ORGANIZATION NAME AND ADDRESS Hydraulics and Sedimentation Laboratory (HSL) Department of Civil and Environmental Engineering 2021 Stephenson Drive The University of Tennessee Knoxville, TN 37916-4514	10. WORK UNIT NO. 11. CONTRACT OR GRANT NO. GCB 1930
12. SPONSORING AGENCY NAME AND ADDRESS Research Office Washington State Department of Transportation Transportation Building, MS 7370 Olympia, Washington 98504-7370 Lu Saechao, Project Manager, (360) 705-7260 Julie Heilman, Technical Monitor	13. TYPE OF REPORT AND PERIOD COVERED Final Report 14. SPONSORING AGENCY CODE
15. SUPPLEMENTARY NOTES	

16. ABSTRACT

Engineered logjams (ELJs) are permeable flow deflection structures that project out from the streambank and are used to stabilize streambanks, protect roadways, and improve aquatic habitat. Dolotimber ELJs are constructed from interlocking large woody material and concrete dolo components to provide optimal performance in terms of structural stability and ecological benefits. The results from this report focus on two primary aspects of scour around ELJs. Part one focuses on the repeatable equilibrium scour characteristics determined through extensive experimentation. The conical scour hole shape extending from the ELJ structure nose is highlighted. Equilibrium scour characteristics are compared with existing predictive methods and are used to develop new physically-based, semi-empirical formulas that consider the effects of both sediment non-uniformity and structure porosity on scour in addition to flow magnitude. Part two focuses on the complex characteristics of scour and flow co-evolution, which have been monitored directly for the first time around permeable structures in a gravel bed. The decay function for relating flow and scour co-evolution is overviewed and developed using this unique data. Also Large Eddy Simulation (LES) numerical modeling for comparable Reynolds numbers with those found in field conditions was employed to visualize the complex three-dimensional flow features generated in the presence of an apex dolotimber ELJ structure.

17. KEY WORDS Permeable dolotimber engineered logjam (ELJ) structures, structure porosity, scour evolution, bed shear stress decay function, scour depth, scour volume.	18. DISTRIBUTION STATEMENT No restrictions.

19. SECURITY CLASSIF. (of this report) None	20. SECURITY CLASSIF. (of this page) None	21. NO. OF PAGES	22. PRICE NA

INVESTIGATION OF FLOW AND LOCAL SCOUR CHARACTERISTICS AROUND PERMEABLE WSDOT DOLOTIMBER ENGINEERED LOGJAMS (ELJ)

Final Report

August 2018

Principal Investigator
Thanos Papanicolaou
Professor, Henry Goodrich Chair of Excellence
Department of Civil and Environmental Engineering
The University of Tennessee
Knoxville, TN 52242

Sponsored by
The Washington State Department of Transportation

A report prepared from
The Hydraulics and Sedimentation Laboratory (HSL)
Department of Civil and Environmental Engineering
The University of Tennessee, Knoxville
Knoxville, TN 52242
Phone: (865) 974-7773
http://hsl.engr.utk.edu

Acknowledgements

The researchers gratefully acknowledge the technical assistance and support from the Technical Advisory Committee, and especially the contributions of the following people and companies during the planning, development, and execution of this project:

Julie Heilman	Washington State Dept. of Transportation, Project Technical Monitor
Casey Kramer	now with Northwest Hydraulic Consultants, formerly of Washington State Dept. of Transportation and identified the need for gravel bed scour equations in 2012 as State Hydraulics Engineer
Lu Saechao	formerly Washington State Dept. of Transportation
Garrett Jackson	Washington State Dept. of Transportation
Rhonda Brooks	Director of Research, Washington State Dept. of Transportation
Jim Park†	Washington State Dept. of Transportation
Achilleas G. Tsakiris	Northwest Hydraulic Consultants, former UTK research associate
Theodoros Kyriakopoulos	Graduate Research Assistant at UTK
Caroline Stephens	Undergraduate Research Assistant at UTK
Brandi Hawkins	Tennessee Department of Transportation, former UTK Graduate Research Assistant

Harrison Aggregates in Knoxville, TN

Technicians Andy Baker, Larry Roberts, Ken Thomas and IT person Jonathan Turnmire

http://www.seatek.com/

Organization of this Report

This report consists of two parts. The first part focuses on the repeatable characteristics of equilibrium scour patterns around ELJs in gravel bed rivers at both clear water and live bed scour conditions. The scour hole is conical in shape, extending away from the ELJ toe. A process – based parameterized formula applicable for scour predictions around permeable ELJ structures in gravel bed rivers is developed. The second part focuses on the complex characteristics of scour and flow co-evolution around ELJs. From the temporal evolution of scour and flow a decay function was developed to characterize scour around the ELJs with a gravel bed. Also, numerical modeling was employed to visualize three-dimensional flow structures that develop around an apex ELJ structure.

Cover picture

Modeling results of the isovel streamline map and vortices around ELJ 5

Table of Contents

1. Introduction

1.1 Definition and Use of Engineered Logjams

Streambank protection is of crucial importance in locations where bank erosion can result in channel migration therefore jeopardizing nearby infrastructure (roads, levees, etc.). Traditional streambank protection methods include the use of structural installation measures (Frissell and Nawa, 1992; Rosgen, 2001; Thompson, 2002), extensive vegetative plantings (Fetherston et al., 1995; Justice et al., 2017; Schultz et al., 1995), and soil bioengineering (Eubanks and Meadows, 2002; Finney, 1993; Lewis 2000). Of these practices, the most common is the application of riprap revetments on streambank surfaces to protect existing substrate material and dissipate flow erosive energy (Blodgett, 1986; Robinson, 2002; Shields et al., 1995).

When considering potential streambank protection design options, there are multiple shortcomings of traditional methods that should be considered. In the installation process, some designs require the driving of piles or other invasive techniques, which can introduce excessive noise to the aquatic system and impact underwater species (Bagočius, 2015; Reyff, 2017). Moreover, the installation process for some designs requires channel dewatering or diversion, which can affect seasonal spawning runs or migratory behavior of fish (USDA, 2007a). Once installed, some engineered designs that utilize primarily non-native materials (i.e., materials not naturally found at stream sites) may exhibit different resonance properties from natural riparian vegetation, which could create increased stress on fish and/or may affect fish habitat selection (Amoser & Ladich, 2005; Smith, 2004; Huijbers et al., 2012). Considering the economic costs of streambank protection design alternatives, some of the commonly preferred designs have proved quite expensive when considering their entire lifetime because of the need for repeated repairs after seasonal high flow events (Abbe et al., 1997; Cardno Entrix, 2011). In addition, failures of streambank protection measures at large flows can lead to excessive erosion, increased turbidity, and destabilization of river beds that are important to the spawning cycle of egg-laying fish (Allen and Flecker, 1993; Kimmerer and Allan, 1982; Meffe, 1984; Montgomery, 1996; USDA, 2007b).

In an attempt to mimic natural rivers and utilize “native” materials for designing streambank protection measures, a growing number of researchers and practitioners have developed design alternatives using wooden components in engineered logjams (ELJs) (Abbe et al., 1997; Bolton et al., 1998; Castro and Sampson, 2001). ELJs employ interlocking components of wood and root wads (referred to as large woody materials, LWM), as well as gravel and thatch. ELJs can also have positive ecological effects by increasing the quantity of interstitial spacing available for biological growth, by enhancing hyporheic flow exchange, and by providing improved habitat diversity and complexity for fish (Brooks et al., 2001; Cedarholm et al., 1997; D’Aoust and Millar, 1999; House and Crispin, 1990; Lautz et al., 2006; Pess et al., 2012). However, a downside to ELJ designs is that they typically require installation with driven piles or in dewatered channels (D’Aoust and Millar, 2000), which can cause negative ecological impacts.

In an attempt to employ the best facets of multiple design alternatives, stream restoration practitioners have partnered with state departments and federal research initiatives to improve the design of traditional ELJs (i.e., those constructed using only natural materials) by integrating LWM with concrete “dolos” to create multi-component dolotimber ELJs. A standard dolo

(Figure 1.1) is jack-like structure weighing over 8 tons and made of unreinforced pre-cast concrete; they are self-settling, interlocking units that have arm-like protrusions, which extend up to 8 feet (Abbe et al., 2011). Due to their immense weight and arm-like protrusions, dolos can be easily combined and interlocked with logs, root wads, and cobble ballasts to create a stable structure that can allow a complex riparian habitat to form within the interstitial spacing (Figure 1.2). The surface of the concrete dolos can also be roughened to imitate tree bark in order to further promote microbiological growth and diverse biota. Utilizing these structural components in a modular manner allows for installation without invasive construction practices and has been shown to yield substantial cost-savings related to materials, time, and permitting efforts (Abbe et al., 1997). Overall, dolotimber ELJs can thus provide advantages in terms of multiple design assessment criteria, such as structural stability, ecological benefits and economic cost.

Dolotimber ELJs can be constructed with multiple design geometries and placements within the channel in order to meet different project goals. The following are three common design types: bank revetment ELJ structures, bank-attached deflector ELJs, and apex ELJs (Abbe and Montgomery, 2003; Brooks et al., 2006). Bank revetment ELJ structures are constructed along a streambank section with staggered and layered components in such a way as to cover the bankline and protect it against erosion. Bank-attached deflector ELJs protrude out from the bankline in order to deflect the flow toward the center of the channel and reduce the erosive energy at the bank. Apex ELJs are constructed in-stream and surrounded on all sides by the channel flow.

The Washington State Department of Transportation (WSDOT), in coordination with Native American entities, local governments, and conservation groups, has installed ELJs for streambank protection and the improvement of aquatic habitat at multiple locations along highways and at river crossings. Examples include installations in the Lower Cle Elum River to recruit more natural wood downstream of Cle Elum Dam (Kittitas Conservation Trust, 2008), the Hoh River bordering US 101 to provide bank stabilization (Ward, 2006), the South Fork Nooksack to aid Chinook salmon spawning habitat restoration (Washington State Recreation and Conservation Office; RCO, 2011), the Deschutes River to restore aquatic habitat complexity lost by historic modification (RCO, 2012), the Lower Elwha River to restore critical salmon habitat (RCO, 2000), and the Cowlitz River to combat bank retreat (Hall and Moler, 2006). These installations represent the growing development and implementation of ELJ construction standards and best management practices, evolving from a predominantly “experimental” methodology to an established streambank protection practice that may be useful in a number of river restoration applications.

Figure 1.1. Standard concrete dolo, with textured surface recreating natural roughness. Human for scale. (WSDOT, 2011)

Figure 1.2. Dolotimber ELJ revetment with inclusion of logs and other LWM (WSDOT, 2011).

1.2 Interactions of ELJ Structures and Flow

The flow characteristics around bank-attached deflector ELJs are similar to those around other bank-attached hydraulic structures, which have been investigated with different shapes, compositions and porosities (e.g., Bennett et al., 2015; Koken & Constantinescu, 2014; Leu et al., 2008). These studies have established the primary flow regions around both impermeable structures and porous ELJs to include the main core, the shear layer, and the wake region (Fox et al., 2005a; Xu and Liu, 2017). Moreover, the well-defined microstructures that occur around impermeable bridge abutments provide a useful reference point for understanding flow characteristics around partially submerged deflector ELJs (Barbhuiya and Dey, 2003; 2004;

Koken and Constantinescu, 2014). These microstructures are described as a system of vortices that develop at the upstream, tip, and lee locations around the structure. The back eddies form on the upstream face of the structure as flow is deflected downward towards the bed (Papanicolaou et al., 2018). This diving energy further merges with the flow accelerating around the structure i.e., along the shear layer, to form the primary/horseshoe vortices in the main core region. These flow structures also cause jettisoned stream tubes focused at the structure toe, which lead to a local bed shear stress amplification by a factor of 3-5 and an associated local scour potential increase (Ahmed and Rajaratnam, 2000; Coleman at al., 2003; Kothyari and Raju, 2001; Whitehouse, 1997). Secondary vortices may also occur outside of the primary vortex where the constricted streamlines near the structure interact with the bulk streamlines further into the channel (Melville and Coleman, 2000). Downstream of the structure, wake vortices are prominent because flow is separated at both the upstream and downstream corners of the abutment (Barbhuiya and Dey, 2004). An illustration of these microstructures forming near an impermeable abutment can be seen in Figure 1.3.

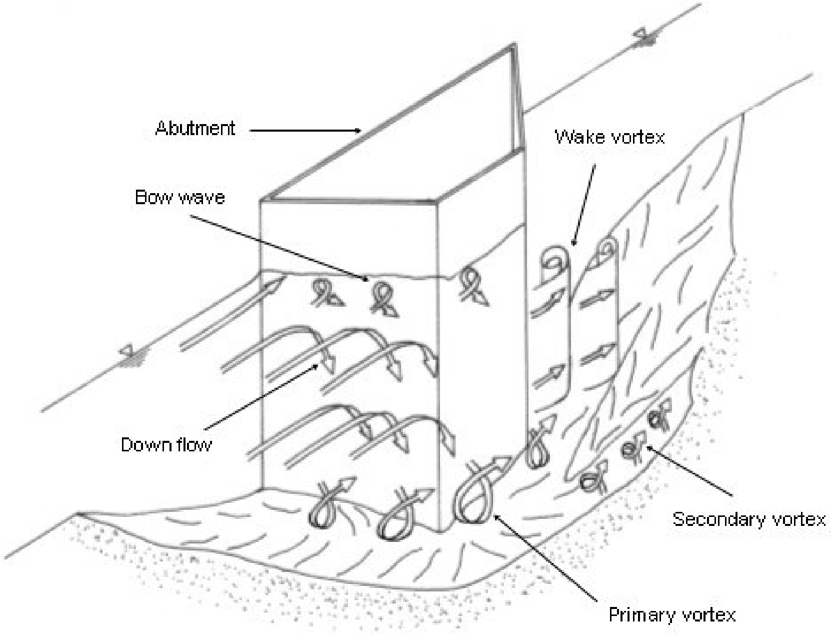

Figure 1.3. Perspective view illustration of developed vortical microstructures near a bridge abutment (after Kwan, 1988)

Because of the in-stream placement of apex ELJs, their surrounding flow characteristics have multiple differences from those illustrated in Figure 1.3 for a bank-attached structure. At the upstream face of partially submerged bar apex ELJs, a downward flow deflection occurs and can lead to a backward flow within this region. A flow stagnation point also occurs upstream of the ELJ face, from which the flow diverges to travel around the two sides of the ELJ face. At the upstream face and upstream flanks of the ELJ, an elevated shear stress with associated scour potential is typically observed (Jackson et al., 2013; Kirkil and Constantinescu, 2009). A large wake recirculation region also forms downstream of apex ELJs. An illustration of the flow characteristics forming around an apex ELJ is provided in Figure 1.4.

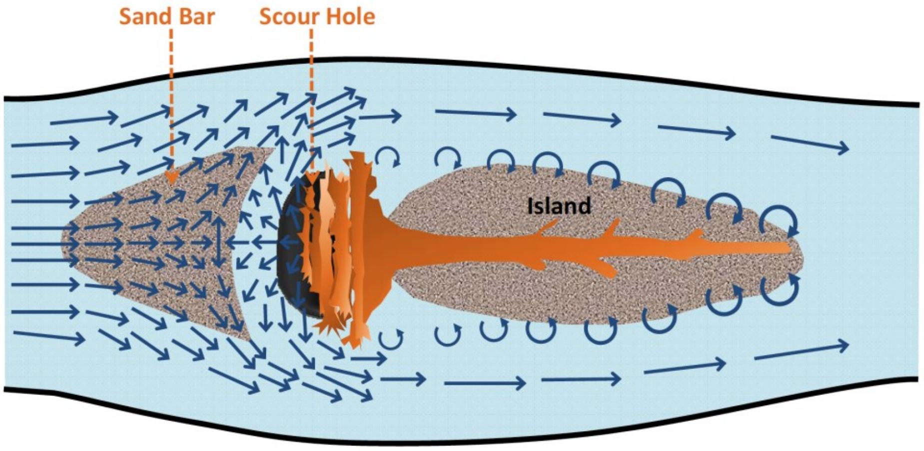

Figure 1.4. Plan view illustration of the flow characteristics forming around an apex ELJ (after Jackson et al., 2013)

Because of their unique features relative to other structures of similar geometry, ELJs can stimulate important modifications the previously described flow characteristics. The high porosity of ELJs, which can be higher than 70%, is one such feature that can affect the flow field around ELJs (WSDOT, 2011). This high porosity promotes percolating flow through the structure and leads to a decrease in the magnitude of backwater effects (Papanicolaou et al., 2004; Papanicolaou et al., 2018). By reducing backwater, porosity increase is also associated with lower shear stresses at the toe of deflector structures, which leads to decreased scour potential (Manners et al., 2007). The increased local roughness at the surface of ELJs associated with protruding dolotimber arms and log extensions may also modify the surrounding flow field (Abbe et al., 1997; Cardno Entrix, 2011; Shields and Gippel, 1995). Specifically, these roughness features can disrupt localized acceleration in the ELJ vicinity and may inhibit the erosive power of important vortical structures such as the primary/horseshoe vortex (Koken and Constantinescu, 2014).

The effects of ELJ porosity and internal structure geometry to the surrounding flow is illustrated in Figure 1.5, which shows the vortices around three different structure types: one with fully resolved internal ELJ geometry with interlocking logs, one comprised of a simple porous media, and one with a solid, impermeable barrier. Figure 1.5 thus illustrates the effects that ELJ structure permeability has on the complex flow characteristics that develop at the ELJ toe and drive scour evolution within the scour zone.

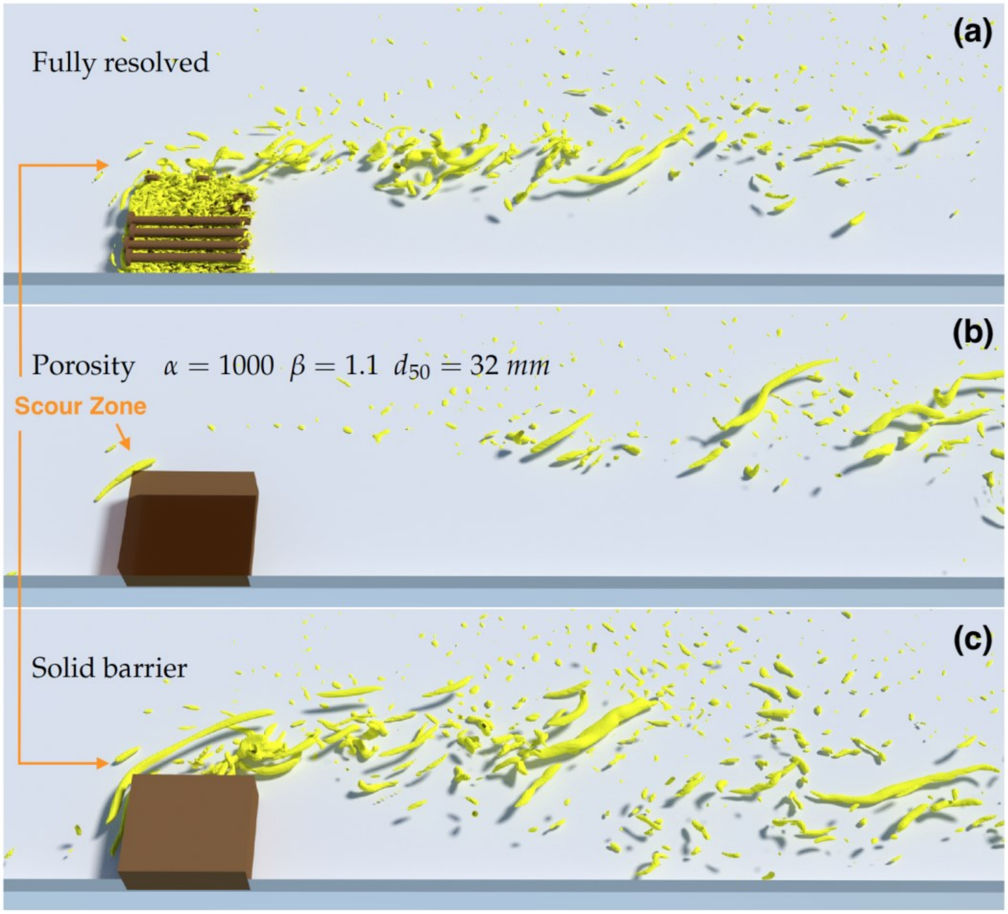

Figure 1.5. Visualization of vortices (in yellow) around deflector structures with different internal structure types. (a) Structure with fully resolved internal ELJ geometry with interlocking logs; (b) structure comprised of a simple porous media; and, (c) solid, impermeable structure. Flow is left to right (modified from Xu and Liu, 2017).

1.3 Interactions of Flow and Sediment

The process of sediment transport by fluid flow may be characterized by the properties of each phase in combination with the interdependent nature of flow and sediment movement. In the vicinity of ELJ structures, the complex patterns of flow turbulence (Section 1.2) play a significant role on local sediment movement and scour evolution. Scour is caused both by localized changes in flow due to the presence of the structure (local scour) and geometric changes that decrease the conveyance area (contraction scour) (Melville and Coleman, 2000). In practice, it is difficult to differentiate between these two processes and the simplified term "localized scour" is used to refer to the simultaneous occurrence of both scour processes (FHWA, 2012; Melville and Coleman, 2000; Wallerstein et al., 2003). Localized scour is expected to concentrate at the toe of deflector ELJs (Papanicolaou et al., 2018) and at the upstream face and upstream flanks of an apex type ELJ (Abbe and Montgomery, 1996).

Both clear water and live bed scour conditions are considered in this study. Clear water scour conditions occur when there is no transport of sediment from the approach flow section into the scour hole. Live bed scour conditions, however, occur when sediment is mobilized in the approach section and is subsequently transported into the scour hole region (FHWA, 2012). The transition between clear water and live bed scour can be estimated to occur when the approach flow shear stress exceeds the critical shear stress for incipient movement of bedload, τ_{cr}. By using similarity principles, previous research has established methods for estimating τ_{cr} and also for estimating mean bedload transport rates at stresses exceeding τ_{cr} (Fernandez-Luque and van Beek, 1976; Elhakeem et al., 2017; Parker et al., 1982; Papanicolaou et al., 2002; Rouse, 1939; Shields, 1936; Suszka, 1991).

An important aspect of flow and sediment interaction during scour development that has not been well studied is the time evolving interdependency of flow and scour features. In particular, the high shear stresses created by flow around ELJ structures (Section 1.2) cause development of a scour hole, which in turn creates a feedback to the flow features as the bed bathymetry evolves (Koken and Constantinescu, 2014; Li, 2016; Papanicolaou et al., 2018). The bed shear stress decay function is one approach that has been recently developed to relate the evolving scour depth with the evolving bed shear stress and can provide a more complete approach to scour prediction (Li, 2016; Suaznabar et al., 2014).

1.4 Critical Literature Review and Research Limitations

Although numerous studies spanning throughout the 20th Century have investigated flow and scour around different hydraulic structures, it is yet uncertain whether existing methods may be applied to predict scour around porous ELJ structures in gravel bed rivers. This uncertainty largely stems from the minimally understood influences on scour from two factors: (1) ELJ structure porosity; and, (2) sediment non-uniformity and particle interlocking in gravel beds. Although it has been highlighted that structure porosity can have significant effects on the scour potential in the flow field around hydraulic structures (e.g., Manners et al., 2007; Xu and Liu, 2017), limited research has been done to investigate scour around porous structures or to develop tools that account for structure porosity (e.g., Kim et al., 2016; Papanicolaou et al., 2018). Also, while the effects of particle interlocking and sediment non-uniformity have received a growing amount of attention and some correction approaches have been proposed (e.g., Ettema, 1983; Euler et al., 2011; Maxwell and Papanicolaou, 2000; Raikar & Dey, 2004), there has been a limited consideration for the whole spectrum of scour (i.e., both clear and live bed conditions) in a gravel bed, with most studies focusing on clear water scour. This study considers the influences of both ELJ porosity and sediment non-uniformity in order to develop enhanced formulas for scour prediction for both clear and live bed conditions.

The thematic focus of recent scour research is also shifting from a limited time-averaged view of scour to a more complete temporal view of scour hole evolution as it connects with flow non-uniformity and unsteadiness (Fox et al., 2005a; Kuhnle et al., 2002; Oliveto and Hager, 2002). This approach could help address two primary causes for inaccuracies of scour depth predictions in gravel bed rivers around permeable ELJs: (1) the focus on the equilibrium state without enough consideration of scour hole evolution, and (2) the mischaracterization of flow fields around ELJs due to oversimplifying assumptions (e.g., considering ELJs as impermeable structures). This new vein of research can also lead to advancement of the FHWA method for scour prediction, which has received attention in recent research. This method is based on the principles of the decay function (Annandale and Smith, 2001) and estimates scour by considering the co-evolution of scour and bed shear stress. The development of this method has been supported by recent experimental and numerical research (Koken and Constantinescu, 2014; Guo, 2011; Lai et al., 2017;Li, 2016), though future work is needed to investigate the decay function characteristics for a wider range of hydraulic structures as well as bed sediment and flow conditions.

While recent studies have improved characterization scour evolution, only a few have been able to do so in a continuous and non-intrusive way (e.g., Friedrich et al., 2005; 2006; Guan et al., 2016). Other studies have used non-continuous testing methods (by stopping and starting the flow), which can introduce experimental errors by affecting the degree of particle interlocking (e.g., Guo, 2011; Kuhnle et al., 2002; Li, 2016). Moreover, many studies considered only the deepest scour location rather than the more complete bathymetry of the scour hole (Fox et al., 2005a; Kuhnle et al., 2003; Wallerstein et al., 2003). As suggested in Papanicolaou et al. (2018), utilizing an array of sonar depth-sensing probes could allow improved scour hole bathymetry mapping throughout an experiment while allowing minimal disturbance of the scour process.

At present, prediction of the flow field characteristics that drive scour development (i.e., shear stress amplification, vortex structures, etc.) in the vicinity of ELJ structures is difficult and further research is needed. Some recent studies have provided improved descriptions of the 3-D flow characteristics around abutments (Barbhuiya and Dey, 2003; Koken and Constantinescu, 2014), porous rock barbs (Fox et al., 2005a; Papanicolaou et al., 2018), and permeable logjams (Bennett et al., 2015; Bocchiola, 2011; Manners et al., 2007; Xu and Liu, 2017), which aid this effort in part. Nevertheless, the tools needed for characterizing the flow field around ELJs are not well developed and are needed in order to guide design and modeling as ELJ implementation increases.

1.5 Critical Needs

Based on the critical literature reviews presented in Section 1.4, in Papanicolaou et al. (2018) and in a publication from the National Academy of Science on scour (Ettema et al., 2011), the following critical needs have been identified:

(1) There is very little research on scour in gravel bed rivers around porous hydraulic structures and the available data has not considered the full spectrum of scour conditions (i.e., clear water and live bed). Available scour formulas are mostly applicable to impermeable structures in sand bed rivers, and, to a lesser extent, for cohesive sediment beds. These formulas may tend to overpredict scour at ELJs in gravel bed rivers because they do not consider the effects of sediment non-uniformity or structure porosity. This research will address this critical need by developing enhanced scour formulas that are applicable to porous ELJs in a gravel bed.

(2) The majority of scour measurements have been done incrementally in time and performed at a fixed location. There are a very limited number of continuous measurements of scour evolution (Friedrich et al., 2005; 2006; Guan et al., 2014). This research will address this limitation by continuously monitoring scour hole evolution with an array of sonar depth-sensing probes. This sonar technology works in laboratory settings, even at a minimal flow depth of 3 cm, and relates sonar beam frequency to distance.

(3) There are limited flow measurements in the vicinity of the toe of a hydraulic structure and most have focused at a single point. There is a need to perform two dimensional flow field measurements using particle image velocimetry (PIV) technology, which can capture the flow

field changes within the scour hole region. Synchronizing these flow field measurements with sonar scour hole measurement can provide unique insights about the co-evolution of scour and flow. In this study, we use state of the art infrared (IR) technology to capture surface flow field changes during scour evolution and analyze the IR images with the large-scale image velocimetry (LSIV) software developed at the Iowa Institute of Hydraulic Research (IIHR). In addition, we use high-resolution Large Eddy Simulation (LES) to investigate the complex turbulent flow field around apex type ELJ structures to discern key locations with high scour potential.

(4) Most current scour formulas predict a maximum depth at what is usually presumed to be the equilibrium condition. However, very few formulas can predict the scour depth at different time increments and relate this information to the decay in shear stress. Li (2014) has shown that as the scour hole evolves, the bed shear stress reduces as form roughness increases. This study, for the first time, provides a decay function describing the bed shear stress evolution during scour around porous structures in a gravel bed.

2. Study Overview

2.1 Scope

The overarching goals of this research are to provide improved tools for predicting equilibrium scour characteristics around porous ELJs in a gravel bed and for predicting the complex characteristics of scour and flow co-evolution. To meet these goals, both physical experimentation and numerical modeling were employed based on input from the WSDOT Technical Advisory Committee. In the experimental campaign, dimensional analysis was employed to develop a physical model of deflector ELJs and to select representative clear water and live bed conditions for testing. The repeatability of equilibrium scour characteristics at these conditions was evaluated rigorously. Results were compared against select scour prediction formulas and were then used in concert with a theoretical delineation of parameters to develop new formulas that consider both the effects of sediment non-uniformity and structure porosity on scour. These new formulas can help minimize the overestimation of maximum scour depth at porous structures in gravel bed rivers. The spatiotemporal co-evolution of scour and flow was also monitored using advanced instrumentation. These unique datasets were used to develop a decay function applicable to describe scour evolution around ELJs in a gravel bed. In the numerical modeling portion of this study, the complex three-dimensional turbulent flow structures were visualized around an apex ELJ structure using Large Eddy Simulations (LES) and can aid estimations of scour, structural stability and energy dissipation.

2.2 Objectives

Overall, the specific objectives of this study are to:

(1) analyze the prototype ELJ reach at the Skagit River and design controlled model experiments;
(2) assess repeatable scour characteristics at a laboratory deflector ELJ for both clear water and live bed scour in a gravel bed;
(3) assess scour hole and flow co-evolution through monitoring of scour depth and flow velocity in the ELJ vicinity;
(4) develop a generic scour equation applicable to porous deflector ELJs in gravel bed rivers;
(5) formulate a decay function approach for predicting scour and flow co-evolution in the vicinity of deflector ELJs within a gravel bed; and
(6) investigate the three-dimensional flow features developing around an apex ELJ structure using numerical modeling.

The results of this study are compared against findings from other studies performed in similar environments, when applicable.

3. Objective 1: Analysis of the Prototype and Design of Controlled Experiments

3.1 Overview of the Skagit River Prototype

3.1.1 Hydrologic, Hydraulic and Bathymetric Information

The prototype river reach considered in this study is located within the Skagit River in Skagit County, WA, where five dolotimber ELJs were installed. Four of the ELJs (ELJs 1-4) were bank-attached deflector ELJs designed to protect State Route 20. ELJs1-3 are located along the bank of the main channel and ELJ4 is located within a secondary channel. The fifth ELJ (ELJ5) is similar to an apex ELJ and is situated on the upstream face of a bar/island with main and secondary channels flowing to either side of the structure. ELJs1-3 and ELJ5 are shown in Figure 3.1. ELJ3 was the primary focus of laboratory experiments because it is in a key location of the prototype river reach and is the largest deflector ELJ. The unique flow features around the bar apex ELJ5 were also investigated in the numerical portion of this study.

A hydraulic analysis memorandum detailing the prototype characteristics was completed by Northwest Hydraulic Consultants, Inc. (NHC) and WSDOT. This report includes river bathymetry, bed elevations, water surface elevations, and hydrological characteristics (NHC, 2010). The stage-discharge data were taken from nearby stream gauges (#12194000, #12193500, #12189500) operated by the United States Geological Survey (USGS). In conjunction with hydrologic analyses for flood damage reduction and other feasibility studies sponsored by the United States Army Corp of Engineers (USACE), the Federal Emergency Management Agency (FEMA), and Skagit County authorities, discharge data and flow frequencies were calculated for the reach bordering State Route 20 near Milepost 100.7 in the ELJ prototype section (Table 3.1). The stream data was published in the state of Washington Water Resources Records by the USGS and in the cited memorandum (NHC, 2010). The hydraulic performance of the ELJs was evaluated at the two design flows, the 2-year and 10-year flow events, corresponding with bankfull and over-bank flow.

Using the provided geographic information system (GIS) bathymetric data, 160 cross sections were taken in ArcGIS along the project reach to ensure high-resolution hydraulic calculations in order to most accurately quantify boundary roughness and flow continuity through the ELJ3 section (Figure 3.1). From this data, it was found that the channel bed slope was approximately 0.0015 ft/ft, the protrusion length of ELJ3 into the main channel was nearly 68 ft, and the channel width near ELJ3 was approximately 500 ft. The total reach length was approximately 1500 ft.

Included in the NHC hydraulics analysis was a stage-discharge relationship established upstream of ELJ5 in a mid-channel location downstream of ELJ3. This relationship was empirically derived by relating features of known elevation to measured discharge values using images and gauge information (WSDOT, 2011). However, due to the change in channel bathymetry between the ELJ3 and ELJ5 sections, this relationship was not explicitly useful in the present experimental design and a more direct stage-discharge relationship at ELJ3 was needed.

Using the GIS data and hydrologic information as inputs, a stage-discharge curve (Figure 3.2) was developed at the ELJ3 location as part of this research by using the HydroCalc software, version 2.0. The HydroCalc program (https://hydrocalc-pro-by-netafim.soft112.com/), which was originally developed by NHC, calculates normal depth and velocity, Froude number, critical depth, and critical velocity from inputs of channel characteristics (shape/cross-section), discharge, Manning's roughness, and the channel slope. The normal depth is calculated from the Manning's equation in English units. The Manning's roughness coefficient, n, was calculated with relation to the median bed particle diameter, d_{50}, by Anderson (1970):

$$n = 0.0395\, d_{50}^{1/6} \tag{3.1}$$

Table 3.1. Hydrologic evaluation of Skagit River flood frequency.

Recurrence Interval (Years)	Annual Exceedance Probability (%)	Peak Flows (cfs)	
		WSDOT (2007)	USACE (2010)
2	50	32230	36000
5	20	45990	46200
10	10	55710	55000
25	4	68680	68100
50	2	78810	79300
100	1	89360	92500

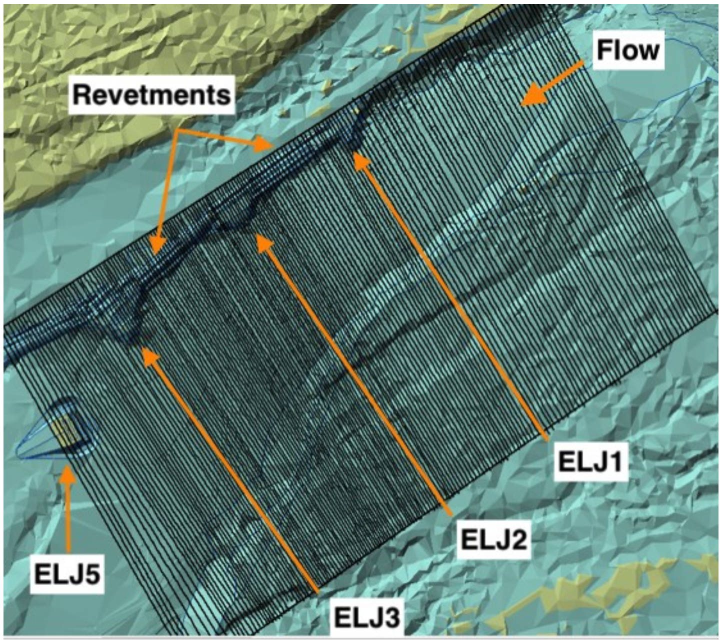

Figure 3.1. Cross-sections taken from bathymetric GIS data for hydraulic calculations.

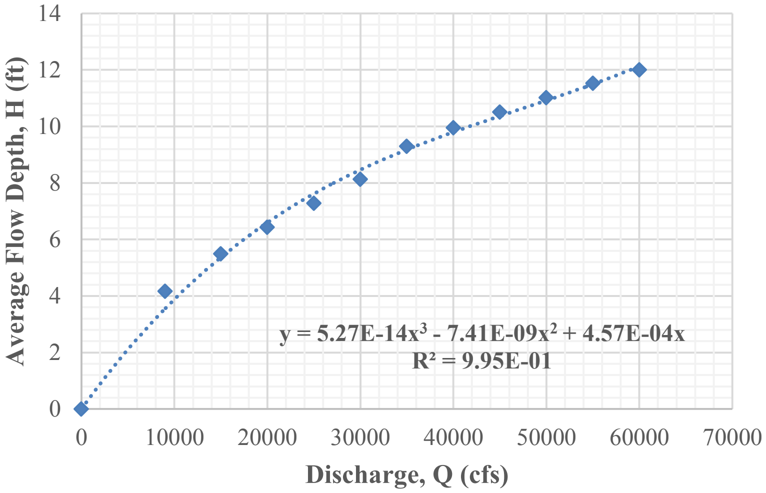

Figure 3.2. Prototype stage-discharge relationship at ELJ3.

The Anderson equation was selected because it was developed using similar bed sediment (0.0005 – 1.0 ft diameter) to the prototype and at slopes less than 1% (Rice et al., 1998). Using d_{50} = 47 mm from the prototype (see section 3.1.2), a Manning's n value of 0.029 was calculated for the prototype channel. This value agrees with the range of 0.023-0.036 for channels containing a gravel bottom and riprap-lined side walls (Chow, 1958). Manning's equation is given by

$$Q = (1.49/n)\, A\, R_h^{2/3}\, S_0^{1/2} \tag{3.2}$$

$$R_h = A/P_w \tag{3.3}$$

$$V = Q/A \tag{3.4}$$

where Q is the fluid discharge, A is the channel cross-sectional area, R_h is the hydraulic radius, P_w is the wetted perimeter, V is the bulk velocity, and S_0 is the energy slope. The Froude number, Fr, which is the ratio of inertial to gravitational forces in open channel flow, is defined as:

$$Fr = V / \sqrt{(gH)} \tag{3.5}$$

where g is the gravitational constant, and H and the approach reach-averaged flow depth. The following additional equations were employed to describe flow characteristics at the prototype:

$$\tau_b = \gamma R_h S_0 \tag{3.6}$$

$$u_* = \sqrt{(g R_h S_0)} \tag{3.7}$$

$$Re_* = u_* d_{50}/\nu \tag{3.8}$$

$$Re = VH/\nu \tag{3.9}$$

$$\tau_* = u_*^2/((S.G.-1)*g*d_{50}) \tag{3.10}$$

where u_* is the friction velocity, Re is the Reynolds number, ν is the kinematic viscosity of water, τ_b is the bed shear stress, τ_* is the dimensionless bed shear stress, γ is the fluid unit weight, and $S.G.$ is the specific gravity of the sediment material (Sturm, 2010).

The relative submergence of a hydraulic structure is defined as the ratio of the flow depth at the structure toe, H_t, to the height of the structure toe, d_t, was considered because of its important implications to scour (e.g. Papanicolaou et al., 2018). To determine the relative submerge of ELJ3, the hydraulic analysis performed by NHC at the 10-year event was used to estimate the water surface elevation at the toe of ELJ3, H_t. Although similar analysis was not available for the 2-year event, the ratio of the near-structure flow depth to the reach-averaged flow depth, H_t/H, was assumed constant to estimate H_t for this event. The average height of the ELJ3 toe, d_t, was estimated from construction documents and near-structure bathymetric data to be about 11.8 ft (+/- 1.5 ft).

Table 3.2 summarizes the key flow condition parameters for the two design flow events at the prototype and provides the key basis for design of model experiments.

Analysis of Table 3.2 shows that flow was subcritical ($Fr < 1$) and turbulent ($Re > 4000$) at both the 2-year and 10-year events. These conditions are present in many natural rivers (McQuivey, 1973). The reach-averaged dimensionless bed shear stress for the 2-year event was equal to 0.047, while it was equal to 0.065 for the 10-year event. This parameter is important for understanding the characteristics of sediment mobility and the threshold of motion for non-uniform sediments typically occurs at $\tau_{cr}^* = 0.03\text{-}0.06$ (Brownlie, 1981; Buffington, 1995; Parker et al., 2003; Shields, 1936). Thus, this analysis suggests that clear water scour is expected at ELJ3 during the 2-year event and that live bed scour is expected during the 10-year event. In addition, it is important to note that a change from partial submergence ($H_t/d_t < 1$) to full submergence ($H_t/d_t > 1$) conditions is estimated to occur between the 2-year and 10-year events, which may have important implications to scour.

Table 3.2. Prototype flow conditions for 2-year and 10-year events.

			Event	
Parameter	**Symbol**	**Units**	**2yr**	**10yr**
Discharge	Q	ft^3/s	33000	55000
Water temperature	T	°F	55	55
Kinematic viscosity	v	ft^2/s	1.21E-05	1.21E-05
Fluid unit weight	γ	lb/ft^3	62.41	62.41
Reach length	L	ft	1500	1500
Channel bed slope	S_0	[]	0.0015	0.0015
Median sediment diameter	d_{50}	ft	0.1542	0.1542
Approach flow depth	H	ft	8	11
Flow depth at the toe of ELJ3	H_t	ft	~9.5	13
ELJ3 relative submergence	H_t/d_t	[]	0.81	1.10
Depth-average bulk velocity	V	ft/s	8	9.5
Reynolds number	Re	[]	5.29E+06	8.64E+06
Froude number	Fr	[]	0.498	0.505
Wetted perimeter	P_w	ft	533.5	543.6
Cross sectional area	A	ft^2	4201.2	5750.5
Hydraulic radius	R_h	ft	7.9	10.6
Friction velocity	$u*$	ft/s	0.622	0.729
Particle Reynolds number	Re_*	[]	7.92E+03	9.29E+03
Bed shear stress	τ_b	lb/ft^2	0.75	1.03
Dimensionless bed shear stress	$\tau*$	[]	0.047	0.065

3.1.2 Mobile Bed Sediment

Two Wolman (1954) pebble counts were performed at the prototype reach to characterize the grain size distributions for both the surface and subsurface material (WSDOT, 2010). Papanicolaou participated in the second pebble survey. The subsurface material was sampled at ELJ5 and was used to determine bed material characteristics prior to bed armoring. The surface material was sampled near ELJ3 and was used in this study since they pertained directly to the location and scour conditions to be modeled (Figure 3.3). The key particle sizes of d_{16}, d_{50}, and d_{84} were determined to be 33, 47 and 71 mm, respectively. These represent the 16th, 50th, and 84th percent finer grain diameters. The two most important values to consider are the median bed material size, d_{50}, and the geometric standard deviation of the distribution, σ_g, which is defined as

$$\sigma_g = \sqrt{(d_{84}/d_{16})} \qquad (3.11)$$

and expresses the degree of sorting in non-uniform size distribution materials. σ_g was equal to 1.47 and thus the gravel represented a poorly-sorted bed composition. The particle specific gravity was reported to be 2.65.

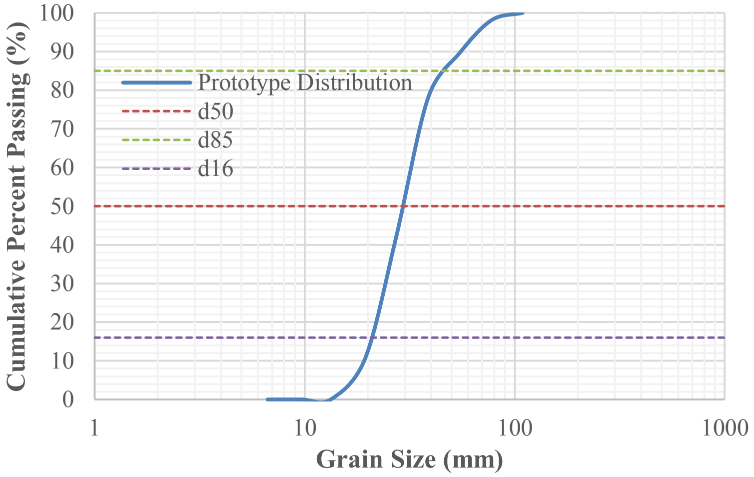

Figure 3.3. Prototype grain size distribution (WSDOT, 2010).

3.1.3 ELJ Placement and Architecture

Figure 3.4 shows the location and construction plans for all five ELJ structures. Downstream of ELJ3, which was the largest of the ELJs placed along the bankline (i.e., ELJs1-4), the flow of the Skagit River divided between the main channel and a side channel. ELJs 1-2 were upstream of ELJ3, and ELJ4 was placed within the side channel. ELJ5 was situated on a bar/island downstream of ELJ3 and helped direct flow primarily into the main channel and away from the side channel. Revetments were stationed downstream of protruding ELJs to stabilize the bank and prevent intermediary erosion.

The ELJs were designed with launchable toes that could deform but maintain their structural integrity as scour developed. Both the ELJs and the revetments incorporated LWM, which constituted high percentages of the structures. According to Mosher and Lunnum (2003), either Douglas fir or Sitka Spruce were most likely used in the project based on local availability and the desired acoustic properties. In the prototype, 15 different dolotimber configurations were created for different purposes by varying the size, number, location and orientation of logs. Each ELJ and revetment was built in layers by stacking the irregularly shaped dolotimber modules in an interlocking manner. The prototype ELJs were designed by Cardno Entrix in accordance with WSDOT standards (WSDOT, 2010a; 2010b; 2010c; 2003).

Using the construction documentation from WSDOT (2011), the ELJ and revetment configurations were dissected to perform a volumetric analysis of their components, which are summarized in Appendix A. Table 3.3 illustrates the component breakdown and approximate porosity of ELJ3.

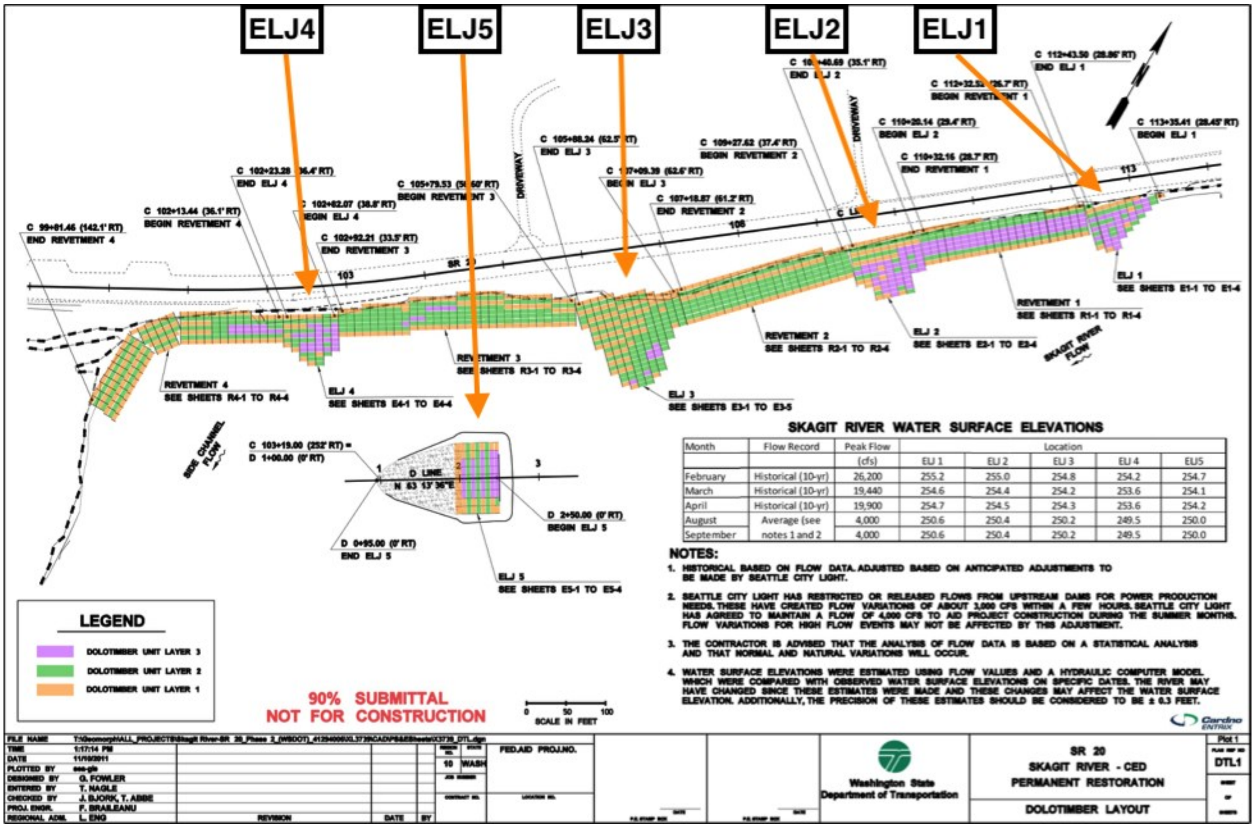

SKAGIT RIVER WATER SURFACE ELEVATIONS

Month	Flow Record	Peak Flow	Location				
		(cfs)	ELJ 1	ELJ 2	ELJ 3	ELJ 4	ELJ5
February	Historical (10-yr)	26,200	255.2	255.0	254.8	254.2	254.7
March	Historical (10-yr)	19,440	254.6	254.4	254.2	253.6	254.1
April	Historical (10-yr)	19,900	254.7	254.5	254.3	253.6	254.2
August	Average (see notes 1 and 2	4,000	250.6	250.4	250.2	249.5	250.0
September		4,000	250.6	250.4	250.2	249.5	250.0

NOTES:

1. HISTORICAL BASED ON FLOW DATA. ADJUSTED BASED ON ANTICIPATED ADJUSTMENTS TO BE MADE BY SEATTLE CITY LIGHT.
2. SEATTLE CITY LIGHT HAS RESTRICTED OR RELEASED FLOWS FROM UPSTREAM DAMS FOR POWER PRODUCTION NEEDS. THESE HAVE CREATED FLOW VARIATIONS OF ABOUT 3,000 CFS WITHIN A FEW HOURS. SEATTLE CITY LIGHT HAS AGREED TO MAINTAIN A FLOW OF 4,000 CFS TO AID PROJECT CONSTRUCTION DURING THE SUMMER MONTHS. FLOW VARIATIONS FOR HIGH FLOW EVENTS MAY NOT BE AFFECTED BY THIS ADJUSTMENT.
3. THE CONTRACTOR IS ADVISED THAT THE ANALYSIS OF FLOW DATA IS BASED ON A STATISTICAL ANALYSIS AND THAT NORMAL AND NATURAL VARIATIONS WILL OCCUR.
4. WATER SURFACE ELEVATIONS WERE ESTIMATED USING FLOW VALUES AND A HYDRAULIC COMPUTER MODEL WHICH WERE COMPARED WITH OBSERVED WATER SURFACE ELEVATIONS ON SPECIFIC DATES. THE RIVER MAY HAVE CHANGED SINCE THESE ESTIMATES WERE MADE AND THESE CHANGES MAY AFFECT THE WATER SURFACE ELEVATION. ADDITIONALLY, THE PRECISION OF THESE ESTIMATES SHOULD BE CONSIDERED TO BE ± 0.3 FEET.

Figure 3.4. Construction plans for prototype ELJs and revetments (Cardno Entrix, 2011).

Table 3.3. Prototype ELJ3 component breakdown and approximate porosity.

ELJ 3 Prototype			
Component	**Volume (ft^3)**	**Percent Structure Volume (%)**	
Cobble	440	1.4	
Logs	12024	39.3	
Dolos	18118	59.2	
Total Solids	30582	**Porosity**	72.0
Total Volume	109312		

3.2 Dimensional Analysis and Parameter Limits

Dimensional analysis was used to identify the important parameters to be considered in the design of the laboratory model and in the selection of appropriate flow conditions for testing. Acceptable limits for each parameter were defined using the literature in order to ensure that the study results would be applicable to the Skagit River prototype and also more generally to other gravel bed rivers within the Pacific Northwest. The enforcement of these limits in this study allowed development of experiments with comparable conditions to the Skagit River prototype, though experiments exhibiting exact similarity conditions were not conducted due to limitations in the flume width.

For characterization of an open channel flow with a fixed rough bed, the key parameters that arise from dimensional analysis of the fluid, flow and channel variables are the following: the Reynolds number, Re, which is a ratio of inertial to viscous forces; the Froude number (Fr), which is a ratio of inertial to gravitational forces; the relative roughness, which is the ratio of the flow depth to the median sediment size, H/d_{50}; and, the channel aspect ratio, which is the ratio of the approach channel width to the average flow depth, B/H. The Reynolds numbers for model flow conditions were ensured to be within the fully turbulent regime ($Re > 4000$), which also occurs at the prototype (Peakall et al., 1996). The Froude number was limited to the subcritical regime ($Fr < 1$), which is representative of conditions found in most natural rivers (Franzini et al., 1997). It is noted, however, that the live bed scour conditions were selected at the upper end of the subcritical flow regime (i.e., with $Fr \approx 0.9$) in order to ensure conservative scour estimates. Such high flow conditions, which mainly occur during infrequent high flow events, cause flow constriction and the development a water surface depression (Dey and Raikar, 2005; Sturm, 2010; Wu and Molinas, 2005) as well as elevated shear stresses at the structure toe (Molinas et al., 1998), which can affect scour depth. These tests are thus considered as upper limit conditions applicable to the design of hydraulic structures in gravel bed rivers. To ensure that no surface effects from the bed sediment were pronounced during the tests, the relative roughness limit of $H/d_{50} > 3$ was imposed (Bettess, 1984). Also, to ensure that the incoming flow was two-dimensional, the aspect ratio was always greater than 5 (Song et al., 1994). Because of the important effects of ELJ relative submergence (H_t/d_t) on scour depth and scour hole geometry (Papanicolaou et al., 2018), this additional parameter was also considered and H_t/d_t was matched between the prototype and model experiments.

When considering the mobile nature of the bed material, another set of parameters arise for establishing comparability of sediment movement between prototype and model experiments. By accounting for the flow and sediment properties, the following additional parameters are considered: the grain Reynolds number (Re_*); and, the dimensionless shear stress (τ^*). The grain Reynolds number is a measure of the roughness of the bed relative to the thickness of the viscous sub-layer, which was maintained within the range of $Re_* > 70$ to ensure hydraulically-rough flow (Chang, 1988). The dimensionless shear stress is a key parameter affecting the probability of sediment motion (Papanicolaou et al., 2002; Elhakeem et al., 2016) and sediment transport rates (Fernandez-Luque and Van Beek, 1976; Parker et al., 1982). Thus, model conditions were selected to have a similar τ^* value to the prototype conditions. Because of the influence of the sediment grain size geometric standard deviation, σ_g, on particle interlocking characteristics (Raudkivi and Ettema, 1997), model sediment was selected with nearly identical σ_g to the prototype. Finally, a direct match of the model and prototype ELJ3 porosities was used because of the importance that structure porosity can have on flow and scour (Manners et al., 2007; Papanicolaou et al., 2004).

3.3 Design of Laboratory Experiments

3.3.1 *Flume Infrastructure*

Laboratory experiments were conducted in the Hydraulics and Sedimentation Laboratory at the University of Tennessee, Knoxville (http://hsl.engr.utk.edu/). The tilt-able, water-recirculating flume, designed by Engineering Laboratory Design, Inc., is 10.0 m long, 0.60 m wide, and 0.50 m deep. The flume slope can be adjusted electronically up to a maximum of 5%, allowing for model design to replicate high gradient streams. A digital slope reader estimates the slope to accuracy of 0.01%. Water is conveyed from the storage reservoir to the flume headbox by a Leeson centrifugal pump with a 1600 gpm discharge capacity. Flowrates are measured via a digital magnetic flow meter and reported with an accuracy of ±0.01 gpm. The connection between the headbox and the flume channel included a series of honeycomb, rectangular grates and a bed section of large gravel (d_{50} = 25 mm) over the initial 0.5 m length (Figure 3.5). These methods collectively decreased energy and turbulence induced by the inflow pipe and headbox. Furthermore, the honeycomb helps induce rectilinear flow at the flume inlet, reducing the role of surface waves and encouraging the expedited formation of fully developed flow conditions.

At the flume exit, 5 mm diameter steel rods were installed perpendicular to the flow in order to adjust the tailwater conditions and obtain uniform flow (Figure 3.6). At the outlet section of the flume channel, a plexiglass step was raised approximately 0.15 m from the flume floor and was used to contain the downstream end of the sediment bed (Figure 3.7). Any sediment transported out of the test section was allowed to transport across smooth plywood until it reached the exit of the flume (Figure 3.7). Exiting sediment was trapped in a porous basket system that was constructed underneath the flume water outfall (Figure 3.8). This basket could be removed periodically to record sediment transport rates. Also, the support structure for the sediment basket had a safety net to capture any sediment that was missed by the basket.

The flume walls are made of transparent plexiglass, allowing side-view optical access to assess flow quality and observe scour over the entire flume length. A moveable trolley was mounted to rails running along the top of the flume and housed the different instruments (ADV, point gage, infrared camera, sonar probes) utilized throughout the study (Figure 3.9).

Figure 3.5. Flume inlet with rectangular grates and cobble bed entrance to promote uniform flow.

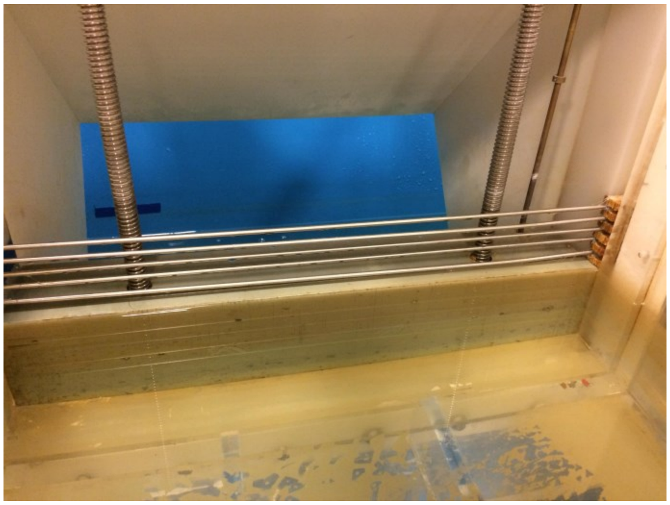

Figure 3.6. Series of steel rods mounted at the flume tailgate for fine control of resistance.

Figure 3.7. Outlet step at the end of the flume test section.

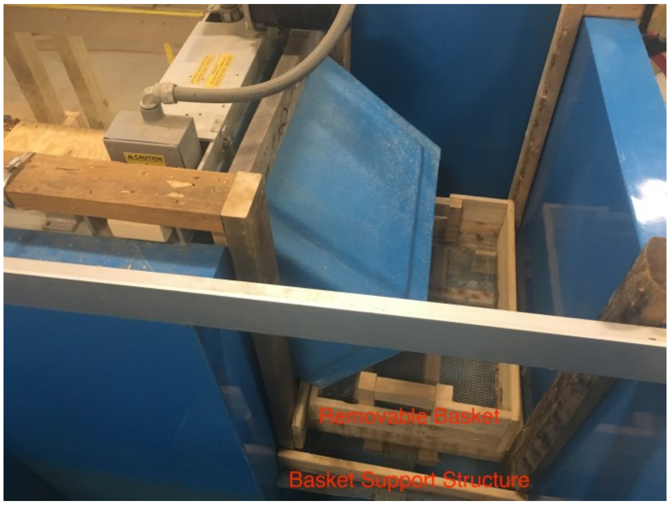

Figure 3.8. Sediment basket used to capture outgoing sediment from the flume outfall.

Figure 3.9. Movable trolley mounted to the flume rails and used for holding instrumentation.

3.3.2 Mobile Bed Sediment

The floor of the flume was covered with a loose layer of aggregate freely laid to maintain a uniform bed height and roughness while minimizing compaction. The naturally worn gravel, provided by Harrison Aggregates in Knoxville, TN, had a d_{50} of 8.12 mm and a σ_g equal to 1.46. The 0.15 m thick layer of gravel was estimated to be of an adequate depth for achieving maximum scour by considering a factor of safety applied to the maximum scour estimates from a number of equations (e.g., Ghodsian and Tehrani, 2001; Melville, 1993). The model and prototype grain size distributions are compared in Figure 3.10.

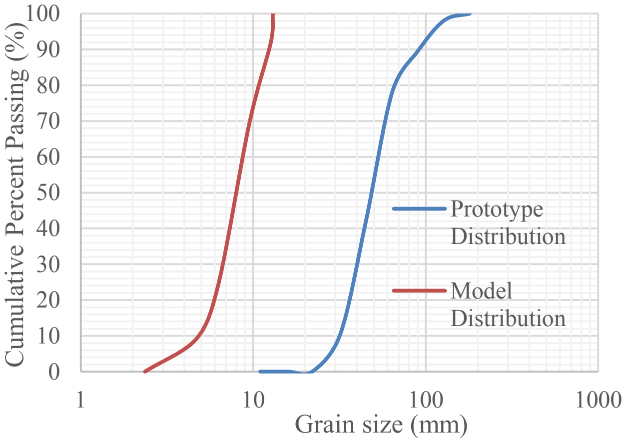

Figure 3.10. Grain size distribution comparison between model and prototype.

3.3.3 Design and Construction of the Model ELJs and the Test Section

The first three ELJs (ELJ1-ELJ3) in the prototype section were selected for the model experiments. Since ELJ4 was placed in the prototype secondary channel, its effects were expected to have negligible effect on the scour evolution around ELJ3, which was in the main channel. ELJ5 was not modeled in physical experiments due to width limitations of the flume.

The first three revetments were included in the model, whereas the fourth revetment in the side channel was ignored.

In order to create a sturdy base for support of the gravel revetment and ELJ structures, a wooden frame made of plywood was built along the flume wall (Figure 3.11). Four coats of waterproofing wood sealant were applied to the plywood to prevent warping.

Figure 3.11. Platform constructed in ELJ test section and installed in the flume.

Model dolos were fabricated from concrete using custom made female silicone molds. The molds were created by first making proxy dolos. Proxy dolos were made from aluminum sheeting that was rolled into cylinders of 3.8 cm diameter (Figure 3.12a). Proxy dolos were then coated with motor lubricant, placed into a tray, and covered with silicone caulking to create female molds. After curing the silicone molds for approximately 8 hours, they were removed from the tray and split at a 45° angle (Figure 3.12b). The completed molds were then used to cast model dolos from a fine, sieved concrete mixture. Great care was taken during the removal process because the sieved concrete mix was quite brittle. Once removed, the model dolos were filed down to match the shape and surface roughness of the prototype dolos (Figures 3.12c).

Wooden dowels were cut and fastened to the dolos to mimic the prototype LWM. Pine dowels were selected in order to replicate the acoustic properties exhibited in the prototype log components (Littell et al., 2010). The model dolotimber structures were sized iteratively based on the relative dimensions of protrusion length and structure height, porous capacity in structure volume, and the weight of each modular dolotimber. The dolotimbers were heavy enough so that they did not float, but light enough such that they did not crack after repeated use and thereby alter model porosity. Of the 15 dolotimber configurations used in the prototype, only three were used in the model (Figure 3.12d) since they constituted over 90% of the total dolotimbers used in the prototype (Cardno Entrix, 2011).

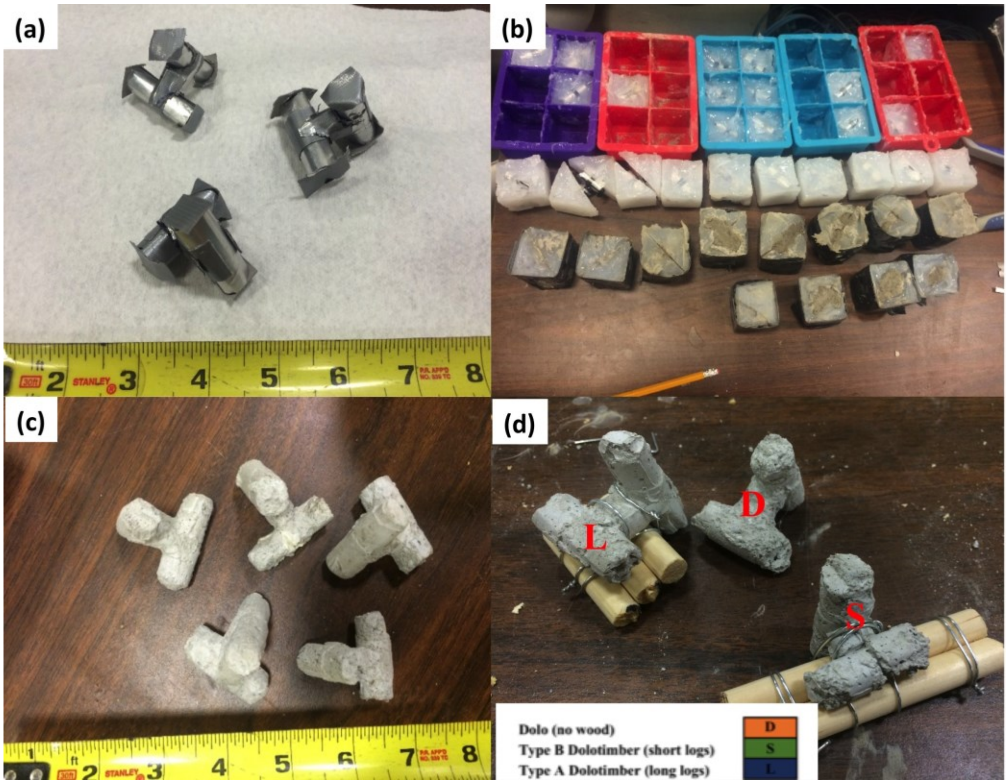

Figure 3.12. Images showing the construction of model dolotimber components from (a) creation of male mold design, (b) female mold development, (c) final concrete model dolos and (d) final model dolotimber configurations used in stacked matrix.

The two key criteria used for design and assembly of the model ELJ were the structure porosity and the relative proportions of dolotimber components (dolo and logs). In order to calibrate scour prediction for gravel bed rivers around porous structures, growing emphasis was placed on closely matching structure surface area, volumetric proportions, porosity and their effects on drag force (Manners et al., 2007). The model ELJs closely matched prototype proportions and were predominantly comprised of dolos (~60%), with the rest being made up of logs (~39%) and a small percentage of cobble ballasts (~1%). Figure 3.13 illustrates the stacked dolotimber matrix used to achieve similar structure porosity. Figure 3.14 shows a closer view of the model ELJ3.

ELJ 3 Prototype			
Component	**Volume (ft^3)**	**Percent Structure Volume (%)**	
Cobble	440	1.4	
Logs	12024	39.3	
Dolos	18118	59.2	
Total Solids	30582	**Porosity**	72.0
Total Volume	109312		
ELJ 3 Model			
Component	**Volume (in^3)**	**Percent Structure Volume (%)**	
Logs	16.4	40.3	
Dolos	24.4	59.7	
Total Solids	40.8	**Porosity**	72.0
Total Volume	145.7		

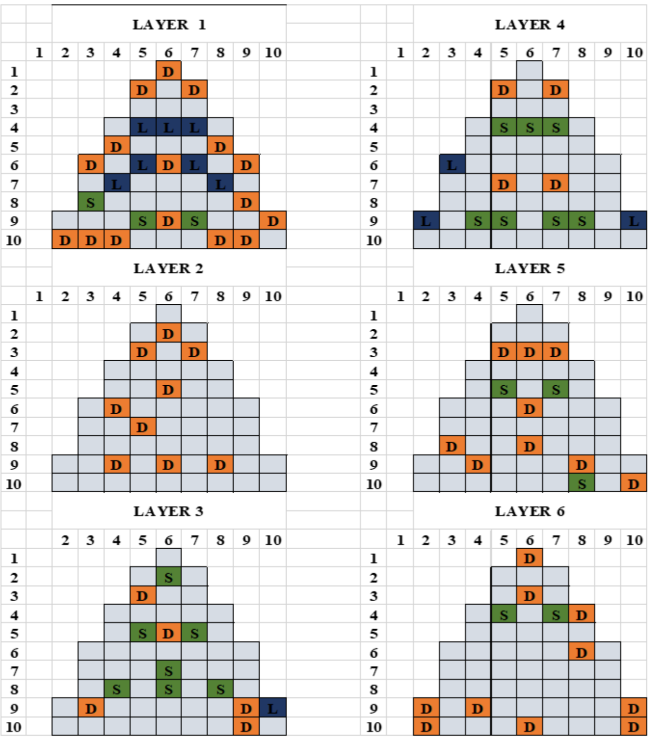

LAYER 1

	1	2	3	4	5	6	7	8	9	10
1						D				
2					D		D			
3										
4					L	L	L			
5				D				D		
6			D		L	D	L		D	
7				L				L		
8			S						D	
9					S	D	S			D
10		D	D	D				D	D	

LAYER 2

	1	2	3	4	5	6	7	8	9	10
1										
2						D				
3					D		D			
4										
5						D				
6				D						
7					D					
8										
9				D		D		D		
10										

LAYER 3

		2	3	4	5	6	7	8	9	10
1										
2						S				
3					D					
4										
5					S	D	S			
6										
7						S				
8				S		S		S		
9			D						D	L
10									D	

LAYER 4

	1	2	3	4	5	6	7	8	9	10
1										
2					D		D			
3										
4					S	S	S			
5										
6			L							
7					D		D			
8										
9		L		S	S		S	S		L
10										

LAYER 5

	1	2	3	4	5	6	7	8	9	10
1										
2										
3					D	D	D			
4										
5					S		S			
6						D				
7										
8			D			D				
9				D				D		
10								S		D

LAYER 6

	1	2	3	4	5	6	7	8	9	10
1						D				
2										
3						D				
4					S		S	D		
5										
6								D		
7										
8										
9		D		D						D
10		D				D				D

Figure 3.13. Relative component percentages and porosity for dolotimber matrix, and matrix layout for ELJ3

Figure 3.14. Oblique view of constructed ELJ3 model

To mimic prototype bankline roughness characteristics, a revetment was installed along the bank adjacent to the ELJs. Due to factors limiting the use of dolotimbers (time and labor required for construction; dolo fragility), however, alternative materials were explored. The primary design parameter was the revetment permeability. A coarse gravel was therefore used as a proxy for the dolotimber revetment. Appropriate gravel to match the permeability of the prototype revetment structures (Section 3.1.3; Appendix A) was selected using the Kozeny-Carman equation:

$$k = [\eta^3/(1-\eta)^2]*[d_{eff}^2/(C_{SH}^2 C_{PK})] \tag{3.12}$$

$$C_{PK} = 5\ \tau^n \tag{3.13}$$

$$K = k\mu/\rho g \tag{3.14}$$

where k is the permeability (m/s), η is the porosity, d_{eff} is the effective diameter (m), τ is the tortuosity, n is the tortuosity coefficient, C_{SH} is the shape coefficient, C_{PK} is the packing coefficient, K is the hydraulic conductivity (m/s), μ is the dynamic viscosity of water (kg/(m s)), and ρ is the density of water (kg/m^3). Assuming C_{PK} is equal to 9.5 and n is equal to 3 based on the input from literature, a gravel with effective diameter of 0.025 m was determined to be appropriate (Judge, 2013; Svensson, 2014). More detailed calculations are provided in Appendix B. The gravel revetment was secured with a wire mesh with nominal openings of 1.25 cm, which was able to maintain porosity and limit the alteration of surface roughness (Figure 3.15).

Figure 3.16 shows an overhead perspective view of the ELJ section and Figure 3.17 shows the dimensioned plans of the designed model.

Figure 3.15. Gravel revetment with wire mesh support.

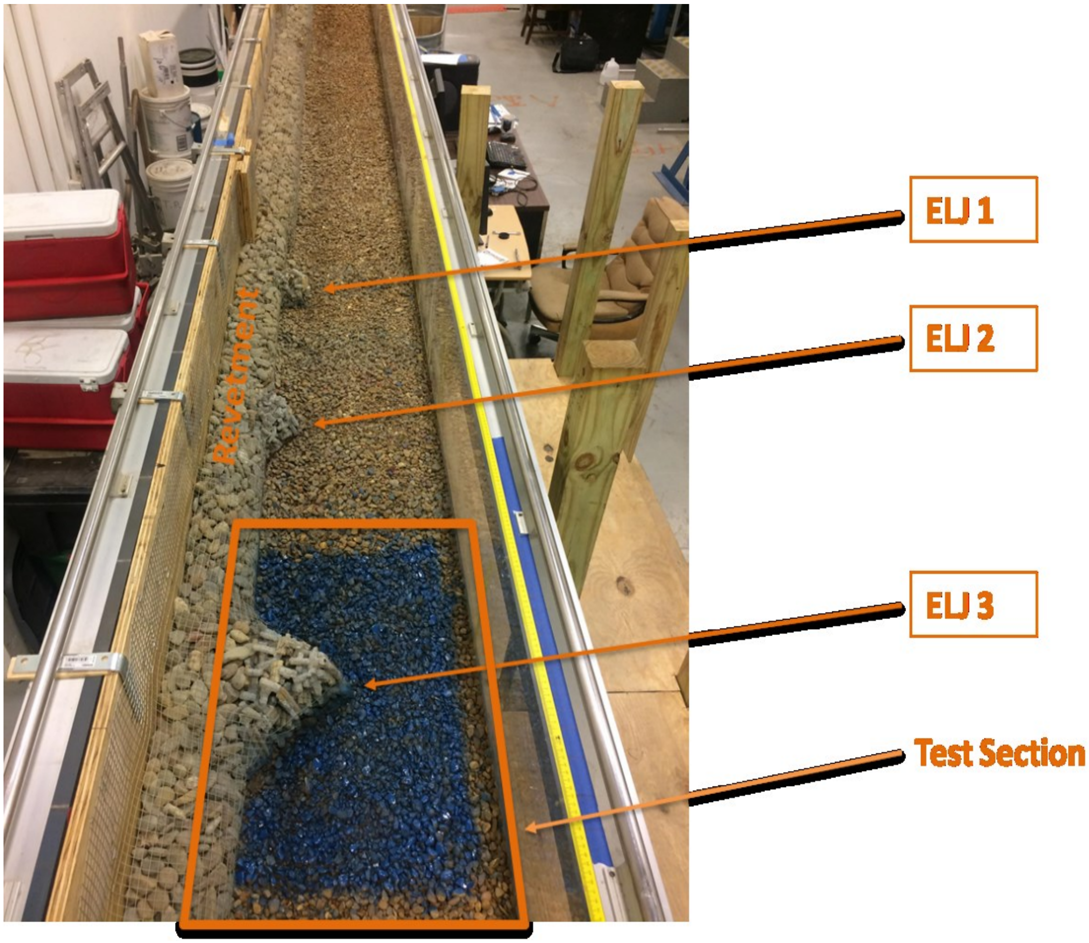

Figure 3.16. Plan-view of constructed model test section.

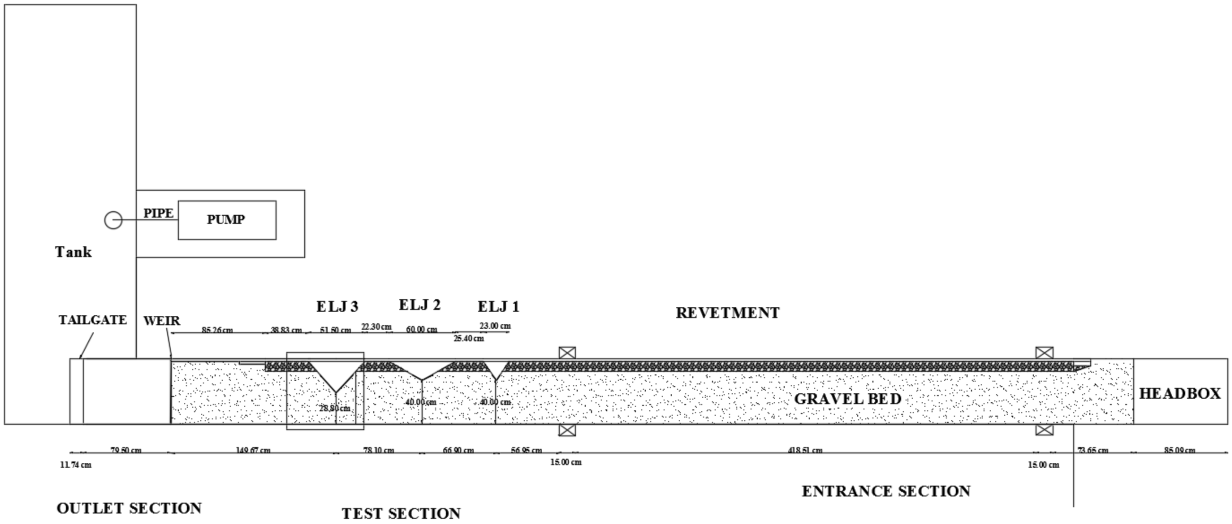

Figure 3.17. Dimensioned plan view of flume model setup.

3.3.4 Selected Experimental Conditions

Based on the dimensional analysis and defined parameter limits (Section 3.2), the flow conditions were determined iteratively to find an optimal point where satisfaction of the multiple regime limits was ensured. The targets of flow condition design were to develop (1) a clear water scour condition that was comparable with the prototype 2-year discharge and (2) a live bed scour condition that was comparable with the prototype 10-year discharge. It is noted that the live bed scour experiments were performed with higher Fr (= 0.90) than exhibited at the prototype (= 0.51) in order to provide conservative scour depth estimates applicable to ELJs in gravel bed rivers within the Pacific Northwest. Conservative scour depths are expected from these tests since they cause flow constriction and the development a water surface depression (Dey and Raikar, 2005; Sturm, 2010; Wu and Molinas, 2005) as well as elevated shear stresses at the structure toe (Molinas et al., 1998). These live bed scour tests are thus considered as upper limit conditions applicable to the design of hydraulic structures in gravel bed rivers. The key parameters for the prototype and the selected model flow conditions are compared in Table 3.5.

Table 3.5. Comparison of prototype and model flow conditions

Parameter	**Symbol**	**Units**	**Model Parameter Limits**	**Prototype Event**		**Model Condition**	
				2yr	**10yr**	**Clear water**	**Live Bed**
Discharge	Q	ft^3/s	*NA*	33000	55000	0.724	2.479
Bulk velocity	U_{bulk}	ft/s	*NA*	8.0	9.5	1.9	3.2
Approach flow depth	H_a	ft	*NA*	8	11	0.269	0.384
Reynolds number ($\times 10^3$)	Re	-	$Re > 4 \times 10^3$	5290	8640	49	121
Froude number	Fr	-	$Fr < 1.0$	0.50	0.51	0.66	0.90
Relative roughness	H/d_{50}	-	$H/d_{50} > 3.0$	51.9	71.3	10.1	14.4
Bed slope	S_0	%	*NA*	0.15%		0.57%	0.85%
Grain Reynolds number	Re_*	-	$Re_* > 70$	7920	9290	461	687
Dimensionless shear stress	τ^*	-	Similar range	0.047	0.065	0.035	0.074
Median bed material size	d_{50}	mm	Gravel range (3-64mm)	47		8.1	
Bed material geometric standard deviation	σ_g	-	Similar magnitude	1.47		1.46	
ELJ3 porosity	ϕ_{ELJ}	%	Equivalent	72%		72%	
ELJ3 relative submergence	H_t/d_t	-	Regime match ("< 1" or "> 1")	0.81	1.10	0.88	1.20

3.3.5 Flow Quality Assessments

A uniform water surface profile was ensured by reading water depths at ten locations along the flume length with graded tape rulers. As expected, backwater effects caused by the ELJs resulted in a local depth increase, and, thus, flow uniformity was defined using the flow depths in the flume inlet and outlet.

The test section location, i.e., the location where the ELJs were placed, was selected to ensure that the flow was fully-developed during all tests. The length downstream from the headbox at which fully developed conditions were achieved, L_d, was calculated using $\frac{L_d}{4R_h} = 32$, where R_h is the hydraulic radius (Nezu and Nakagawa, 1986). The test section was thus placed 7.25 m downstream of the headbox.

To evaluate the flow structures developing in the vicinity of the model ELJ3, qualitative dye tests were performed to visualize the flow characteristics. Figure 3.18 presents an image following dye injection at a location just upstream of ELJ3 and allows visualization of a few flow features. First, when the dye met the upstream face some traveled in the downflow that occurred at the upstream face of the ELJ. Second, another portion of the dye traveled via the primary vortex around the structure nose. Finally, the wake vortices were visualized through the portions of dye that traveled toward the bank into the region of slower flow. Figure 3.19 presents an image following dye injection further upstream and away from the nose of ELJ3, which visualized clearly the shear layer where the dye in the secondary vortex and main core flow was repelled by the primary vortex. The wake area is most clearly visualized in Figure 3.20, which presents an image that was taken a few moments after dye was introduced in a single large pulse near the revetment. This dye plunged with the down flow then traveled around and through the permeable structure to reach the other side. This resulted in recirculation of dye in the ELJ wake region, which is outlined with a dotted line.

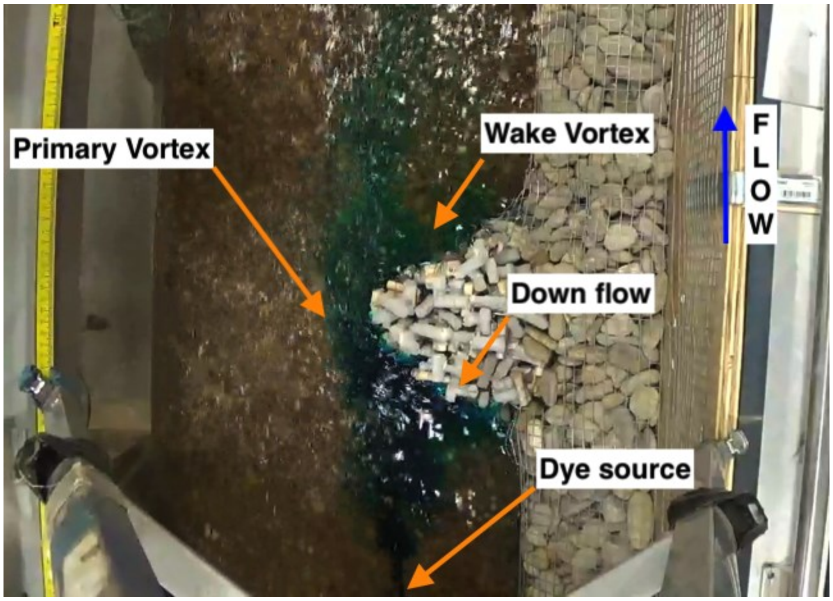

Figure 3.18. Model ELJ3 dye test illustrating location of down flow, primary vortex, and wake vortices.

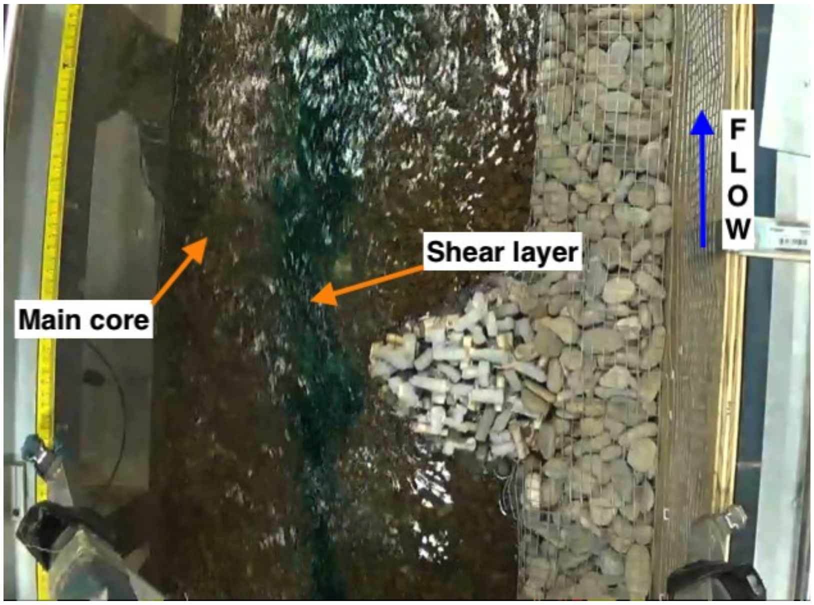

Figure 3.19. Model ELJ3 dye test illustrating shear layer formation and main core flow.

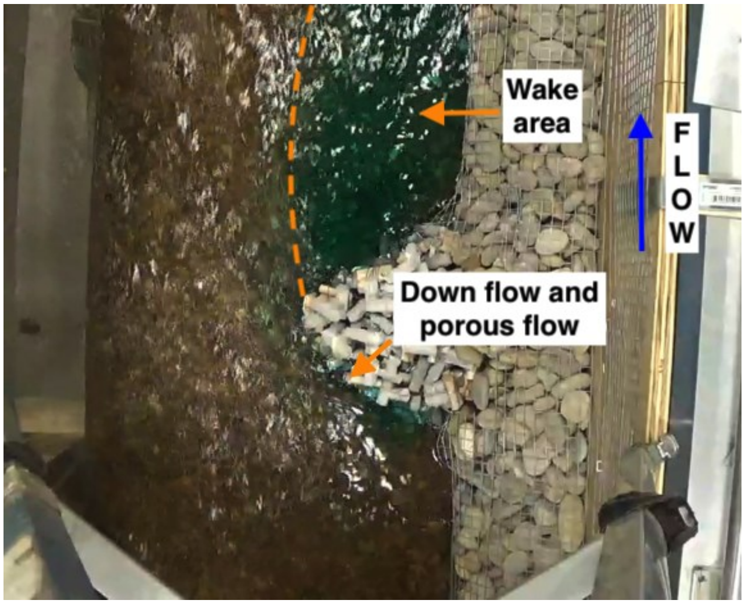

Figure 3.20. Model ELJ3 dye test showing down and porous flows that travel to wake area.

3.4 Conclusions for Objective 1

1. A thorough analysis of the prototype allowed determination of the key parameters needed to characterize the flow and the ELJ structures.
2. Dimensional analysis was used to identify the important parameters to be considered in the design of laboratory experiments. Parameter limits were used to develop model clear water and live bed scour conditions that were comparable to the prototype.
3. Dye visualizations of the flow field around the model ELJ3 show that the model experiments replicate the expected flow structures in the ELJ vicinity.

4. Objective 2: Assessment of Repeatable Equilibrium Scour Characteristics

4.1 Experimental Methodology

4.1.1 Determination of the Critical Clear Water Scour Condition

To set the general context for scour experiments, it was important to first determine the critical clear water scour condition. This condition was estimated by observing particle movement at the toe of ELJ3 while incrementally increasing the flow conditions until scour occurred. Each flow stage was held constant and movement was observed for 5-10 minutes before proceeding to the next increment if scour did not occur. The critical condition was defined as that which caused an initial group of particles to be mobilized near the toe of the ELJ and thus led to the development of a scour hole. The approach flow dimensionless bed shear stress, τ^*, at the critical condition for clear water scour was equal to 0.034, which compares well with previous results found in a gravel bed in the vicinity of a porous barb structure (Papanicolaou et al., 2004).

4.1.2 Scour Experiment Procedure

More than 70 scour experiments were conducted as part of this research at both clear water and live bed scour conditions in order establish the optimal experimental procedures and define the degree of scour repeatability. Sensitivity of scour initiation (location and scour rate) and equilibrium scour characteristics (magnitude and location of maximum scour depth, scour hole shape, and scour volume) were evaluated in development and assessment of the experimental procedure. The experimental procedure is described as follows:

1. Flume operation conditions
    a. Tank reservoir depth was constant to ensure flow discharge consistency.
    b. Flume slope was set mechanically and verified digitally.
    c. Excess air was released from the pump prior to testing to ensure steady discharge.
    d. Flow uniformity was assessed by measuring flow depths across the flume length. Tailwater depth was controlled using rods at the tailgate, which were adjusted to ensure uniformity.
2. Bed material
    a. The bed level was set at a defined constant level before every test.
    b. Gravel materials in the vicinity of the ELJ structures were removed and replaced after each test to ensure no size change occurred between tests.
    c. Bed material was mixed throughout the bed depth to ensure that no surface armoring occurred.
    d. Bed material was raked and set with great care near the ELJ structures to eliminate bias in scour initiation.
3. Test initiation procedure
    a. A perforated metal gate was placed at the tailgate to provide increased flow resistance and ensure that scour did not initiate when the flow discharge was started.
    b. The pump discharge was slowly increased (1) to prevent energetic bursts that might prematurely initiate scour and (2) to ensure slow filling of air voids in the bed material.
    c. Once at the target discharge, the perforated gate was systematically removed by small increments every 10 seconds to allow the water surface profile to equalize gradually. The gate removal phase was about 2-3 minutes in duration. Scour initiation

    corresponded with the point of full removal of the gate with about +/- 1 minute of lag time. This rigorous procedure yielded consistent scour initiation and evolution results.
    d. When scour initiated, a water surface profile was taken along the entire flume length.
4. Bedload rate monitoring (live bed scour only)
    a. Sediment particles leaving the test section were allowed to fall out into the flume tank with outgoing water and were captured in the porous basket.
    b. The basket was removed at pre-defined intervals (3-5 minutes) and the sediment material was emptied into a bucket marked to indicate the given time during the test.
    c. The basket was replaced after being removed and emptied. The time between basket removal and replacement was typically about 10-15 seconds. During the time that the basket was absent, sediment fell into the safety net.
    d. After completion of the experiment, the sediment in each bucket was dewatered and weighed to calculate the bedload transport rates. Also, the sediment caught in the safety net was collected and distributed evenly between each basket measurement.
5. Ending of the test
    a. The total experiment duration was defined for each condition as a multiple of the observed time required to achieve equilibrium scour geometry. These total durations were defined for each flow condition based on preliminary experiments and were equal to 90 minutes for the clear water condition and 60 minutes for the live bed condition.
    b. Once the target test duration was achieved, the perforated gate was re-inserted to halt the scour process by adding significant flow resistance. The gate insertion caused a significant backwater to the water surface profile and effectively halted all scour and bedload movement within about 10-15 seconds.
    c. Pump discharge was decreased and water was drained from the flume back into the reservoir tank.
6. Assessment of equilibrium scour geometry
    a. Bed elevation data was taken using a point gage in the scour hole and the test section. Within the scour hole region, measurements were taken with spacing of 1-3 cm to obtain high quality maps (Figure 4.1). In the regions farther outside the scour hole region, wider spacing was used with a maximum of 10 cm employed for the scour maps taken at live bed conditions.
    b. Maximum scour depth and location were measured via the point gage.
    c. The bed elevation data was plotted using a Matlab code to generate a scour map.
    d. The scour volume was determined from the Matlab code by applying the trapezoidal integration method.

4.2 Results

4.2.1 Equilibrium Scour Hole Geometry

Scour initiation was focused at the toe of the structure where streamlines are most constricted and erosive capacity is greatest (Koken and Constantinescu, 2014). Initiation was marked by an event moving larger clusters of particles that led to scour rates that were initially rapid but decayed gradually until an equilibrium scour depth was achieved (Cardoso and Bettess, 1999). Equilibrium was commonly achieved within the first 25 minutes of the clear water scour tests and within the first 10-15 minutes of the live bed scour tests. The decreased time to equilibrium at live bed scour is related to the higher bed shear stress at this condition, which accelerated the rate of scour.

The maximum scour depth location at equilibrium was typically downstream of the ELJ3 toe, which is similar to scour observations around wing-wall abutments with comparable structure protrusion length (Ettema et al., 2010). The scour hole characteristics for the tests at each flow condition are reported in Tables 4.1 and 4.2. The maximum scour depths were on average near 6 cm for the clear water scour condition and near 8.5 cm for the live bed scour condition. These values were repeatable within 6-11%, which agreed well with the variability reported in other scour studies with a mobile gravel bed (Papanicolaou et al., 2004). The equilibrium scour hole volumes, on average nearly 2850 cm^3 for clear water and 4750 cm^3 for live bed scour, maintained an associated error of 7-14% that compared well with literature (Kuhnle et al., 2002).

The equilibrium scour bed maps for the clear water and live bed tests are presented in Figures 4.2 and 4.3. Comparison of the various trials for each condition show a high degree of repeatability in the scour hole features. In particular, the location of the maximum scour depth at the toe of ELJ3, the conical scour hole shape (Papanicolaou et al., 2018), and the lateral and streamwise extents of the scour hole were similar between the tests.

Table 4.1. Abbreviated test condition and scour results from clear water scour Trials 1-7.

Trial #	Flow discharge, Q (m^3/s)	Approach flow depth, H (m)	Approach flow dimensionless shear stress, τ^* (-)	Maximum scour depth, $d_{s,m}$ (cm)	Scour hole volume (cm^3)
1	0.0205	0.082	0.0350	6.6	2924
2	0.0204	0.081	0.0345	6.2	2656
3	0.0205	0.083	0.0354	6.7	3034
4	0.0204	0.082	0.0350	5.9	2873
5	0.0206	0.082	0.0350	6.5	2831
6	0.0205	0.083	0.0354	6.0	2824
7	0.0205	0.082	0.0350	6.5	2831
Average				6.3	2853
Standard Deviation				0.3	115
Percent Variability (%)				6.3%	6.6%

Table 4.2. Abbreviated test condition and scour results from live bed scour Trials 1-4.

Trial #	Flow discharge, Q (m^3/s)	Approach flow depth, H (m)	Approach flow dimensionless shear stress, τ^* (-)	Maximum scour depth, $d_{s,m}$ (cm)	Scour hole volume (cm^3)
1	0.0702	0.116	0.0738	8.5	4300
2	0.0702	0.119	0.0757	8.2	4788
3	0.0702	0.117	0.0744	9.1	4958
4	0.0702	0.117	0.0744	9.2	4988
Average				8.8	4759
Standard Deviation				0.5	318
Percent Variability (%)				11%	14%

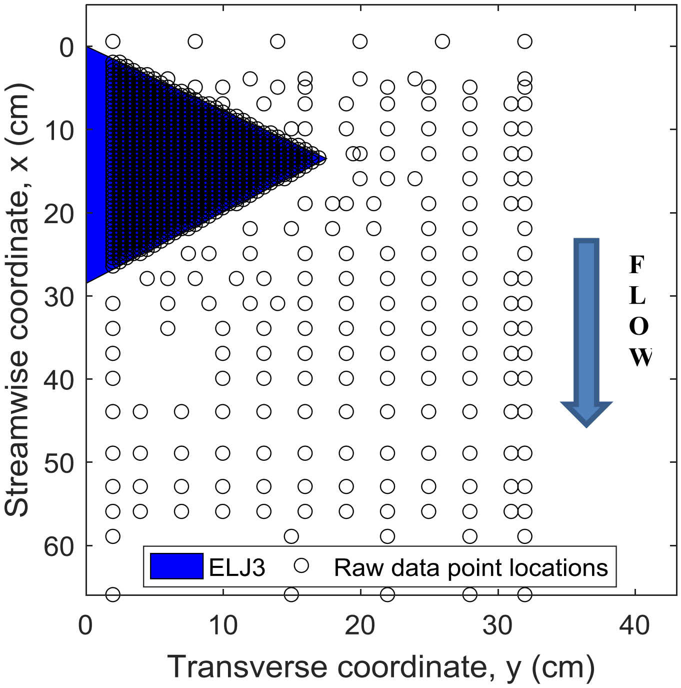

Figure 4.1. Locations of point gage measurements within the scour hole area

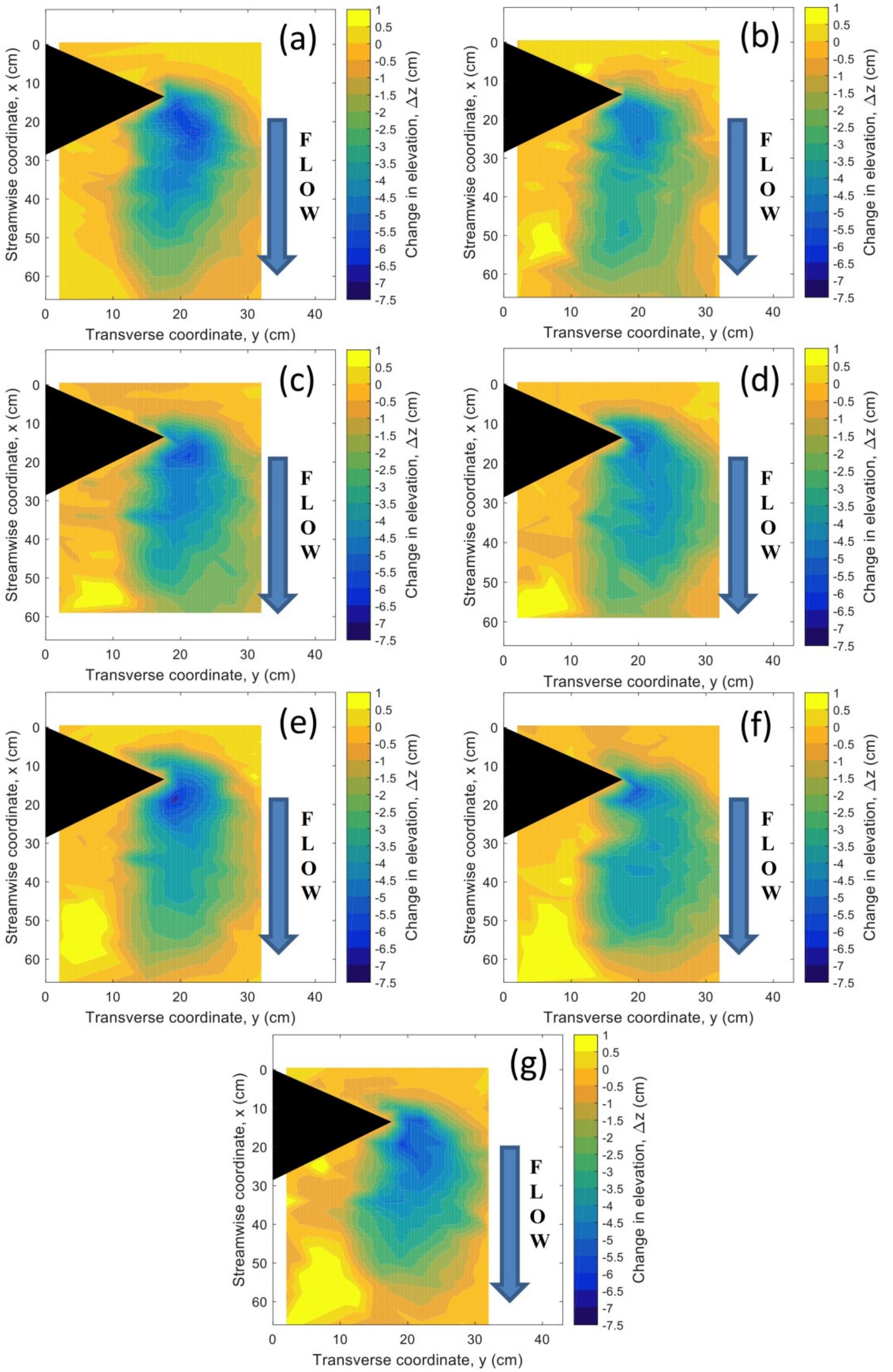

Figure 4.2. Equilibrium scour contour maps for clear water scour (a)-(g) Trials 1-7

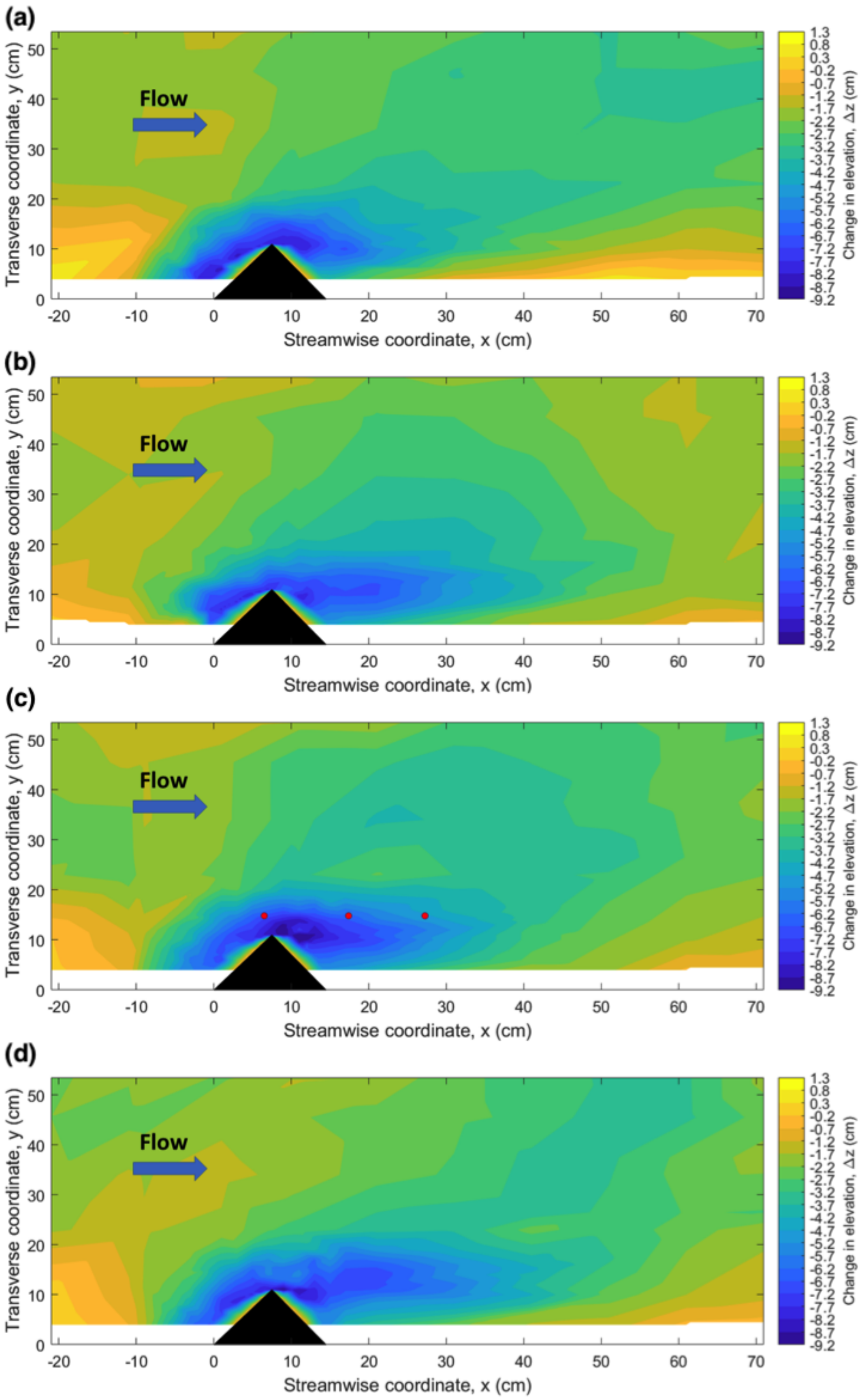

Figure 4.3. Equilibrium scour contour maps for live bed scour (a)-(d) Trials 1-4

4.2.2 Exiting Bedload Rates (Live Bed Scour Only)

The bedload transport rates exiting the flume during the live bed scour experiments were useful for understanding some unique aspects of these scour conditions and for comparison with established bedload transport equations. From the recorded exiting sediment masses, the values of bedload rate per unit channel width, q_s, in units of kg/m/s, were determined. To compare the present results with existing literature, the dimensionless version of q_s, q_s^*, was determined. q_s^* is defined as:

$$q_s^* = \frac{q_s}{\rho_s \left[\left(S.G. - 1 \right) g d_{50}^3 \right]^{0.5}} \tag{4.1}$$

where ρ_s is the sediment density (kg/m^3), $S.G.$ is the sediment specific gravity, g is the acceleration of gravity (m/s^2) and d_{50} is the median bed material size. In Figure 4.4a, q_s^* is plotted as a function of time for live bed scour Trials 1-4. Figure 4.4a shows that bedload rates were high near the start of each test and decreased over time to approach an equilibrium bedload transport rate that remained pseudo-constant for the remainder of the test duration. The high exiting bedload rates near test initiation were attributed to the combined contributions from two sediment sources: (1) the incoming bedload to the test section and (2) the scour hole development. Thus, the occurrence of pseudo-constant exiting bedload rates later in the tests was attributed to the cessation of scour development, which led to the condition that the incoming bedload to the test section was equivalent to the exiting bedload. The observed equilibrium bedload transport rates were generally achieved by about 15 minutes after test commencement and were on average equal to $q_s^* = 4.5\text{x}10^{-3}$, or equivalently $q_s = 0.0335$ kg/m/s.

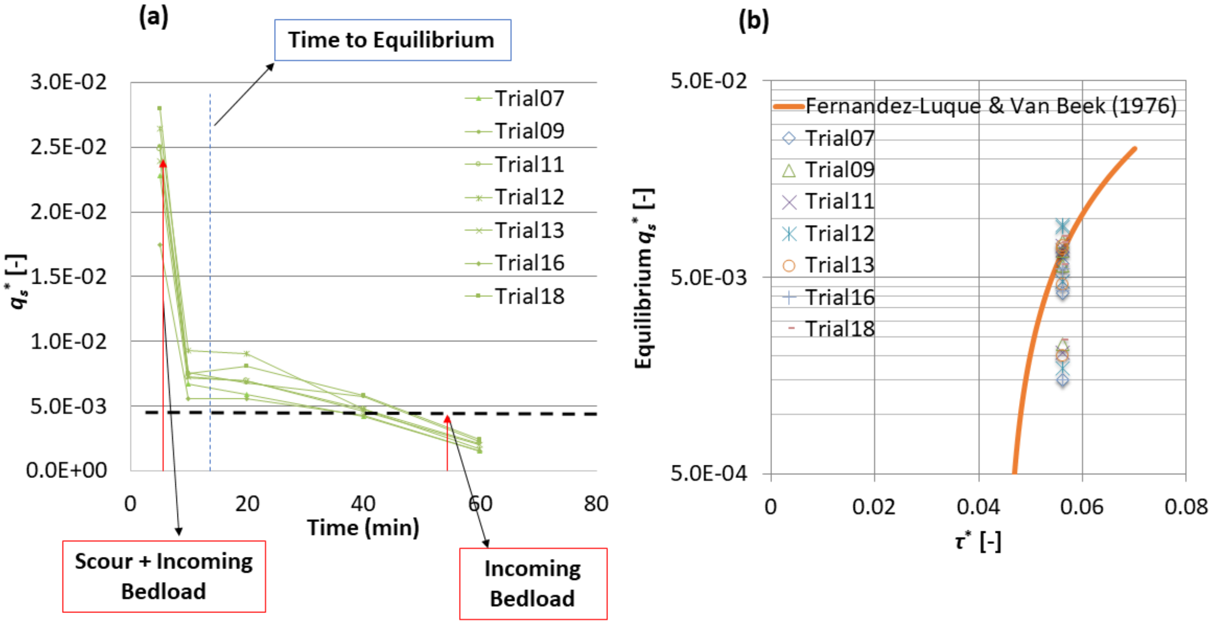

Figure 4.4. Dimensionless exiting bedload rates, q_s^*, during live bed scour tests illustrating (a) temporal evolution and (b) equilibrium bedload rates compared with the Fernandez-Luque and Van Beek (1976) bedload equation.

The equilibrium bedload transport rates are compared in Figure 4.4b with the classic bedload transport equation of Fernandez-Luque and Van Beek (1976):

$$q_s^* = 5.7\left(\boldsymbol{\tau}^* - \boldsymbol{\tau}_{cr}^*\right)^{1.5} \tag{4.2}$$

where τ^*_{cr} is the critical dimensionless bed shear stress corresponding with incipient bedload motion. In the context of scour experiments, τ_{cr}^* corresponds with the condition at which general bedload movement occurs (i.e., live bed conditions) and is different from the critical clear water scour condition determined in Section 4.1.1. A value of $\tau_{cr}^* = 0.045$ was assumed in Figure 4.4b and corresponds closely with the prediction from the Suszka (1991) equation for τ_{cr}^*:

$$\boldsymbol{\tau}_{cr}^* = 0.0851\left(h/d_{50}\right)^{-0.266} \tag{4.3}$$

Comparison of equilibrium bedload transport rates with the Ferndandez-Luque and Van Beek (1976) formula predictions was good and also less than an order of magnitude variability was seen (Figure 4.4b). This order of error is good when compared with typical studies of bedload transport in gravel bed rivers (Papanicolaou et al., 2018).

4.3 Conclusions for Objective 2

1. Qualitative features of the equilibrium scour holes were consistent and exhibited a conical scour hole extending downstream from the ELJ toe and the maximum scour depth occurring just downstream of the ELJ toe.
2. Quantitative metrics for the equilibrium scour geometry (max scour depth, scour hole length and scour hole volume) were measured and showed a good degree of repeatability (6-14%).
3. Exiting bedload transport rates during live bed scour experiments show two sources of sediment: (1) incoming bedload; and, (2) the evolving scour volume. Equilibrium bedload transport rates were achieved when the scour hole reached an equilibrium volume.

5. Objective 3: Assessment of Scour and Flow Co-Evolution

5.1 Experimental Methodology

5.1.1 Monitoring Scour Hole Evolution with Sonar Depth-Sensing Probes

Scour evolution was monitored using the Seatek 5MHz Ultrasonic Ranging System. When submerged, these probes are a capable of reading the bed elevation underneath the probe beam with sub-millimeter accuracy. The system was used to obtain 4 depth readings per second (4 Hz) to track scour depth changes with high frequency. While this method has shown success in tracking the migration of sand bedforms over time in a uniform bed (Friedrich, 2005), to the authors' knowledge there is no comparable research for sonar depth experiments in non-uniform, gravel substrate.

In the early stages of testing, the accuracy of the sonar probes for measuring bed elevations in a gravel bed were verified by comparing the sonar returns with point gage measurements along a scour hole transect under static conditions (i.e., with no scour evolution). The comparison of point gage and sonar probe readings is presented in Figure 5.1. The differences between readings yielded a Root Mean Square Error (RMSE) of approximately 2.4 mm, which was only a fraction of the median bed material size (RMSE/d_{50} = 0.3). These results illustrate the system's ability to take depth measurements over the non-uniform, mobile bed with high accuracy.

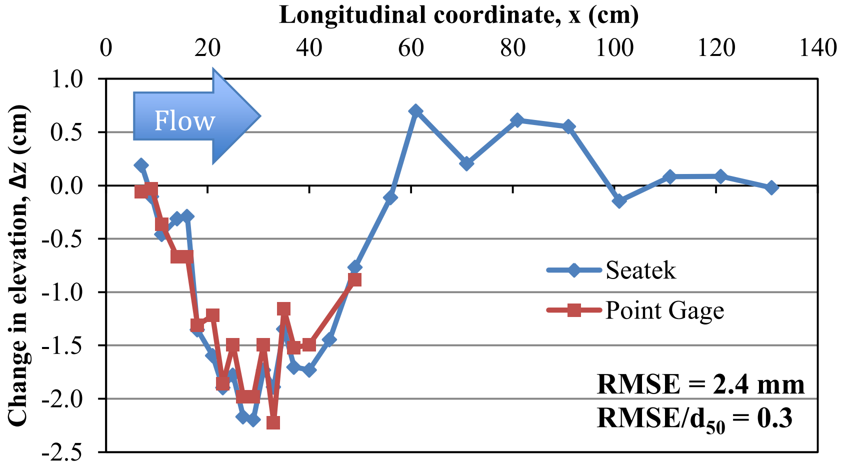

Figure 5.1. Verification comparison of point gage and sonar results for equilibrium scour conditions (i.e., no scour evolution).

For monitoring scour temporal evolution, a linear array of sonar probes was stationed along the thalweg transect of the scour hole. Four probes used for scour monitoring (labeled 1 through 4 in Figure 5.2) were spaced 15 cm apart and were placed at the water surface with minimal intrusion into the water column. The sonar probe locations used at the initiation of each test were determined in preliminary experiments by setting the probes manually to follow the water surface profile, which rapidly varied near the ELJ structure.

Before initiating scour tests with sonar probe monitoring, probe zero-readings were gathered in stillwater conditions. During the trial, the sonar probes were stationed and activated to capture scour evolution over the full experiment duration. In some cases, however, the water surface profile at the probes decreased due to scour evolution and caused some probes to become unsubmerged. When this occurred for a given probe, it was adjusted in elevation to match the new water surface elevation. The change in probe elevation was recorded in order to re-zero data readings.

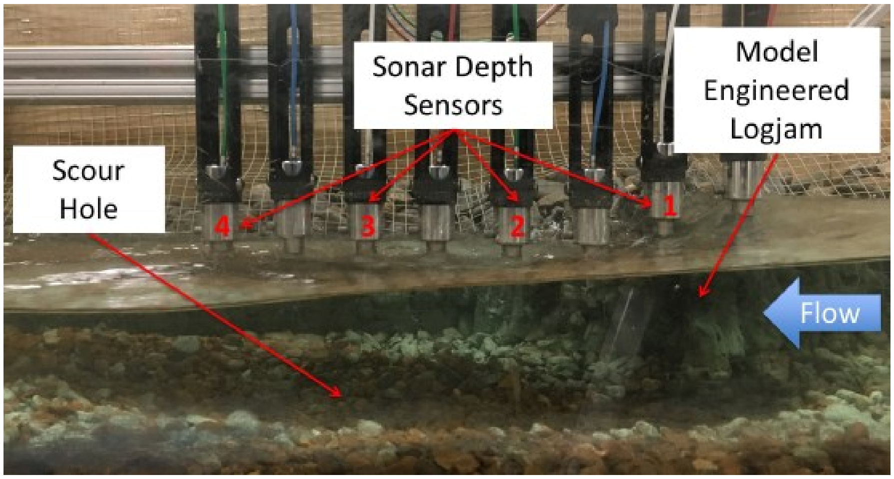

Figure 5.2. Profile view of the HSL sonar set-up, on a trolley, in relation to ELJ and developed scour hole.

To develop accurate scour depth evolution curves from the raw sonar readings, multiple processing and post-processing steps were carried out via a Matlab code that was developed in this research to remove erroneous data points and smooth over measurement noise. An example of the raw, processed and post-processed sonar data results are presented in Figure 5.3. Figure 5.3a shows the raw data and highlights examples of accurate d_s readings and of erroneous data points from multiple error sources. The erroneous data points are attributed to (1) periods when the probes were unsubmerged due to fluctuations in the water surface, (2) moments when moving sediment particles traveled under the probes, and (3) random measurement errors. The processing stage of the Matlab code used median filtering and absolute thresholding algorithms to identify and remove the outliers from the trend established by the accurate data points. The output data from this processing stage was considered to be the accurate scour depth readings that were made within measurement accuracy of the sonar system (Figure 5.3b). The post-processing stage of the Matlab code then applied a linear interpolation between data points and a low-pass smoothing filter to develop a smooth scour evolution curve (Figure 5.3c).

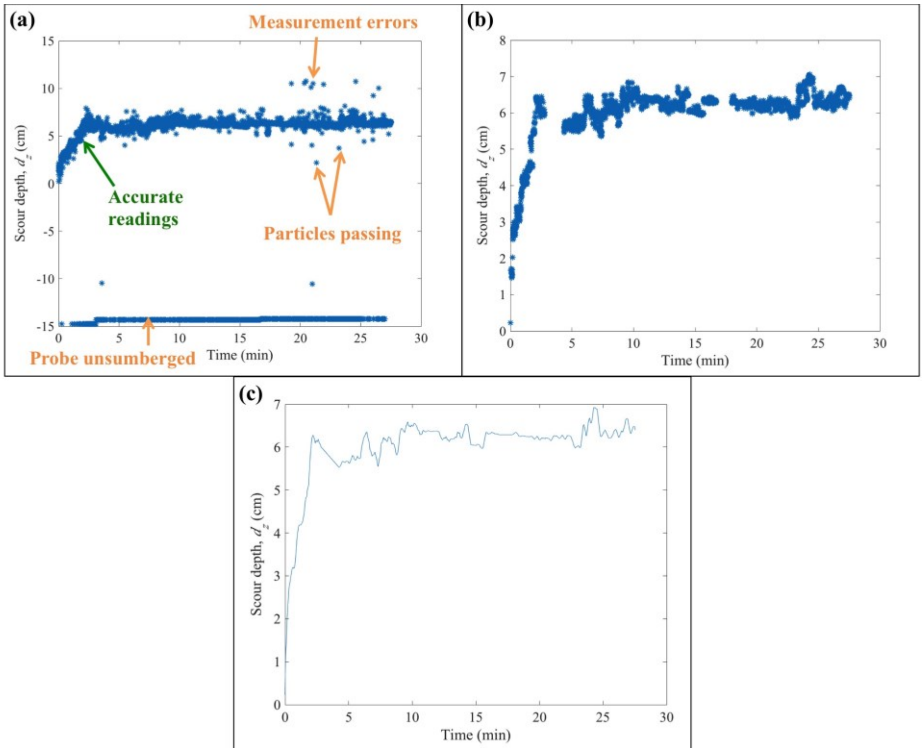

Figure 5.3. Illustration of sonar data with processed and post-processed results. (a) Raw scour depth, d_s, readings with examples of accurate readings and error sources; (b) accurate d_s readings identified via processing steps; (c) post-processed d_s curve.

5.1.2 Monitoring Flow Velocity Evolution with LSIV and ADV

Two separate efforts were made to evaluate the changes in flow field characteristics that were directly related to the effects of scour evolution. First, detailed surface velocity flow field maps around ELJ3 were made for frozen gravel bed configurations with the flat bed and the developed equilibrium clear water scour hole configurations (shown in Figures 5.4 and 5.5). In this testing, the bed was frozen following the methodology outlined in Benson et al. (2001). The comparison of these pre- and post-scour flow field maps illustrates the total changes in flow field characteristics from the start to the end of scour. Second, semi-continuous surface velocity measurements were taken throughout scour evolution in order to assess how the flow field characteristics evolved as a function of time.

To meet both of these goals, both acoustic Doppler velocimetry (ADV) and large scale image velocimetry (LSIV) instrumentation techniques were employed. For the first goal pertaining to frozen bed velocity measurements, the ADV was used to measure velocity near the water surface over a range of locations in the vicinity of ELJ3. To understand the flow structures around the ELJ, sampling points were spread over the approach section, the shear layer, the main core, and the wake. For the second goal of monitoring velocity evolution over time, LSIV was employed for the clear water scour tests, and the ADV was employed for the live bed scour tests (because of the shorter timescale of evolution occurring in live bed scour). The methodological details for obtaining and processing data from each instrument are outlined below.

Figure 5.4. Frozen flat-bed bathymetry in gravel bed for flow field mapping.

Figure 5.5. Frozen scoured bathymetry in gravel bed for flow field mapping.

ADV Instrumentation and Methods

A side-viewing 10 MHz SonTek ADV with sampling rate of 25 Hz and velocity resolution of 0.01 cm/s was employed to obtain 2D velocity measurements in the streamwise and transverse directions (Figure 5.6). An important advantage of the ADV is that it measures the flow in a small sampling volume (approximately 0.25 cm^3) that is 10 cm away from the transmitting transducer (Figure 5.7). Since this model is a side-viewing ADV, it can also be used in shallow flows and near the water surface where down-looking ADVs will be unusable. The ADV provided point measurements of the velocity.

During sampling, the ADV was mounted to a rigid beam in order to limit vibrations. The ADV probe was placed about 2 cm below the water surface for all data taken during this study. In clear water testing at frozen bed conditions, data was taken over roughly 1-minute intervals at each selected location. For the live bed scour trials, the probe was placed outside the scour hole with the sampling volume being located just downstream of the toe of ELJ3, and data was recorded continuously.

The ADV data was post-processed using the *HorizonADV* software provided by SonTek and analyzed in Microsoft Excel. In data processing, data points with a signal-to-noise ratio (SNR) less than 15 or a Correlation (CORR) less than 70% were removed.

Figure 5.6. Side-looking SonTek ADV in flume.

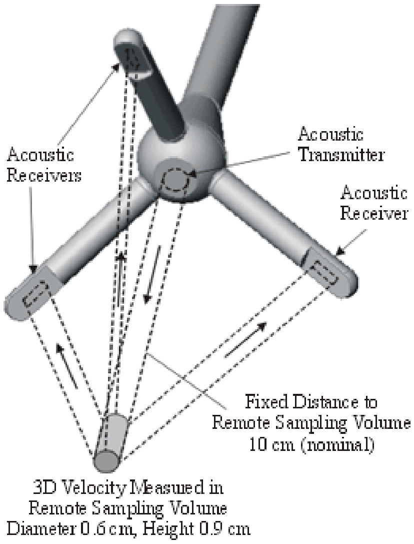

Figure 5.7. Schematic of ADV sampling volume (SonTek, 1998).

LSIV Instrumentation and Methods for the InfraRed (IR) camera data analysis

Particle image velocimetry (PIV) is a powerful and nonintrusive flow measurement technique that is used to track seeding particles over time in order to reveal flow velocities. One approach to PIV flow field monitoring is to employ a thermal imaging camera and use hot water to seed the flow with individual diffusive droplets that can be tracked due to their temperature differential (Fujita et al., 1997; Admiraal, 2009; Papanicolaou et al., 2011). This method is referred to hereafter as LSIV.

To obtain LSIV data, hot water was poured into a reservoir (Figure 5.8) where it was fed at a constant rate though the hose and was distributed evenly across the flume width by using a multi-nozzle sprinkler (Figure 5.9). The droplet movement, beginning approximately 0.50 m upstream of the test section, was recorded with an FLIR Thermacam P65 InfraRed (IR) camera mounted above the observation area (Figure 5.10). The IR camera can capture data at a rate of 30 frames per second for a duration of approximately 35 seconds. The IR camera also had a temperature resolution of 0.08° and captured images with resolution 320x240 pixels. The field of view of the IR camera extended approximately 22 and 30 cm in the transverse and streamwise directions, respectively.

In the LSIV data processing phase, pixels in the IR images were related to the physical model by using calibration images that captured objects separated by a known physical distance. To generate displacement vectors between sequential images, the LSIV software utilized a pixelated interrogation radius and defined search area over which to correlate the successive particle locations. These correlated pixel movements yielded instantaneous displacements, which were then used to calculate instantaneous velocity vectors within the 2D IR camera field of view. Once displacements were obtained, the processing settings were used to remove erroneous velocity readings. The most important processing settings for obtaining accurate readings were the setting of the minimum correlation and the velocity processing range. The final processed instantaneous velocity vectors were then averaged over the sequence duration to yield a 2D time-averaged velocity field (Figure 5.11).

LSIV data was taken periodically during a clear water scour experiment to develop a timeline of the evolving spatial velocity distribution during scour development. Additionally, validation of the thermal LSIV data was done by comparing with the frozen bed ADV velocity measurements made near the water surface at both the flat bed and equilibrium (clear water) scoured bed conditions.

Figure 5.8. Reservoir for hot water supply during IR data collection.

Figure 5.9. Continuous, uniform hot water seeding during IR data collection.

Figure 5.10. IR camera mount for plan-view data collection at ELJ3.

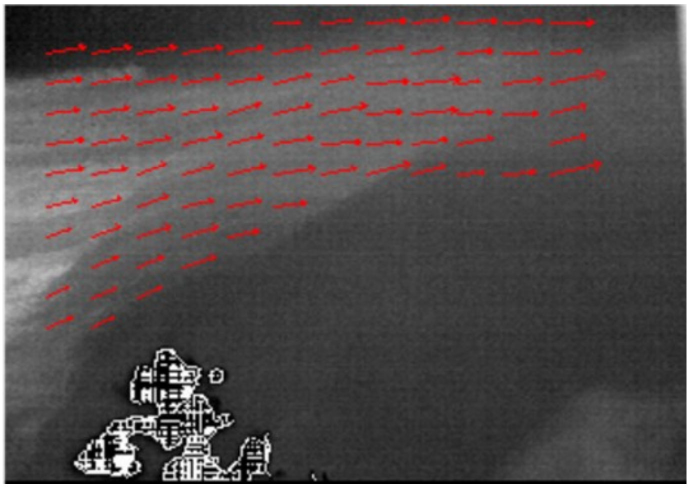

Figure 5.11. Example of surface velocity vectors at one point during scour evolution.

5.2. Results

5.2.1 Scour Hole Evolution

The processed and post-processed sonar scour depth readings from the representative clear water and live bed scour tests are illustrated in Figures 5.12 and 5.13, respectively. In each of these figures, pane (a) presents the sonar outputs as a function of time to illustrate scour evolution and pane (b) compares the end of test sonar readings with the point gauge scour hole transect to validate the accuracy of the readings. Overall, the end of test readings yielded errors with RMSE = 2.1 mm (RMSE/d_{50} = 0.25) for the clear water scour test and RMSE = 9.5 mm (RMSE/d_{50} = 1.17) for the live bed scour test. This order of accuracy was comparable to the stillwater tests, except for the influence of large errors from probe 3 in the live bed scour test, which was attributed to experimental error (i.e. Figure 5.13b)

As discussed in previous literature, the scour depth evolution visualized in Figures 5.12a and 5.13a follow a logarithmic shape with time. Kuhnle et al. (2002) showed similar logarithmic scour depth increase in clear water scour around angled spur dikes in a sand bed and highlighted the fact that scour depth reached nearly 80% of the maximum within the first 20% of the time to equilibrium. The data presented in Figures 5.12a and 5.13a also provide unique insight into the scour volume evolution through continuous capture of scour depths at representative points along the scour hole centerline. This aspect is a unique contribution from this study and has been minimally considered in previous research.

Another important observation from Figure 5.13a for the live bed condition is that there were minimal infilling events near the ELJ toe (i.e., Probe 1) since the scour depth was relatively constant at this location after obtaining a near-maximum value. This behavior was attributed to the high shear stresses at the structure nose (Ahmed and Rajaratnam, 2000; Koken and Constantinescu, 2008; Kothyari and Raju, 2001), which were able to transport incoming material through the scour hole. However, some notable infilling events were observed further downstream of the ELJ, with the maximum depth of infilling recorded at Probe 3 (i.e., at about 5 minutes elapsed) being equal approximately 25% of the maximum scour depth. It is noted that most infilling events at Probes 2 and 3 occurred mostly in the first ~30-40 minutes of the test, after which time the scour depth at these locations was more stable. Overall, these scour monitoring results suggest that the scour volume likely fluctuated for the present live bed tests more than the maximum scour depth due to sediment infilling in the region downstream of the ELJ toe but not near the ELJ toe.

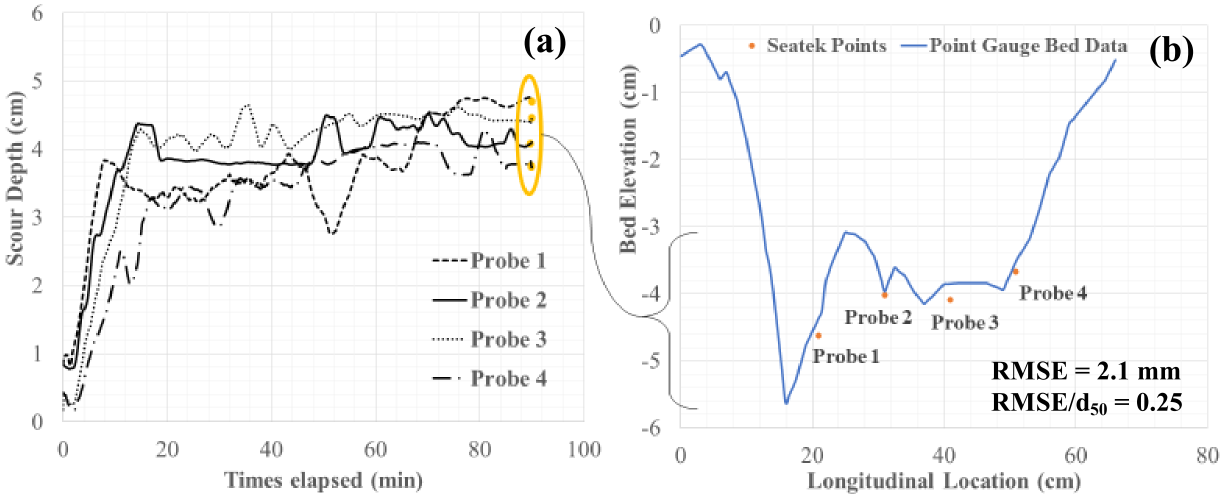

Figure 5.12. For the clear water scour condition, the sonar data is presented to show (a) temporal scour evolution and (b) validation of the end of test sonar readings by direct comparison with point gage readings taken at the end of test.

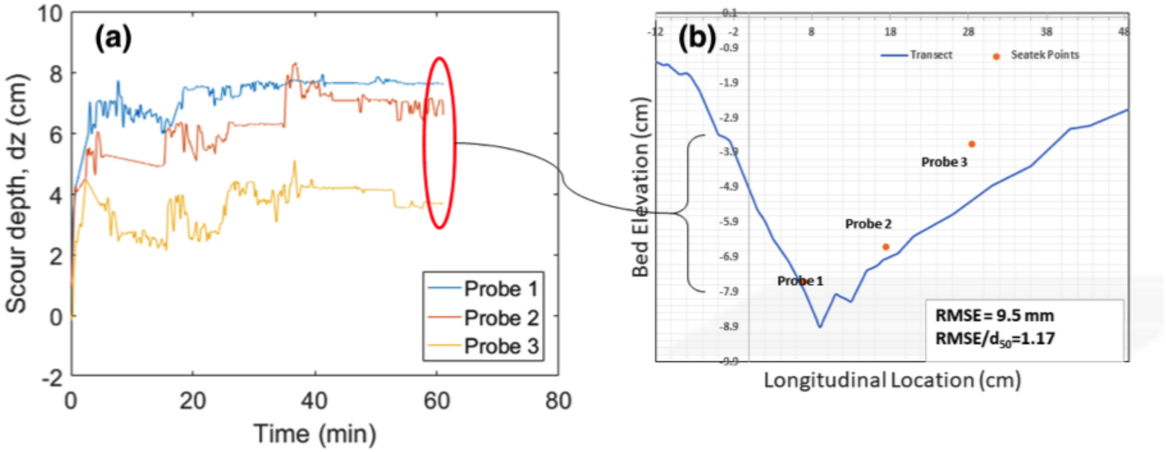

Figure 5.13. For the live bed scour condition, the sonar data is presented to show (a) temporal scour evolution and (b) validation of the end of test sonar readings by direct comparison with point gage readings taken at the end of test.

5.2.2 Flow Velocity during Clear Water Scour Evolution

Flow Field Mapping with Frozen Bed Arrangements

In Figure 5.14 the ADV streamwise velocities in select locations are compared for pre- (Figure 5.14a) and post-scour (Figure 5.14b) conditions. The general trends in velocity from comparison of Figures 5.14a and 5.14b are illustrated in Figure 5.14c. These trends first show that velocities upstream of the ELJ increased during scour evolution, which is attributed to a decrease in backwater effects as the scour hole evolved. Second, the trends in Figure 5.14c show that velocities downstream of the ELJ decreased as scour evolved, which is attributed to energy dissipation within the scour hole. These maps thus highlight the complex nature of scour and flow co-evolution and provide a baseline of expected trends that can be compared with more detailed temporal monitoring of flow evolution during scour progression.

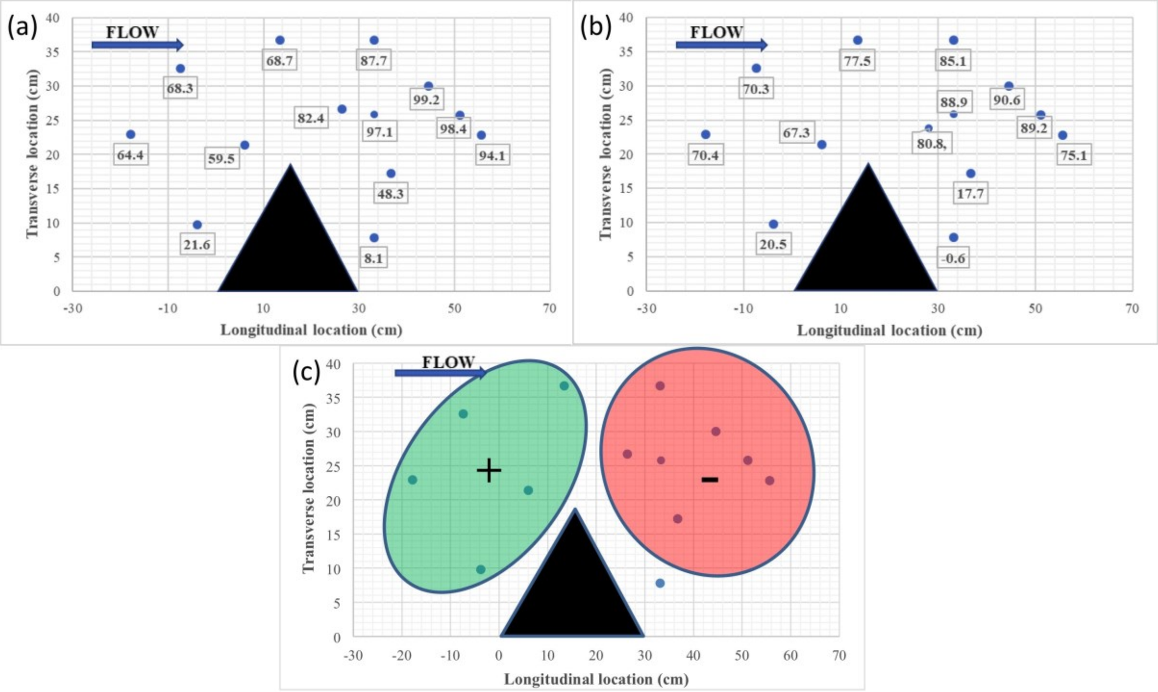

Figure 5.14. Measured ADV streamwise velocities (cm/s) at select locations in test section for the clear water scour conditions and showing (a) pre-scour conditions, (b) post-scour conditions, and (c) a summary of overall velocity trends (+ indicates an increase in velocity and – indicates a decrease in velocity).

<u>LSIV Validation</u>

Direct comparisons between frozen bed LSIV and ADV (i.e. Figure 5.14) data are shown Table 5.1. This comparison shows that, on average, there was less than 10% difference between ADV and LSIV velocity magnitudes. Thus, the LSIV system was deemed to be suitable for capturing mean flow velocities in the ELJ vicinity.

Table 5.1. Comparison of LSIV and ADV velocity magnitudes at multiple locations for the frozen flat bed condition to validate LSIV readings

ADV Velocity (cm/s)	LSIV Velocity Range (cm/s)	Maximum % Difference	Minimum % Difference
90.7	90 - 100	9.7	0.8
87.8	80 - 90	9.3	2.5
97.3	90 - 100	7.8	2.7
82.4	80 - 90	8.8	3.0
68.7	60 - 70	13.5	1.9

Monitoring Flow Temporal Evolution

The results from the clear water scour trial with simultaneous LSIV velocity monitoring are summarized in Figure 5.15. The LSIV velocity maps (bottom panes in Figure 5.15) show the shear layer extending downstream of the ELJ toe, which occurs at the interface between the high and the low velocity regions. The shear layer location near the ELJ toe as visualized by LSIV corresponds closely with the location visualized with the dye experiments (i.e., Figure 3.19). Perspective photos of scour progress were also taken simultaneously with individual LSIV datasets and are presented in the top panes of Figure 5.15 for comparison. As scour developed, the velocity contour plots illustrate the overall trend of the faster moving velocities (displayed as green and red contours) decreasing (to blue contours) and shifting as the scour hole developed. At the toe of the ELJ in particular, the velocity decreased notably. This shows that the flow energy available to mobilize sediment decreased as scour evolved, which eventually led to the attainment of the equilibrium scour condition.

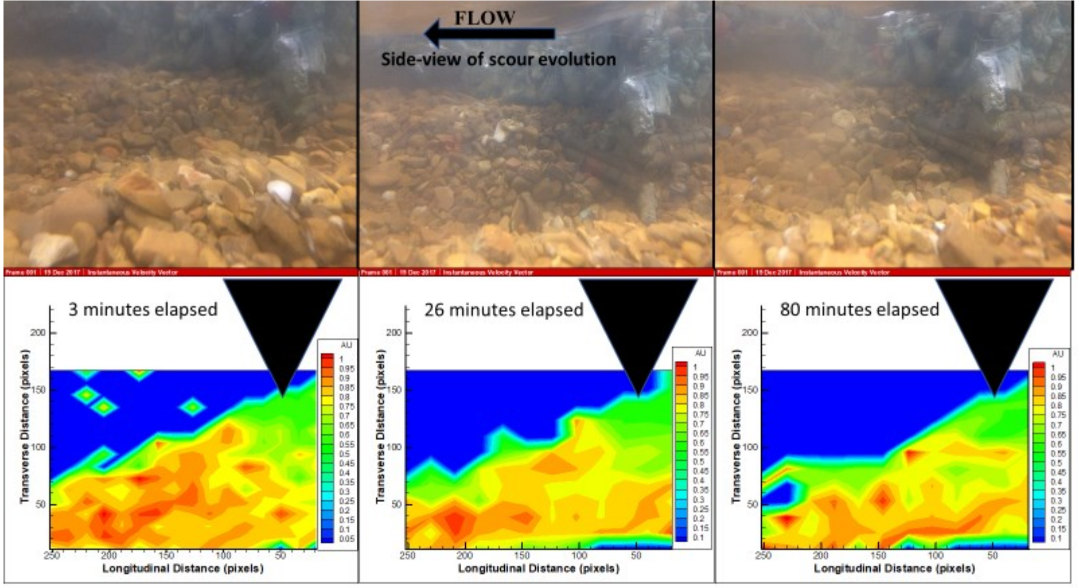

Figure 5.15. Side-view of clear water scour evolution and velocity distributions from LSIV (AU is the streamwise velocity in m/s)

In the live bed test, temporal monitoring of velocity at the toe of ELJ3 was conducted using single point measurements with the side-looking ADV. This data was processed to estimate the mean velocity sampled every 20 seconds, which is presented as a function of time in Figure 5.16. In this figure, the mean velocity near the ELJ toe was also observed to decrease and asymptotically reach an equilibrium value near about 90% of the bulk velocity.

5.2.3 Co-Evolution of Scour and Flow Velocity

The results from scour depth and flow velocity monitoring are now considered collectively since these variables are interrelated and co-evolving during scour evolution. In Figure 5.17, scour depth and mean velocity at the ELJ toe are presented together as a function of time for both the clear water and live bed scour tests. These figures show clearly that the decay of mean surface velocity at the toe of the ELJ structure is correlated with the increase in depth of scour. In the live bed case (Figure 5.17b), however, the flow velocity is observed to approach an equilibrium value at a later time after test initiation (at approximately 40 minutes in Figure 5.17) than the equilibrium scour depth does (at approximately 5 minutes in Figure 5.17). This behavior is attributed to a delay between the attainment of the maximum scour depth and attainment of the maximum scour hole volume since the scour hole widened for a longer period after the scour depth reached equilibrium (Papanicolaou et al., 2018).

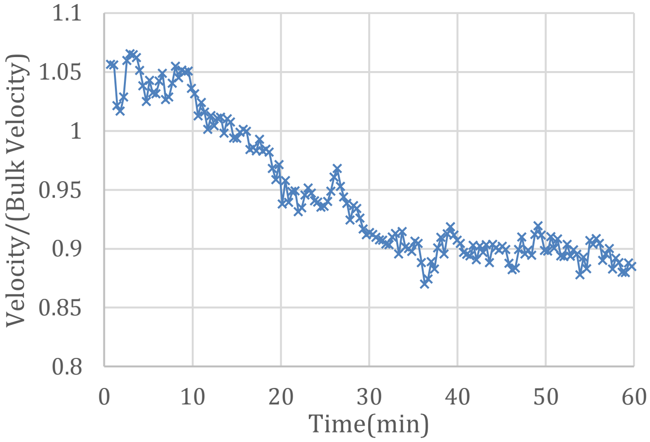

Figure 5.16. Temporal evolution of the mean streamwise velocity during live bed scour evolution; measured velocities are normalized with the bulk velocity.

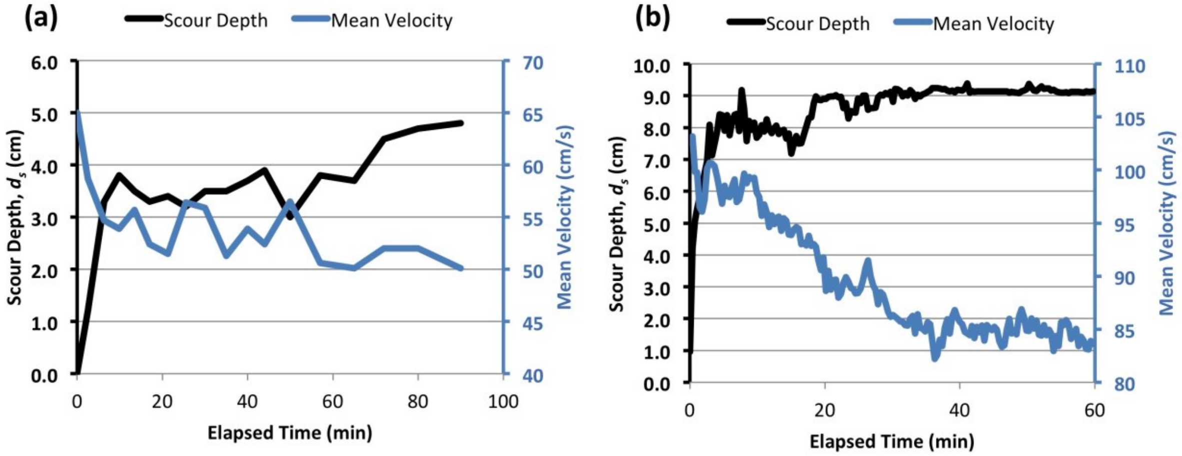

Figure 5.17. Co-evolution of scour depth and flow velocity near the toe of ELJ3 for the duration of scour tests in the (a) clear water and (b) live bed tests.

5.3 Conclusions for Objective 3

1. Sonar depth-sensing probes can be used to monitor scour hole evolution even in the presence of a rapidly varied and temporally evolving water surface profile.
2. Maximum scour depth evolution around an ELJ in a gravel bed river follows a logarithmic shape since it increases rapidly at the initial portion of the test and then increases more slowly until equilibrium is reached.
3. The flow field features and velocity magnitudes around an ELJ evolve as scour evolves and both asymptotically approach an equilibrium value.
4. Scour depth and water surface velocity near an ELJ are co-evolving variables that were correlated through the unique monitoring conducted in this experimental study.

6. Objective 4: Development of Generic Scour Equations for Predicting Scour Depth Around ELJs in Gravel Bed Rivers

6.1 Review of Scour Prediction Approaches

Questions often arise as to the applicability of existing methods for estimating the maximum scour depth, d_{sm}, at porous structures in gravel bed rivers. In particular, the effects on d_{sm} from changes in structure porosity and from increased particle interlocking in non-uniform gravels are minimally understood (Papanicolaou et al., 2018). While many formulas can predict d_{sm} at impermeable bridge abutments in sand bed rivers, they have been minimally tested at ELJs in a gravel bed. The present research addresses this critical gap and considers four existing scour prediction formulas (presented in Table 6.1) in order to evaluate their performance and potential adaptation for predicting scour around porous deflector structures in a gravel bed.

The first formula (equation 6.1) was developed by Papanicolaou et al. (2004) to predict d_{sm} at a permeable WSDOT barb in a gravel bed. This method was developed from dimensional analysis with the Buckhingham π theorem and expresses the dimensionless scour depth as a function of a modified Froude number (or discharge intensity), the relative roughness and the geometric standard deviation of the gravel material (Maxwell and Papanicolaou, 2001). The dimensionless terms in this formula are applicable to gravel bed streams and account for the influences of particle non-uniformity on d_{sm}.

The second formula (equation 6.2) was developed by Ettema et al. (2010) for application to abutment scour by computing localized scour depth as an amplification of the contraction scour. Thus, by including the amplification coefficient, α, this formula accounts for the effects of macro turbulence developing in the vicinity of the structure to scour. Because of the physical meaning associated with the α coefficient, this approach may enable more direct consideration of changes in flow-structure interactions (e.g., due to changes in structure porosity) when estimating scour.

The third and fourth formulas (equations 6.3 and 6.4) are the methods developed by Melville and Coleman (2000) and presented in HEC-18 (FHWA, 2012; TRB, 1989). Both of these empirical methods were developed for bridge abutment scour in a sand bed and employ empirically defined *K*-factors that account for the effects on scour depth from multiple sources (e.g., flow depth, projection length, flow intensity, sediment characteristics, structure shape, and structure alignment).

Table 6.1. Scour formulas evaluated for performance at permeable structures in a gravel bed.

Equation	Reference	Formula
6.1	Papanicolaou et al. (2004)	$\frac{d_{sm}}{H}\sigma_g^{1/2} = 3.02\left[\frac{Q}{\sqrt{gH^5}}\left(\frac{d_{50}}{H}\right)^{1.5}\right]^{0.2054}$
6.2	Ettema et al. (2010)	$\frac{d_{sm}}{H} = \left[\alpha\left(\frac{\tau_0}{\tau_{cr}}\right)^{\frac{3}{7}}\left(\frac{q_b}{q_0}\right)^{\frac{6}{7}} - 1\right]$ (a)* $\frac{d_{sm}}{H} = \left[\alpha\left(\frac{q_b}{q_0}\right)^{\frac{6}{7}} - 1\right]$ (b)*
6.3	Melville and Coleman (2000)	$d_{sm} = K_{yL}K_I K_d K_s K_\vartheta K_G K_t$
6.4	HEC-18 (FHWA, 2012; TRB, 1989)	$\frac{d_{sm}}{H} = 2.27K_1K_2\left(\frac{L}{H}\right)^{0.43} Fr^{0.61} + 1$

*Equation 6.2(a) is applicable to clear water scour and equation 6.2(b) is applicable to live bed scour.

List of Symbols:

B	- channel width
B_b	- obstructed width at the water surface level
d_{50}	- median sediment size
d_{sm}	- maximum scour depth
Fr	- Froude number [= $U_{bulk}/(gH)^{0.5}$]
g	- acceleration of gravity
H	- approach flow depth
K_1	- coefficient for structure shape [Table 8.1 in FHWA, 2012]
K_2	- coefficient for angle of the upstream structure face to flow [= $(\theta/90)^{0.13}$]
K_{yL}	- depth-size factor [p. 218, Melville and Coleman (2000)]
K_I	- flow intensity factor [pp. 220-1, Melville and Coleman (2000)]
K_d	- sediment size factor [p. 223, Melville and Coleman (2000)]
K_S	- abutment shape factor [p. 225, Melville and Coleman (2000)]
K_ϑ	- abutment alignment factor [pp. 227/500, Melville and Coleman (2000)]
K_G	- channel geometry factor [p. 227, Melville and Coleman (2000)]
K_t	- time factor [p. 230, Melville and Coleman (2000)]
L	- length of active flow obstructed by the structure
q_0	- approach flow discharge per unit width [= Q/B]
q_b	- discharge per unit width in the contracted section [= Q/B_b]
Q	- flow discharge
S_0	- channel slope
α	- scour amplification coefficient [Ettema et al. (2010)]
θ	- angle of the upstream ELJ face relative to the downstream bank [i.e., $\theta<90°$ if points downstream]
ρ	- fluid density
ρ_s	- sediment density
σ_g	- geometric standard deviation of the sediment size distribution
τ_0	- approach flow bed shear stress [= $\rho g R_h S_0$]
τ_{cr}	- critical shear stress for incipient bedload motion of d_{50} size sediment [=$\tau_{cr}^*((\rho_s-\rho)gd_{50})$]
τ_{cr}^*	- critical Shields parameter for d_{50} size sediment

6.2 Performance Assessment at Porous Structures in a Gravel Bed

The performance of each scour formula (Table 6.1) was evaluated based on the percent error in predicting experimental d_{sm} values. This evaluation was made for the present ELJ data at both clear water, CW, and live bed, LB, scour conditions (i.e., data from Section 4.2). In addition, CW scour data at a permeable WSDOT barb in a gravel bed were included for comparison in this analysis son (Papanicolaou et al., 2018).

The d_{sm} prediction errors for equations (6.1)-(6.4) are summarized in Table 6.2 and are shown in Figure 6.1 by comparison of experimental and predicted values. The following key observations are made from this analysis:

1. All formulas overestimate d_{sm} at the ELJ by 95% or more;
2. All formulas except equation (6.1) overestimate d_{sm} at the Barb by 12%-70% on average;
3. d_{sm} overestimation is greater at the ELJ than the barb by 80% or more; and,
4. Equation (6.4) performs poorly for all data and overestimates d_{sm} at the ELJ by 250% or more.

Table 6.2. d_{sm} prediction errors around porous structures in a gravel bed.

	Percent error		
Formula	**ELJ CW**	**ELJ LB**	**Barb CW**
Equation 6.1: Papanicolaou et al. (2004)	105%	126%	-2% ± 14%
Equation 6.2: Ettema et al. (2010)	124%	95%	21% ± 17%
Equation 6.3: Melville and Coleman (2000)	129%	96%	12% ± 18%
Equation 6.4: HEC-18 (FHWA, 2012; TRB, 1989)	262%	279%	70% ± 27%

Note: $\tau_{cr}^* = 0.06$ from the Shields diagram

Since these experiments were all performed with non-uniform sediment of similar σ_g and only equation (6.1) accounts for this parameter, a portion of the d_{sm} overestimation is attributed to the effects of sediment gradation and increased particle interlocking. However, the 80% separation between the ELJ and Barb dataset errors is not initially explained since equations (6.1)-(6.4) account for numerous factors that could influence d_{sm} (i.e., flow depth, projection length, flow intensity, sediment characteristics, structure shape, and structure alignment). Therefore, the observed separation between the ELJ and Barb datasets is most likely attributed to the effects of structure porosity since the ELJ has a higher porosity (about 70%) than the gravel barb structure (about 30%-40%). This interpretation is based on findings in the literature that increasing structure porosity can decrease backwater effects, limit streamline constriction at the structure and lower the shear stress amplification at the structure nose (Manners et al., 2007; Papanicolaou et al., 2004; Papanicolaou et al., 2018; Xu and Liu, 2017).

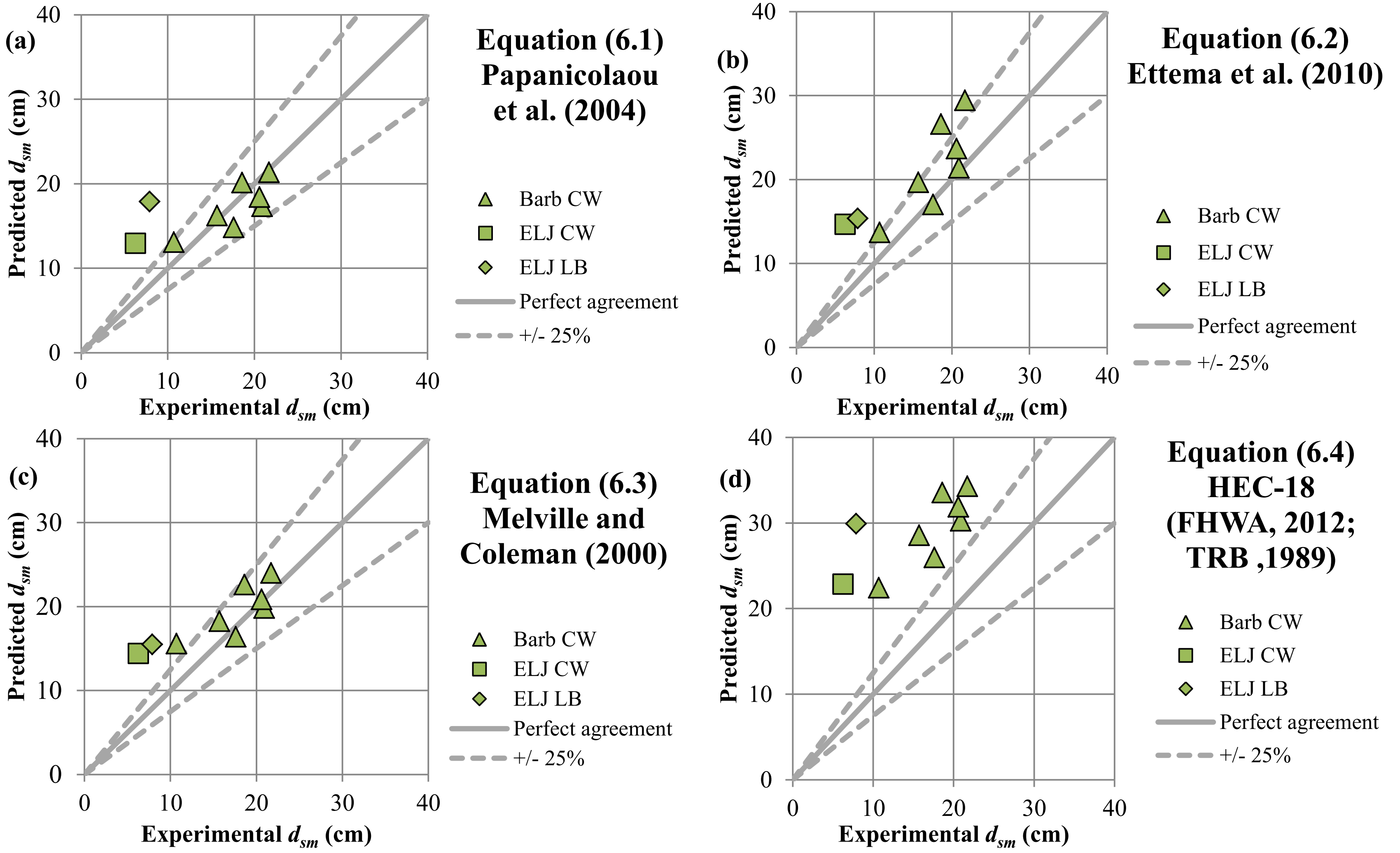

Figure 6.1. Comparison between experimental and predicted maximum scour depths, d_{sm}, for four formulas: (a) Papanicolaou et al. (2004); (b) Ettema et al. (2010); (c) Melville and Coleman (2000); and, (d) HEC-18 (FHWA, 2012; TRB, 1989).

6.3 Enhanced Formulas for Predicting Scour at Porous Structures in a Gravel Bed

Based on the conclusions that d_{sm} overestimations (i.e., Figure 6.1) are attributed to sediment gradation and structure porosity effects, modifications to equations (6.1)-(6.4) are investigated in order to minimize d_{sm} overestimation by accounting for these factors.

Sediment non-uniformity effects on d_{sm} are accounted for by employing the *K*-factor developed in previous research. This factor is defined as $K_\sigma = 1/\sqrt{\sigma_g}$ (Maxwell and Papanicolaou, 2001; Euler et al., 2011) and can be multiplied to the right hand side of equations (6.2)-(6.4) in order to correct for the effects of sediment gradation. Since the effects of structure porosity on scour have been not been well investigated in the literature, two possible formula modification approaches have been developed and tested here.

Formula Modification Approach 1: Develop a new *K*-factor, K_p, that accounts for the effects of structure porosity on scour (outlined below in Section 6.3.1).

- This approach integrates over the effects of structure porosity on the three-way interaction of the flow, structure and scour hole.
- K_p is estimated based on comparisons of scour at structures of different porosity.

Formula Modification Approach 2: Develop a new coefficient, $C_{\alpha,p}$, that accounts for the effects of structure porosity on the amplification coefficient, α, in the Ettema et al. (2010) scour formula (outlined below in Section 6.3.2).

- This approach accounts for the effects of structure porosity on scour via alteration of the two-way interaction of the structure with the flow.
- $C_{\alpha,p}$ can be estimated based on comparisons of either scour or flow at structures of different porosity.

6.3.1 Formula Modification Approach 1

The new *K*-factor, K_p, is defined similar to Melville (1992; 1997) as:

$$K_p = \frac{d_{sm,p}}{d_{sm,imp}} \tag{6.5}$$

where $d_{sm,p}$ is the maximum scour depth at a permeable structure and $d_{sm,imp}$ is the maximum scour depth at an impermeable structure of identical geometry under identical flow conditions.

K_p was determined using the present experimental data (i.e., $d_{sm,p}$) and estimating $d_{sm,imp}$ with equations (6.2) and (6.3) (after including the K_σ factor). Equations (6.2) and (6.3) were used to estimate $d_{sm,imp}$ since they were developed using impermeable abutment data and performed similarly for the porous structure data (i.e., Figure 6.1 and Table 6.2). Also, the effects of structure submergence were isolated in this analysis by estimating K_p for unsubmerged test conditions. The results of this analysis are presented in Table 6.3, which yield average estimates of $K_p = 0.55$ and $K_p = 0.88$ for the ELJ and Barb datasets, respectively.

Table 6.3. K_p estimates for the ELJ and Barb.

Data	K_p ($d_{sm,imp}$ from equation 6.2)	K_p ($d_{sm,imp}$ from equation 6.3)
ELJ	0.54	0.53
Barb	0.94	0.82

6.3.2 Formula Modification Approach 2

The coefficient, $C_{\alpha,p}$, used to correct α for the effects of structure porosity is defined as:

$$C_{\alpha,p} = \frac{\alpha_p}{\alpha_{imp}} \tag{6.6}$$

where α_p is the α value at a permeable structure and α_{imp} is the α value at an impermeable structure of identical geometry under identical flow conditions. Three methods based on both flow and scour are employed to estimate $C_{\alpha,p}$ and are outlined in Table 6.4.

Table 6.4. Methods used to estimate $C_{\alpha,p}$ at porous structures.

Method 1: Use estimate of α_p based on maximum scour depth a) Fit α in equation (6.2) to match the experimental $d_{sm,p}$ (after correcting with K_σ). This is denoted as $\alpha_{p,scour}$. b) Estimate α_{imp} from Ettema et al. (2010). c) Calculate $C_{\alpha,p}$ using equation (6.6) with α values from steps (a) and (b).
Method 2: Use estimate of α_p based on bed shear stress estimates from flow a) Estimate the bed shear stress at equilibrium scour condition near the permeable structure, τ_p, using flow measurements (see Section 7.2 and equation 7.6). b) Calculate shear stress in a long contraction at identical d_{sm}, τ_{LC} (equation 7.6). c) Use the results from (a) and (b) to calculate α_p with $\alpha_p = \left(\tau_p / \psi \tau_{LC}\right)^{3/7}$ (i.e., equation C10). Assume $\psi = 0.5$ for correcting the equilibrium shear stress at localized scour conditions (Section 7.2; Dey and Barbhuiya, 2005). d) Estimate α_{imp} from Ettema et al. (2010). e) Calculate $C_{\alpha,p}$ using equation (6.6) with values from steps (c) and (d).
Method 3: Estimate $C_{\alpha,p}$ by comparing bed shear stresses at a permeable and an impermeable structure a) Assume that the bed shear stress near a structure is proportional to the near-bed turbulent kinetic energy, k (e.g., Biron et al., 2004; Bennett et al., 2015). b) Estimate the maximum k near a permeable structure, k_p, and near an impermeable structure, k_{imp}, with identical geometry and under identical flow conditions. c) Calculate $C_{\alpha,p}$ using $C_{\alpha,p} = \left(k_p / k_{imp}\right)^{3/7}$ (modified from equation C11).

The resulting estimates of $C_{\alpha,p}$ are summarized in Table 6.5. In the present experiments, the $C_{\alpha,p}$ estimates based on both scour and flow corresponded well (within 8%), which confirms that this method can capture changes in d_{sm} by accounting for changes in flow-structure interactions. Moreover, $C_{\alpha,p}$ was also estimated at a porous ELJ with Method 3 using data from Xu and Liu (2017). All $C_{\alpha,p}$ estimates for the ELJs agree within ± 10% (Table 6.5), which supports the interpretation that the low scour depths at the ELJ in this study were influenced by structure porosity effects on the surrounding flow field.

Table 6.5. Estimates of α amplification coefficients and the correction coefficient for porous structure effects, $C_{\alpha,p}$.

Reference	Structure(s)	Scour Condition	Structure porosity	α_p: $\alpha_{p,scour}$	α_p: $\alpha_{p,flow}$	α_{imp}	$C_{\alpha,p}$ Methods	$C_{\alpha,p}$
Present study	ELJ	CW	≈ 0.72	1.56	1.43	2.25	1; 2	0.64-0.69
Present study	ELJ	LB	≈ 0.72	1.79	1.72	2.40	1; 2	0.72-0.75
Xu and Liu (2017)	ELJ/ Abutment	None	≈ 0.63/ = 1.0	-	-	-	3	0.65-0.75
Papanicolaou et al. (2018)	Barb	CW	≈ 0.3-0.4	2.04	2.16	2.20	1; 2	0.93-0.98

6.3.3 Enhanced Scour Formulas

Based on the formula modification approaches investigated in Sections 6.3.1 and 6.3.2, two new scour formulas are developed and recommended (Table 6.6) for scour prediction at porous structures in gravel bed rivers. Due to their added features, we call these formulas hereafter "enhanced formulas."

1. A modified version of the Papanicolaou et al. (2004) formula that incorporates the K_p correction for structure porosity effects (equation 6.7).
2. A modified version of the Ettema et al. (2010) formula that incorporates the K_σ correction for sediment non-uniformity effects and the $C_{\alpha,p}$ correction for structure porosity effects (equation 6.8).

The parameterization of equation (6.7) is sound (Maxwell and Papanicolaou, 2000) and the benefit of this formula is that it is easy to use with limited flow and bed data. Equation (6.8), on the other hand, requires more stream reach information than equation (6.7), but is particularly useful for minimizing scour overestimation when structures are submerged (Papanicolaou et al., 2018).

The d_{sm} predictions from equations (6.7) and (6.8) are compared with experimental values in Figure 6.2, which shows that errors are minimized with these enhanced formulas. Equations (6.7) and (6.8) predict all d_{sm} values to within 36% and 23%, respectively.

Table 6.6. Modified formulas for scour prediction at permeable structures in a gravel bed.

Equation	Modified From	Formula	Notes
6.7	Papanicolaou et al. (2004)	$\frac{d_{sm}}{H}\sigma_g^{1/2} = 3.43K_p\left[\frac{Q}{\sqrt{gH^5}}\left(\frac{d_{50}}{H}\right)^{1.5}\right]^{0.2054}$	$K_p = 0.55$ for dolotimber ELJ $K_p = 0.88$ for rock barb
6.8	Ettema et al. (2010)	$\frac{d_{sm}}{H} = K_\sigma\left[C_{\alpha,p}\alpha_{imp}\left(\frac{\tau_0}{\tau_{cr}}\right)^{\frac{3}{7}}\left(\frac{q_b}{q_0}\right)^{\frac{6}{7}} - 1\right]$ (a) $\frac{d_{sm}}{H} = K_\sigma\left[C_{\alpha,p}\alpha_{imp}\left(\frac{q_b}{q_0}\right)^{\frac{6}{7}} - 1\right]$ (b)	$C_{\alpha,p} = 0.68$ for dolotimber ELJ $C_{\alpha,p} = 0.93$ for rock barb

Note: Equation (6.8a) is applicable to clear water scour and equation (6.8b) is applicable to live bed scour.

List of symbols:

B - channel width
B_b - obstructed width at the water surface level
$C_{\alpha,p}$ - coefficient to correct α based on the effects of structure porosity
d_{50} - median sediment size
d_{sm} - maximum scour depth
Fr - Froude number [$= U_{bulk}/(gH)^{0.5}$]
g - acceleration of gravity
H - approach flow depth
K_p - correction factor for structure porosity
K_σ - correction factor for sediment non-uniformity [$= 1/\sqrt{(\sigma_g)}$]
q_0 - approach flow discharge per unit width [$= Q/B$]
q_b - discharge per unit width in the contracted section [$= Q/B_b$]
Q - flow discharge
S_0 - channel slope
α_{imp} - shear stress amplification coefficient for an impermeable structure [i.e., Ettema et al., 2010]
σ_g - geometric standard deviation of the sediment size distribution
τ_0 - approach flow bed shear stress [$= \rho g R_h S_0$]
τ_{cr} - critical shear stress for incipient bedload motion of d_{50} size sediment [$=\tau_{cr}^*((\rho_s-\rho)gd_{50})$]
τ_{cr}^* - critical Shields parameter for d_{50} size sediment

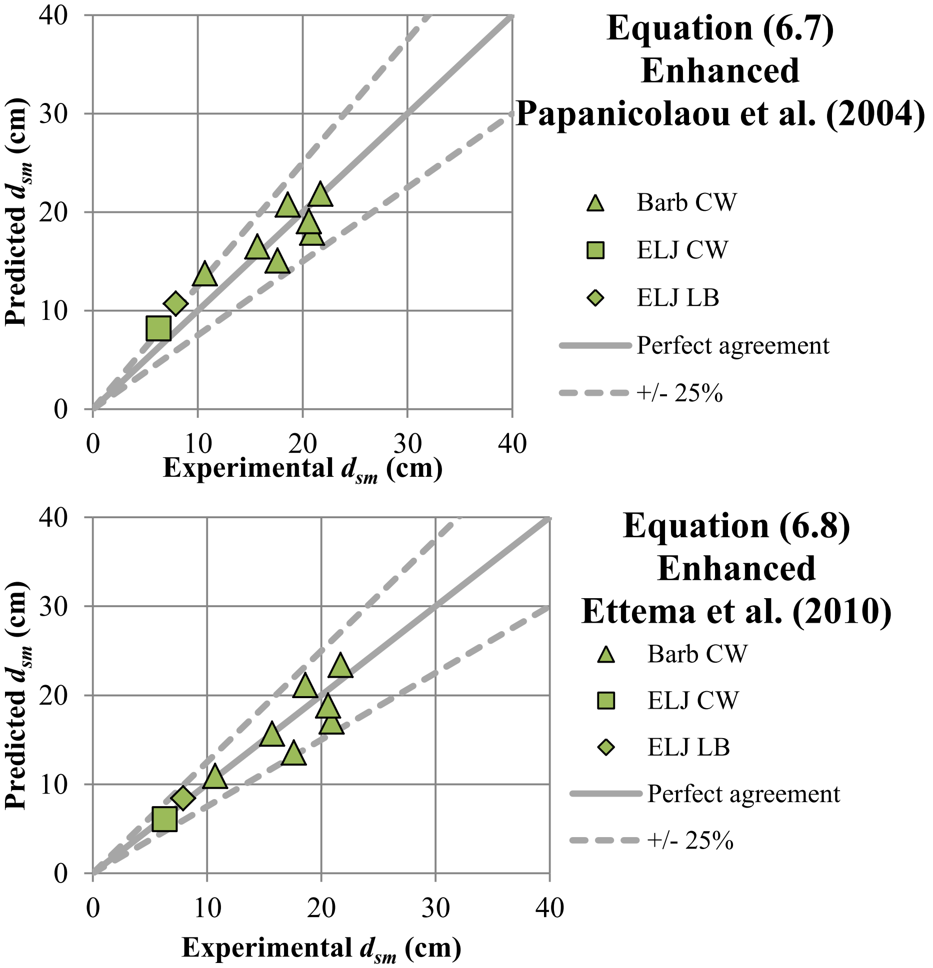

Figure 6.2. Comparisons of experimental and predicted maximum scour depths, d_{sm}. (a) Predictions from the enhanced Papanicolaou et al. (2004) formula; and (b) predictions from the enhanced Ettema et al. (2010) formula.

6.4 Prototype Scour Predictions

Maximum scour depth predictions at the prototype ELJ3 were made using the two enhanced formulas (equations 6.7 and 6.8) and are presented in Table 6.2. This table was populated using the stage-discharge curve (Figure 3.2) and the ratio H_t/H, which was assumed equal to 1.18 for all flow conditions (see Section 3.1.1). In equation (6.8), the contraction ratio q_b/q_0 (= B/B_b) was computed for unsubmerged ELJ conditions (i.e., $H_t/d_t < 1$) by using the ELJ3 projection length (68 ft) and the total channel width at ELJ3 (500 ft). For fully submerged conditions (i.e., $H_t/d_t > 1$), B/B_b was taken equal to unity (Papanicolaou et al., 2018).

Table 6.6. Predicted scour depths at the prototype ELJ3 using equations (6.7) and (6.8).

Flow event	Flow discharge, Q (cfs)	Approach flow depth, H (ft)	Flow depth at ELJ3, H_t (ft)	Contraction ratio, B/B_b (-)	Pred. d_{sm} – eq. (6.7) (ft)	Pred. d_{sm} – eq. (6.8), (ft)
2-year	33,000	8.0	9.5	1.16	8.2	6.5
	40,000	9.5	11.2	1.16	9.0	9.0
10-year	55,000	11.0	13.0	1.00	9.8	8.4

Note: α_{imp} = 2.6 (Ettema et al., 2010)

The d_{sm} predictions from equations (6.7) and (6.8) agreed to within 20% for all flow conditions considered. It is important to note, however, that the d_{sm} predictions from equation (6.8) approached a maximum value at a discharge of about 40,000 cfs and were fairly constant above this discharge. Papanicolaou et al. (2018) similarly observed a relatively constant d_{sm} around a permeable barb as the discharge increased. Moreover, their study showed how this behavior was related to the reduction in flow contraction as structure submergence increased. Therefore, the d_{sm} behavior predicted by equation (6.8) is attributed to the effects of overtopping and the implications of the changing B/B_b ratio when H_t/d_t is greater than 1. The ability of equation (6.8) to capture these overtopping effects is one of its key benefits since this can minimize the overdesign of structures for stability during very high flows.

6.4 Conclusions from Objective 4

1. Scour formulas from Papanicolaou et al. (2004), Ettema et al. (2010), Melville and Coleman (2000) and HEC-18 (FHWA, 2012; TRB, 1989) were tested with the present data. All formulas overpredicted the maximum scour depth at an ELJ in a gravel bed by 95% or more.
2. Enhanced versions of the Papanicolaou et al. (2004) and Ettema et al. (2010) formulas were developed for application to porous structures in a gravel bed. These formulas predict experimental maximum scour depths to within 35%.
3. Maximum scour depth predictions were made for the prototype by using the enhanced formulas and considering a range of flow conditions.
4. The enhanced Papanicolaou et al. (2004) was recommended for scour estimation with limited flow and bed data and the enhanced Ettema et al. (2010) formula was recommended for limiting scour overestimation in cases when structures are submerged.

7. Objective 5: Formulation of a Decay Function for Predicting Scour and Flow Co-Evolution

7.1 Overview of the Decay Function

In order to increase the accuracy of scour predictions and to better predict the likelihood of structural failure for given flow conditions, a better understanding of the hydraulic load, or bed shear stress, applied to sediment near a structure is needed. If the changes in bed shear stress during scour progression can be accurately predicted, then forecasts of maximum scour depth can be made when the critical shear stresses for a certain vertical soil profile are known. The main benefits of this approach are its sound physical basis that can be adapted with minimal alteration to different conditions (e.g., types of structures), its ability to limit the number of empirical coefficients with uncertain physical meaning, and its ability to account for differences in material properties within the vertical soil profile at a structure. Thus, this approach may help prevent the common overestimation of scour depth around porous ELJ structures in gravel bed rivers.

By building on the FHWA decay function scour prediction approach, which employs the predescribed principles (Annandale and Smith, 2001), recent research has investigated the decay of bed shear stress associated with scour hole development around bridge piers in a sand bed (Li, 2016). In this method, the instantaneous bed shear stress, τ, is normalized with the minimum bed shear stress, τ_{min}, associated with the equilibrium scour to determine the bed shear stress amplification, τ_{amp}, at different points in time during scour evolution (equation 7.1).

$$\tau_{amp} = \tau/\tau_{min} \qquad (7.1)$$

The evolution of τ_{amp} is then paired with the dimensionless relationship:

$$d_s/d_{sm} \qquad (7.2)$$

where d_s is the instantaneous value of scour depth, and d_{sm} is the maximum scour depth at equilibrium. Following the work of Li (2016), the bed shear stress decay function is written in a generic form as follows:

$$\tau_{amp} = a * exp\,[b * (d_s/d_{sm})] \qquad (7.3)$$

The mathematical form of equation (7.3) implies that the coefficient a is equivalent to τ_{amp} at the initiation of the test and that τ_{amp} is equivalent to 1 at the equilibrium condition, i.e., at d_s/d_{sm} equal to 1. These conditions are expressed in equations (7.4) and (7.5), respectively.

$$\tau_{amp} = a * exp\,(b * 0\%) = a \qquad (7.4)$$

$$\tau_{amp} = a * exp\,(b * 100\%) = 1 \qquad (7.5)$$

By solving equation (7.5) for b, the relationship $b = ln(1/a)$ is determined. These relationships show that the decay function may be defined based on knowledge of τ_{min} and of τ at the start of the test, though a confirmation of the accuracy of this functional relationship for describing experimental data is necessary.

7.2 Development of the Decay Function at Porous Structures in a Gravel Bed

The decay function is developed for the present experiments to investigate its performance near permeable ELJs in a gravel bed by using the following equation for bed shear stress (Li, 2016):

$$\tau = \rho g(V{*}n)^2/(H)^{1/3} \qquad (7.6)$$

where V is the local bulk velocity, n is the Manning's roughness, H is the local flow depth, ρ is the fluid density and g is the acceleration of gravity. Equation (7.6) was applied to the data from this study (i.e., Section 5) by: (1) calculating H as the sum of the flow depth and scour depth (from sonar probes) at ELJ3 toe, and (2) calculating V from the measured surface velocity, V_{surf}, using $V = C_1 {*} V_{surf}$, where C_1 is a velocity correction coefficient. C_1 was estimated from velocity data taken at the toe of similar bank-attached deflector structures (Bennett et al., 2015; Duan et al., 2009). C_1 was estimated to be equal to 0.9 at the flat bed condition and equal to 0.75 at equilibrium scour. C_1 was assumed to vary linearly with d_s between these conditions.

The present clear water and live bed data are plotted in Figure 7.1. The coefficients a (i.e., τ_{amp} at the start of the test) and b (i.e., $ln(1/a)$) that define the specific decay functions for these experiments are presented in Table 7.1 along with the R^2 values showing goodness of fit. The lower quality of fit for the live bed experiment ($R^2 = 0.629$) is attributed to the slower decay of τ due to the lag between scour depth and velocity evolution (Section 5.5). Since the decay function coefficients were similar for both tests, however, an average function was fitted to the both datasets ($a = 2.75$; $b = -1.01$) and is plotted in Figure 7.1.

Table 7.1. Decay function coefficients for the present experiments.

Case	a	b	R^2
Clear water	2.92	-1.07	0.958
Live bed	2.58	-0.95	0.629

The measured τ_{min} values correspond to dimensionless bed shear stress of $\tau_{min}^* = 0.022$ and $\tau_{min}^* = 0.038$ for the clear water and live bed experiments, respectively. These values are less than the estimated critical shear stress for incipient bedload motion at the approach section (i.e., $\tau_{cr}^* = 0.045$), though this agrees with the findings of other research focused on localized scour (Dey and Barbhuiya, 2005; Li, 2016). Specifically, Dey and Barbhuiya (2005) recommended that τ_{min} be assumed equal to $\psi\tau_{cr}$ for clear water scour at bridge abutments, where ψ [≈ 0.5] is a correction factor that accounts for the effects of strong vortex flow on τ_{min}. The τ_{min} estimates from this approach are similar to the findings for the present clear water scour tests.

The present data are also compared in Figure 7.2 with the study of Li (2016), who investigated the decay function around a rectangular bridge pier in a sand bed, and with data from Papanicolaou et al. (2018), who investigated scour at a permeable WSDOT barb in a gravel bed. Overall, the decay function similarly describes all datasets (except for the present live bed condition), but the total shear stress decay was lower for experiments in gravel beds at porous structures. This suggests that shear stress decay during scour at porous structures in gravel bed rivers may occurs with a similar functionality to sand bed scour around a bridge pier, but with altered magnitude of total decay. This behavior is likely attributed to changes in shear stress amplification associated with differences in structure type and/or to the increased particle interlocking of non-uniform gravel particles. Future investigations of the near-bed turbulence characteristics and their connections with both temporally evolving and equilibrium scour characteristics are needed in order to understand the root of the observed differences.

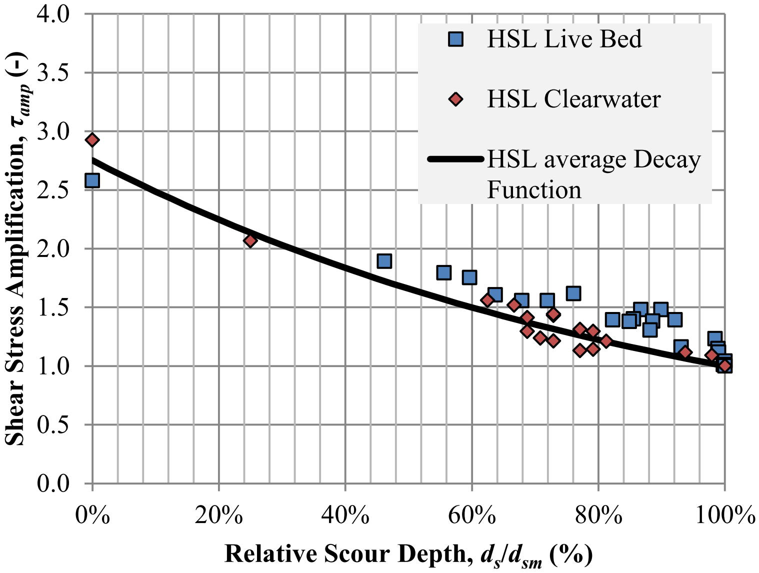

Figure 7.1. Decay function of bed shear stress around permeable ELJs in gravel bed.

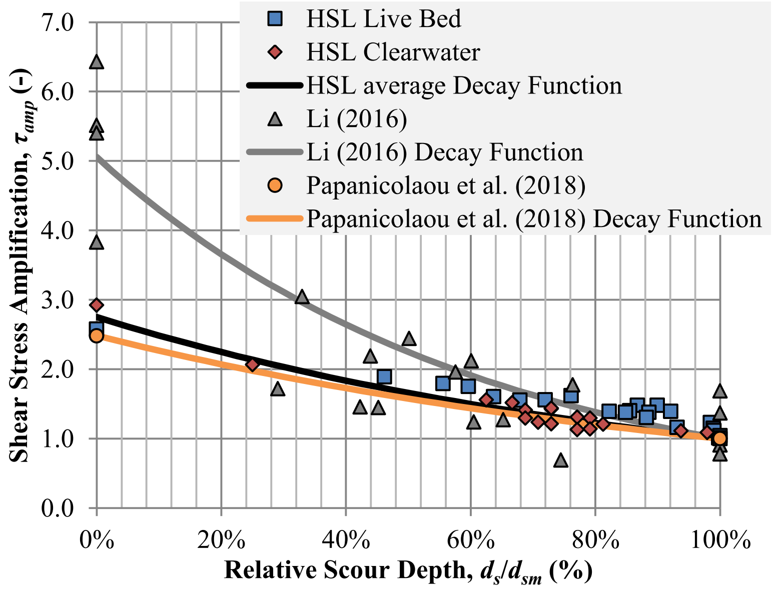

Figure 7.2. Decay function of bed shear stress around permeable ELJs in gravel bed and around a bridge pier in a sand bed (Li, 2016).

7.3 Decay Function Steps for Scour Prediction

In the following, a general approach for predicting d_{sm} based on the principles of the decay function is outlined. The approach employs the assumption that the applied shear stress at the toe of a partially submerged deflector ELJ is proportional to the contracted shear stress (similar the α coefficient employed in the Ettema et al. (2010) formula).

Step 1: Estimate the bed shear stress at the scour hole, τ, as a function of scour depth, d_s.

a) Determine the approach flow depth, H, and the discharge per unit width in the contracted section, q.

b) Compute τ for a range of d_s values using equation (7.7) and assuming $V = q/(H+d_s)$ at the location of maximum scour. Notes: Equation (7.7) results by combining equations (7.6) and (C10); α_p is estimated using α_{imp} from Ettema et al. (2010) and $C_{\alpha,p}$ from Table 6.6.

$$\tau = \alpha_p^{7/3}\psi\left[\rho g \frac{(Vn)^2}{(H+d_s)^{1/3}}\right] \tag{7.7}$$

Step 2: Estimate the profile of values for the gravel critical shear stress, τ_{cr}, at the scour hole

a) Estimate τ_{cr} for the gravel sediment size at unobstructed conditions.
    - One approach is to use the following equation (Suszka, 1991):

$$\tau_{cr}^{*} = 0.0851\left(H/d_{50}\right)^{-0.266} \tag{7.8}$$

b) Assume that τ_{cr} at the scour hole is equal to half of τ_{cr} under unobstructed conditions (Dey and Barbhuiya, 2005; Li, 2016).

Step 3: Estimate d_{sm} as the d_s value corresponding with the intersection of: (1) the τ vs. d_s curve and, (2) the profile of τ_{cr} values.

Figure 7.3 presents an example application of the above steps to predict d_{sm} at the ELJ clear water scour conditions. These calculations were made by assuming $\psi = 0.5$ (Dey and Barbhuiya, 2005) and using $\alpha_p = 1.54$ (fitted in Section 6.2), $\tau_{cr}^{*} = 0.022$ (determined in Section 7.2) and $n = 0.0235$ (calibrated with experimental data). This method predicts $d_{sm} = 6.6$ cm, which is within the range of experimentally observed values (i.e., $d_{sm} = 6.3$ cm ± 0.3 cm – Table 4.1).

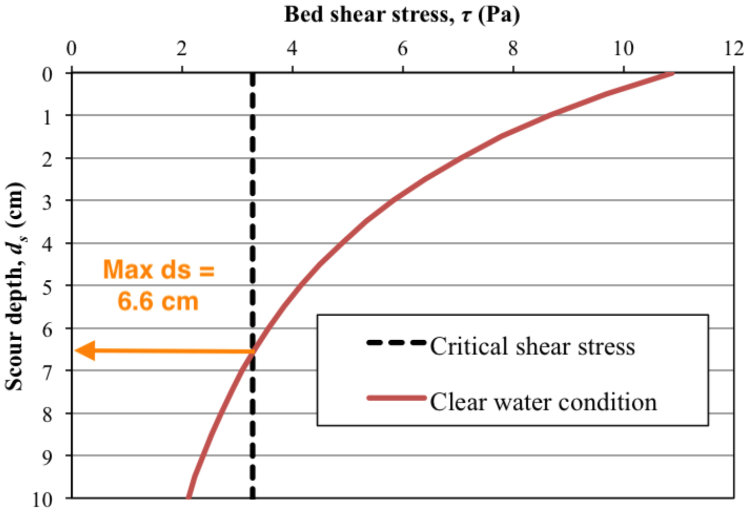

Figure 7.3. Application of the decay function method for predicting the maximum scour depth for the clear water scour condition.

7.3 Conclusions for Objective 5

1. The principles of the decay function, which relate the co-evolving bed shear stress and scour depth, were overviewed and a particular function describing the present experiments was determined.
2. A good correspondence was found between the magnitude of shear stress decay at a permeable ELJ and at a permeable rock barb during gravel bed scour, though this decay is much less than found at a bridge pier during sand bed scour. This is likely attributed to differences in structure type and to the effects of particle interlocking in a gravel bed.
3. A generic approach to employ the decay function principles for predicting the maximum scour depth was developed and outlined.

8. Objective 6: Assessment of Three-Dimensional Flow Features Around an Apex ELJ By Numerical Modeling

8.1 Overview and Methodology

In order to understand the flow field features developing around an apex ELJ and to determine potential implications for scour, numerical experiments were conducted to investigate the flow field around an ELJ resembling ELJ5 at the prototype. 3D Large Eddy Simulations (LES) were conducted for the 100-year flood, which was selected as a critical design flow for ELJ5 performance.

The LES simulation boundary conditions were determined using results from two-dimensional (2D) simulations conducted by the NHC group for the prototype ELJ reach using River 2D. The simulated 2D flow field at the 100-year flood is presented in Figure 8.1, which yielded LES simulation inflow conditions of *Re* = 10,000 and *Fr* = 0.32 for the LES modeling area indicated with a black box.

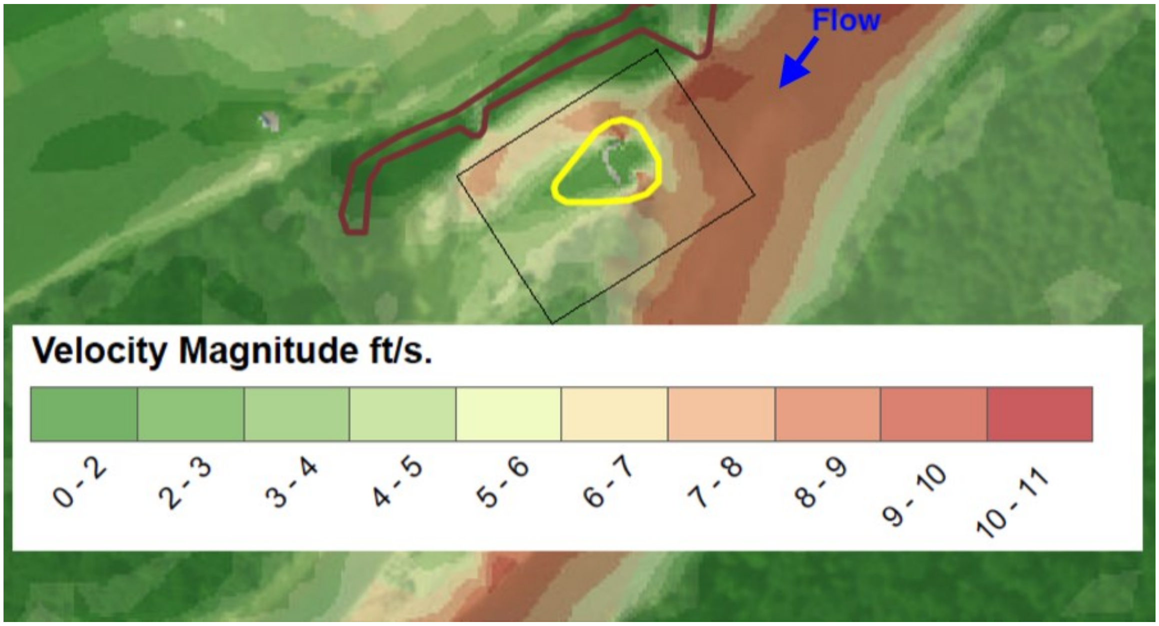

Figure 8.1. 2D flow field at the prototype during a 100 year flood simulated with River 2D; ELJ5 is outlined in yellow; the black box outlines the area investigated with 3D LES simulations.

The 3D turbulent flow field around ELJ5 was computed with wall-resolving LES by using a curvilinear-coordinate LES algorithm (Armenio and Piomelli, 2000). The bathymetry employed for the LES simulations (Figure 8.2) accurately mimics the bathymetry of ELJ5 but utilizes a simplified surrounding bathymetry due to numerical limitations. In the numerical code, the bed and structure were modeled as impermeable with a smooth surface and the water surface was modeled with a frictionless rigid lid in order to lower computational cost while allowing investigation of the relevant 3D flow features. The governing equations were integrated in this numerical code using a semi-implicit, finite difference, fractional step method (Zang et al., 1994). To ensure code stability, the simulation time step was maintained at a constant value and was selected to ensure that the Courant number was always less than 0.3. Constant flow discharge was maintained between the inlet and the outlet of the simulation section and the no-slip condition was fixed at the rigid boundary. For additional details concerning the methodology employed in this numerical code and examples of its usage for resolving the 3D flow fields around obstructions, see Bressan and Papanicolaou (2012) and Papanicolaou et al. (2018).

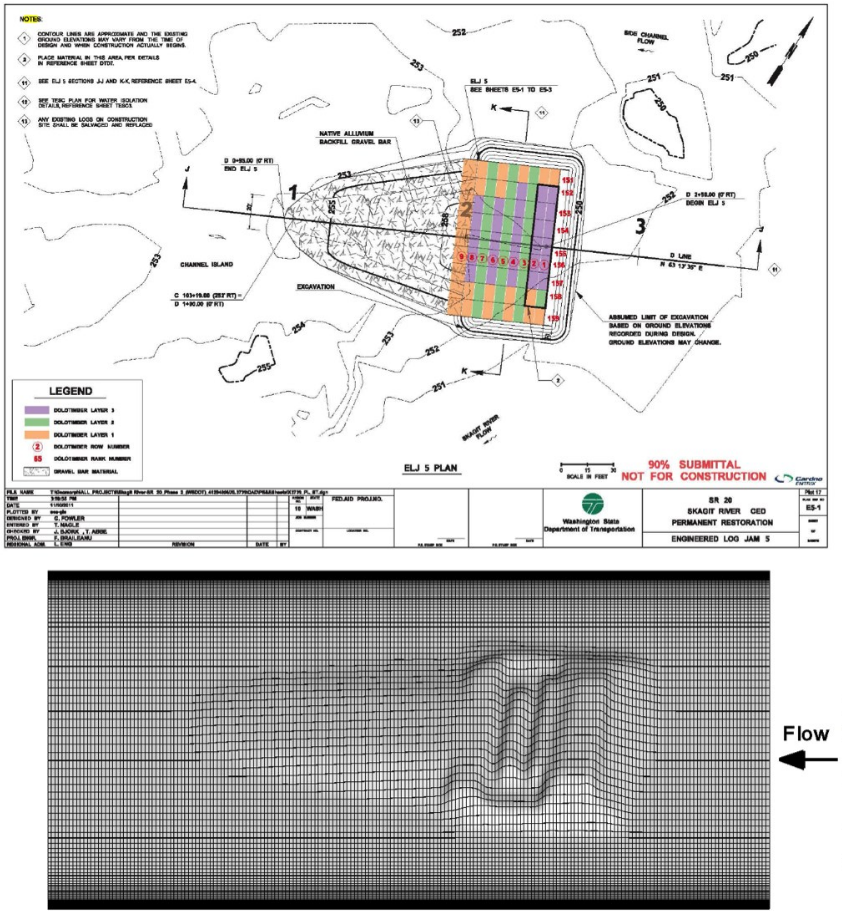

ELJ5 bathymetry and materials

Flow is from right to left

Flow

LES bathymetry representing the bathymetry above

Flow is from right to left

The planview is rotated 30 degrees to visualize the 3D bathymetry

Figure 8.2. Comparison of the prototype and LES bathymetries at ELJ5.

In order to visualize complex vortices in the 3D flow field, the *Q* criterion was employed (Dubief and Delcayre, 2000). This criterion is a powerful tool aiding vortex visualization via its ability to distinguish locations where the strength of rotation is greater than strain.

8.2 Results

The time-averaged flow features surrounding ELJ5 at the 100-year flood were first evaluated using a 2D flow field extracted from the 3D LES turbulent velocity simulations (Figure 8.3). Figure 8.3 shows the effects of ELJ5 on the surrounding flow field by creating flow acceleration at the structure sides and flow deceleration downstream of the unsubmerged ELJ's upstream face. The sides of ELJ5 are thus highlighted as zones of high scour potential (indicated in Figure 8.3) due to the accelerated flow velocities.

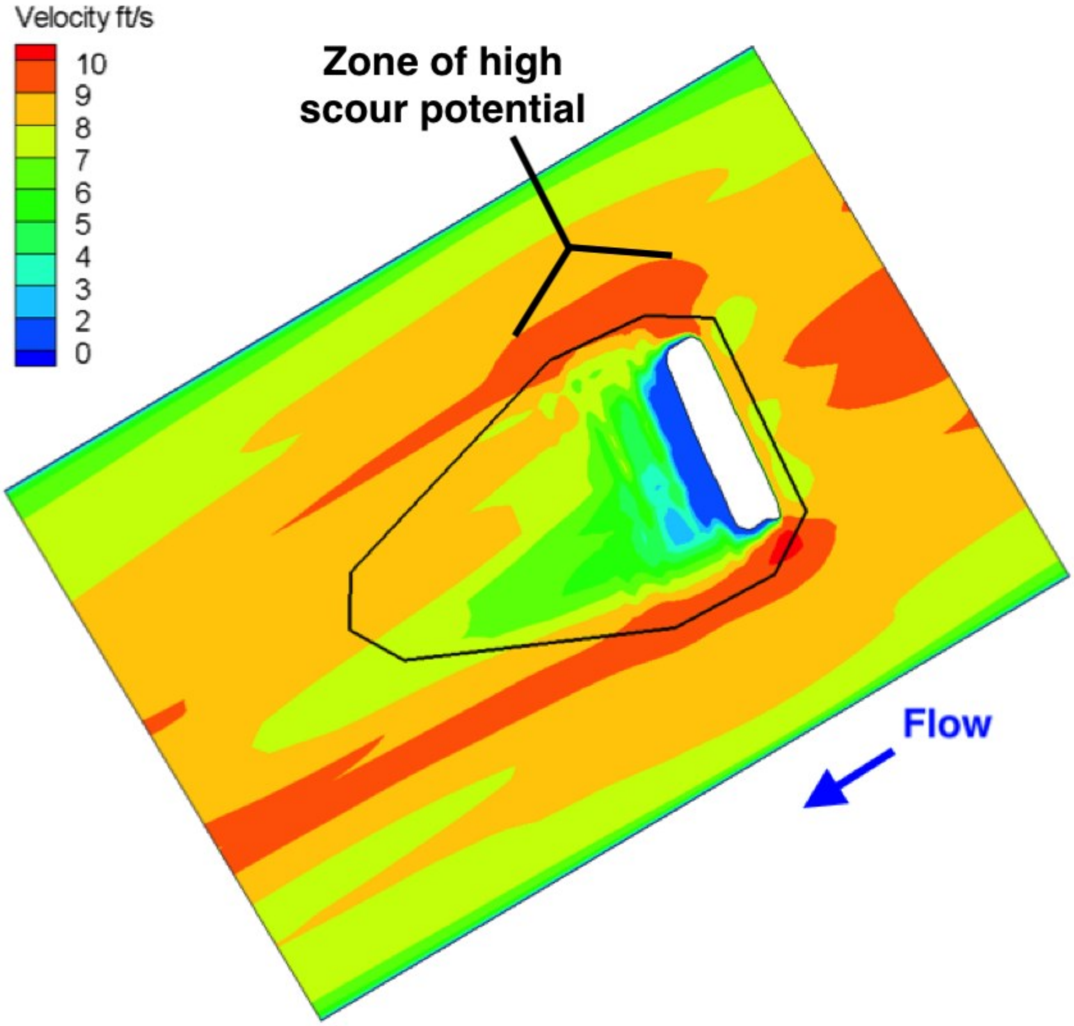

Figure 8.3. 2D flow field during a 100-year flood extracted from a 3D LES simulation.

To visualize complex 3D flow features developing around ELJ5, the flow streamlines were plotted overlaying the transparent 2D velocity map in both plan view (Figure 8.4) and perspective view (Figure 8.5). These streamlines allowed the visualization of three principle vortices forming around ELJ5, which are labeled V1, V2, and V3. The first two principle vortices (V1 and V2) develop at the downstream edge of ELJ5 on its two sides, which is where the streamlines wrap around the downstream corners of the structure. The third principle vortex (V3) develops in the flow recirculation region located downstream of the ELJ's upstream face. Since vortices V1 and V2 are located near the accelerated flow regions at the sides of the ELJ, they may impact sediment mobility and scour development in these areas. Due to their location at the downstream end of ELJ5, it is possible that the characteristics of these vortices affect scour pool development in the region downstream of the structure (e.g., see Figs. 5 & 7 in Abbe and Montgomery, 1996). These scour features could have implications for fish habitat and structural stability.

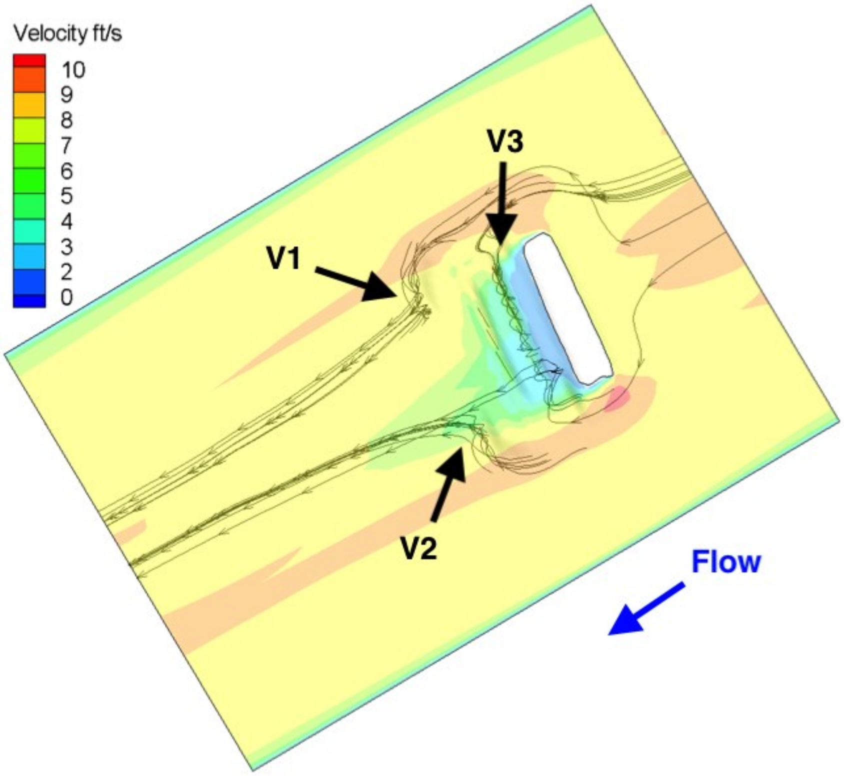

Figure 8.4. Plan view of the flow velocities and streamlines during a 100-year flood extracted from a 3D LES simulation; three principle vortices (V1, V2, V3) are visualized.

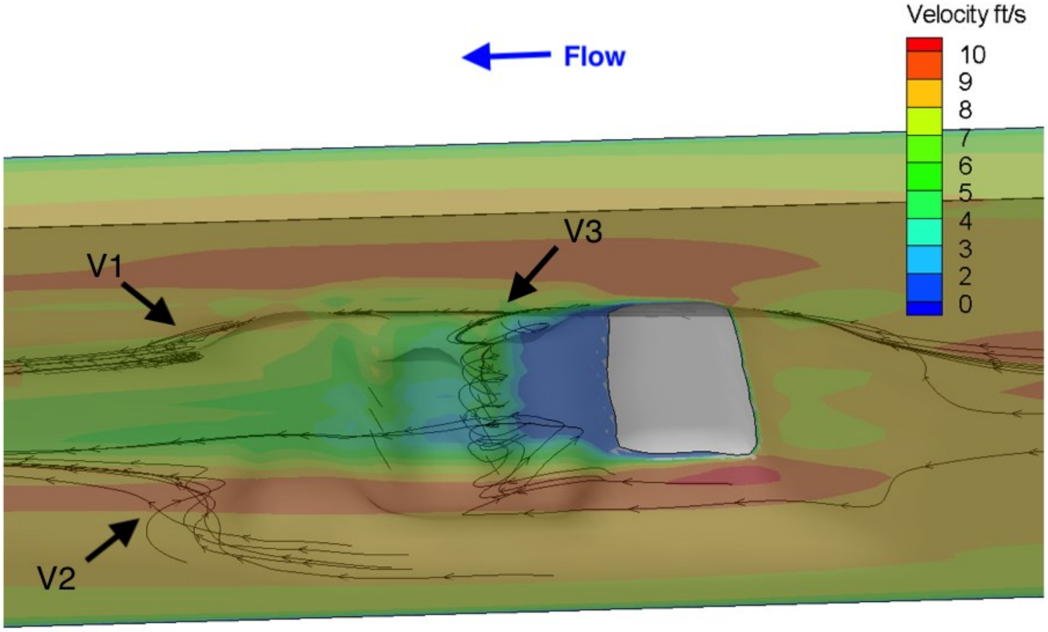

Figure 8.5. Perspective view of the flow velocities and streamlines during a 100-year flood extracted from a 3D LES simulation; three principle vortices (V1, V2, V3) are visualized.

To further investigate the complex 3D features of the flow field around ELJ5, the *Q* criterion was employed in Figure 8.6 to visualize vortex structures. In addition to vortices V1, V2 and V3,

Figure 8.6 highlights the locations where a detached shear layer (DSL) forms. In general, a DSL forms at the intersection between regions of high and low flow velocity and is a common feature observed around flow obstructions (e.g., Fox et al., 2005a, b; Papanicolaou et al., 2018). The high complexity of the DSL features that are visualized in Figure 8.6 is attributed to the complex geometry of ELJ5, i.e., the complex distribution of structure edges along the surface of ELJ5.

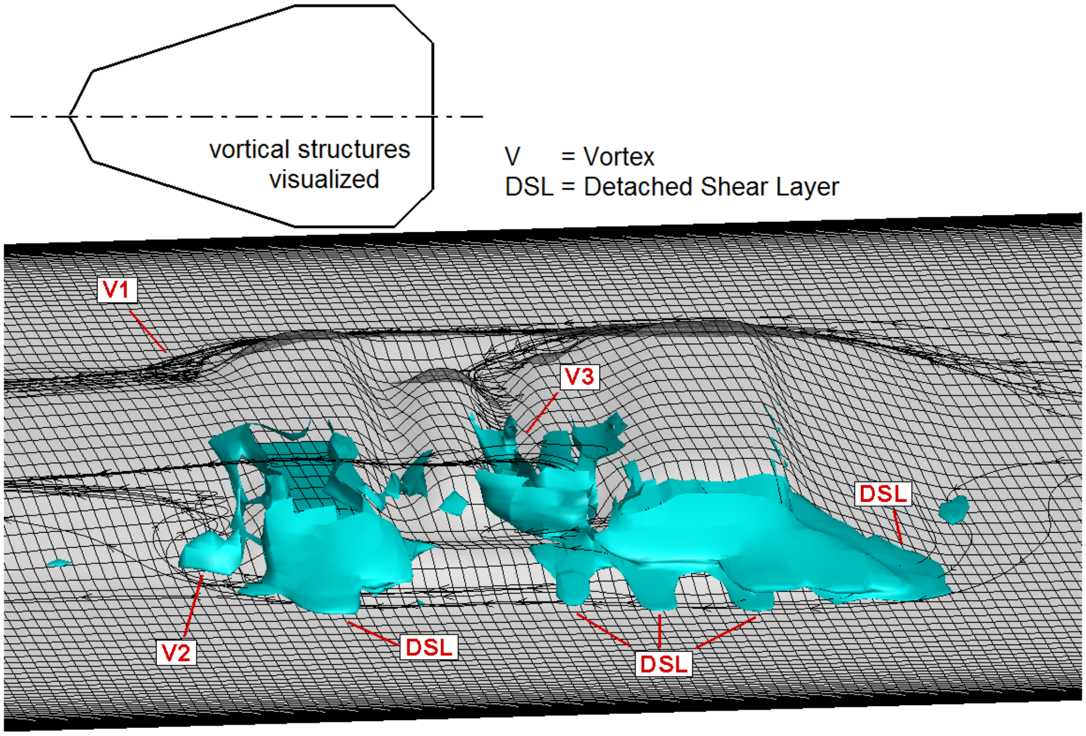

Figure 8.6. Perspective view of the streamlines and vortical structures (visualized with the Q criterion) around ELJ5; light blue surfaces correspond to isosurfaces of $Q = 0$; vortical structures are visualized only for half of ELJ5.

Figure 8.7 presents a final visualization of the 3D flow structure in the vicinity of ELJ5 by showing vertical cross-section plots of velocities and streamlines. These cross sections specifically illustrate the recirculation vortices that develop downstream of the faces and steps in the complex ELJ5 geometry, which are not visible with 2D models.

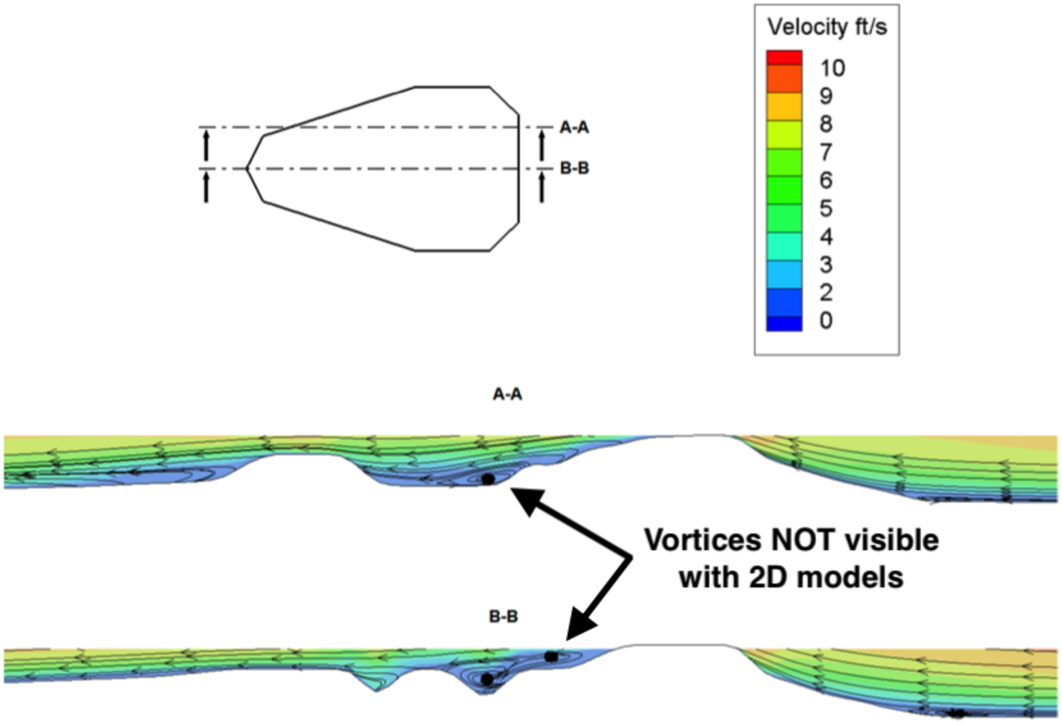

Figure 8.7. Vertical cross-sections along the longitudinal axis of the ELJ5 structure to visualize vortices and streamlines.

8.3 Conclusions for Objective 6

1. The two sides of ELJ5, and particularly the upstream ELJ corners, were highlighted as critical locations for evaluation of bed scour and ELJ stability because of the accelerated flow velocities occurring in these regions.
2. 3D LES simulations allowed visualization of complex and important flow features around ELJ5 that are not captured by 2D models.
3. Three principle vortices were visualized around ELJ5. The first two principle vortices developed at the downstream corners of ELJ5. These vortices were near the zones of accelerated velocities at the structure sides and may have implications for scour hole development in these areas. The third principle vortex developed in the flow recirculation region located just downstream of the front ELJ face.
4. A detached shear layer (DSL) with complex features developed around ELJ5. The complexity of the DSL is attributed to the complex geometry of ELJ5.

9. Conclusions

Observations
This research project has provided unique insights about the feedbacks between an ELJ structure, the flow, and a gravel bed under clear water and live bed scour conditions. The findings in this research showed that the scour hole in the vicinity of an experimental deflector ELJ obtained a conical shape and that the average time to reach an equilibrium state was about 20 minutes. Flow measurements complemented the scour measurements and provided rare data for describing the decay function of the bed shear stress in a gravel bed as the scour hole develops.

Multiple scour formulas (Papanicolaou et al., 2004; Ettema et al., 2010; Melville and Coleman, 2000; FHWA, 2012) were tested for predicting the maximum scour depths at clear water and live bed scour. All formulas overestimated scour at the porous dolotimber ELJ in a gravel bed by 95% or more. Thus, enhanced versions of the Papanicolaou et al. (2004) and Ettema et al. (2010) formulas were developed based on theoretical delineation of parameters and supported by the experimental data. These enhanced formulas (provided in Table 6.6) account for the effects of dolotimber ELJ structure porosity and sediment non-uniformity on scour. The parameterization of equation (6.7) is sound and this formula is easy to use with limited flow and bed data. Equation (6.8) requires more stream reach information than equation (6.7), but is particularly useful for minimizing scour overestimation when structures are submerged (Papanicolaou et al., 2018).

Analysis of the temporal scour and velocity measurements obtained in this study allowed the development of a decay function for describing for the first time the bed shear stress evolution during scour evolution at a porous structure in a gravel bed. In addition, a general approach for applying the decay function to predict scour prediction around a deflector ELJ has been outlined (Section 7.3). Information from these experiments will be used in determining how to advance existing scour estimation methods, particularly the Scour Depth Limit State Design Approach (Figure 9.1).

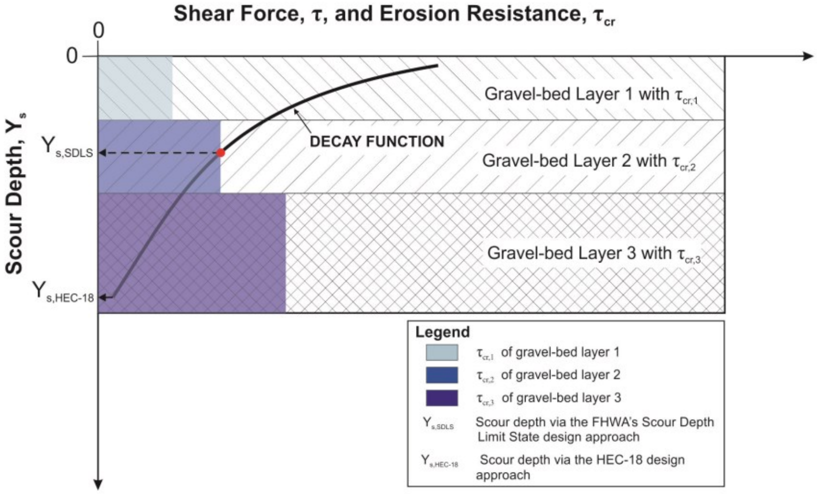

Figure 9.1. Shear Decay Function Concept in a Layered Gravel Bed River (adopted from FHWA). The Shear Force Applied by the Flow (Black Line) Decays as the Scour Hole Develops. The Equilibrium Scour Depth is Reached when the Shear Force Applied by the Flow no Longer Exceeds the Erosion Resistance of the Gravel Bed Layer (Red Dot in the Figure) (from Papanicolaou, Ettema, Kramer, Tsakiris, 2018).

Future Work

The findings of this research show the value and importance of using a detailed experimental design that considers aspects of hydraulic-dynamic similarity for flow and sediment. Although the experiments were not an exact similarity replication of the prototype, the study nonetheless ensured that the submergence of the structure, average structure layering and porosity, as well as bed sediment grain size distribution mimicked the prototype conditions. Flume limitations such as channel width did not permit the exact replication of the complex plan-form geometry found in the prototype, which would be beneficial to consider in future research.

A frequently expressed concern is that existing scour equations overestimate depths of scour at structures placed in gravel bed rivers. We believe that this concern has some validity, but that it is inaccurately or incompletely posed. Future research should investigate further the differentiation of clear water from live bed scour in a gravel bed. In addition, Table 9.1 lists all unique (or rather unique) aspects of gravel bed rivers that may affect depth of scour and need to be considered in future research.

Table 9.1. Unique Aspects of Gravel Bed Rivers as it Pertains to Scour at Hydraulic Structures.

	Aspect	Comment on Physical Process at Play
1	Non-uniformity of bed particles	The larger median particle diameter, d_{50}, means that far greater size ranges occur with gravels than with sands.
2	Interlocking of particles	Interlocking makes particle entrainment more difficult.
3	Large relative roughness	Particle diameter relative to structure width influences energy dissipation within the scour region formed at a structure; larger relative roughness causes more energy dissipation.
4	Armoring of bed surface	An armor layer that is resistant to erosion heightens the clear water scour condition estimated.
5	Layering of bed particles	Given the dynamic nature that gravel beds form and bars shift, layering of particles may occur, affecting scour and stress decay.
6	Sand content in the gravel bed	Sand depresses the reference Shields stress value for particle entrainment and thus affects the onset for grain movement.
7	Bar formation	Bar presence may concentrate flow.
8	High velocities of approach flow	Gravel bed rivers typically convey high-velocity flows, in keeping with the coarseness of bed particles and slope.
9	Possible super-critical (Froude number) approach flow	Design flows can be super-critical (following item 8).
10	Intense turbulence at, and around, hydraulic structures	High velocities generate more intense turbulence and affect frequency of vortex shedding.
11	Relatively weak bank materials	Bank material near bridges on gravel bed rivers usually lack clay particles, and thus are relatively weak.

This research is a first step in utilizing nearly synchronous flow and depth measurements and can become the keystone for future experimental work investigating the connections of scour volume evolution with evolving bed shear stress. This can be expressed generically as follows:

$$V_s(t) = f\left[\langle \boldsymbol{\tau} \rangle (t)\right] \tag{9.1}$$

where $V_s(t)$ is the scour volume at time t and $<\tau>(t)$ is the spatially averaged bed shear stress around a hydraulic structure at time t. By appropriately considering the physical processes leading to scour volume evolution, this approach has potential for minimizing scour depth overestimation and for limiting the need for empirical adjustment coefficients that often have uncertain physical meaning.

This research has highlighted the need to better understand the effects of ELJ characteristics (e.g., porosity, shape, placement either as bank-attached or in-stream) to shear stress amplification in order to aid scour prediction at complex prototype structures. In addition, future scour research needs to consider the ability of dolotimber ELJ structures to deform. Such deformation is illustrated in Figure 9.2, which shows that one dolo was mobilized from the toe of ELJ3 at the Skagit River prototype and was deposited in the region where a scour hole is expected. Moreover, the dolotimber matrix at the ELJ toe appears to have deformed, likely through some collapse of the structure toe following the development of a scour hole. This example highlights the importance for future research to account for the interplay between scour evolution and ELJ deformation when predicting both scour depth and structural stability, which has not been considered in previous studies.

Figure 9.2. Aerial photo showing a dolo that was mobilized during a previous flow event and apparent toe deformation at ELJ3 (posted on June 28, 2016 – https://www.youtube.com/watch?v=-uc6exYwgxU&t=97s).

References

Abbe, T. B., and Montgomery, D. R. (1996). “Large woody debris jams, channel hydraulics and habitat formation in large rivers.” Regulated Rivers Research & Management, 12(23), 201-221.

Abbe, T., Bjork, J., Zehni, A. and Park, J. (2011). “New Innovative, Habitat-Creating Bank Protection Method.” World Environmental and Water Resources Congress 2011, doi:10.1061/41173(414)211.

Ahmed, F. and Rajaratnam, N. (2000). “Observations on flow around bridge abutment.” Journal of Engineering Mechanics, 126(1), 51-59.

Allan, J.D., and Flecker, A.S. (1993). “Biodiversity conservation in running waters.” Bioscience, 43, 32–43.

Amoser, S. and Ladich, F. (2005). “Are hearing sensitivities of freshwater fish adapted to the ambient noise in their habitats?” The Journal of Experimental Biology, 208, 3533-3542.

Anderson, A.G., Paintal, A.S. and Davenport, J.T. (1970). “Tentative design procedure for riprap-lined channels.” NCHRP Report No. 146.

Armenio, V., and Piomelli, U. (2000). “Lagrangian mixed subgrid-scale model in generalized coordinates.” Flow, Turbulence and Combustion, 65(1), 51-81.

Bagočius, D. (2015). “Piling Underwater Noise Impact on Migrating Salmon Fish during Lithuanian LNG Terminal Construction (Curonian Lagoon, Eastern Baltic Sea Coast).” Marine Pollution Bulletin, 92(1-2), 45–51., doi: 10.1016/j.marpolbul.2015.01.002.

Barbhuiya, A.K., and Dey, S. (2003). “Vortex flow field in a scour hole around abutments.” International Journal of Sediment Research, 18(4), 310-325.

Barbhuiya, A.K., and Dey, S. (2004). “Local scour at abutments: A review.” Sadhana, 29(5), 449-476.

Bennett, S.J., Ghaneeizad, S.M., Gallisdorfer, M.S., Cai, D., Atkinson, J.F., Simon, A., and Langendoen, E.J. (2015). “Flow, turbulence, and drag associated with engineered log jams in a fixed-bed experimental channel.” Geomorphology, 248, 172-184.

Benson, I. A., Valentine, E. M., Nalluri, C. and Bathurst, J. C. (2001). “Stabilizing the sediment bed in laboratory flumes.” Journal of Hydraulic Research, 39(3), 279–282.

Bettess, R., et al. (1984). "Initiation of sediment transport in gravel streams.” Proceedings of the Institution of Civil Engineers, 77(4), 523-524.

Blodgett, J.C. (1986). Rock riprap design for protection of stream channels near highway structures, Vol. 1—Hydraulic characteristics of open channels. U.S. Geological Survey. Water-Resources Investigations Report 86–4127. Denver, CO.

Bocchiola, D. (2011). “Hydraulic characteristics and habitat suitability in presence of woody debris: a flume experiment.” Advances in Water Resources, 34(10), 1304-1319.

Bolton, S., Watts, A., Sibley, T., and Dooley, J. (1998). A pilot study examining the effectiveness of engineered large woody debris (ELWD TM) as an interim solution to lack of LWD in streams. EOS, Trans. of the Amer. Geophysical Union 79(45): F346.

Bressan, F., and Papanicolaou, A.N. (2012). “Scour around a variably submerged barb in a gravel bed stream.” River Flow 2012, CRC Press, London, 333-339.

Brooks, A.P., Abbe, T.B., Jansen, J.D., Taylor, M., and Gippel, C.J. (2001). “Putting the wood back into our rivers: An experiment in river rehabilitation.” Third Australian Stream Management Conference, Brisbane, Australia, August 27-29.

Brooks, A.P., Abbe, T., Cohen, T., Marsh, N., Mika, S., Boulton, A., Broderick, T., Borg, D., Rutherfurd, I. (2006). “Design guideline for the reintroduction of wood into Australian streams.” Land & Water Australia, Canberra.

Brownlie, W.R. (1981). “Prediction of flow depth and sediment discharge in open channels.” W. M. Keck Laboratory of Hydraulics and Water Resources Report, 43A. California Institute of Technology, Pasadena, CA.

Buffington, J.M. (1995). "Effects of hydraulic roughness and sediment supply on surface textures of gravel-bedded rivers. MS thesis. University of Washington.

Buffington, J.M., and Montgomery, D.R. (1997). “A systematic analysis of eight decades of incipient motion studies, with special reference to gravel- bedded rivers.” Water Resources Research, 33(8), 1993-2029.

Buffington, J.M. (1999). "The legend of AF Shields." Journal of Hydraulic Engineering, 125(4), 376-387.

Bunte, K., and Abt, S.R. (2001). “Sampling surface and subsurface particle-size distributions in wadable gravel-and cobble-bed streams for analyses in sediment transport, hydraulics, and streambed monitoring.” Gen. Tech. Rep. RMRS-GTR-74. Fort Collins,CO: U.S. Department of Agriculture, Forest Service, Rocky Mountain Research Station. 428 p.

Cardoso, A. H., and R. Bettess. (1999). “Effects of time and channel geometry on scour at bridge abutments.” Journal of Hydraulic Engineering, 125(4), 388-399.

Castro, J., and Sampson, R. (2001). “Incorporation of large wood into engineering structures.” Natural Resource Conservation Service Engineering Technical Note no 15.

Cederholm, C. J., et al. (1997). “Response of juvenile coho salmon and steelhead to placement of large woody debris in a coastal Washington stream.” North American Journal of Fisheries Management 17(4), 947-963.

Chang, H. H. (1998). Fluvial processes in river engineering, Krieger Publishing Company, Malabar, Florida

Chow, V.T. (2009). Open-Channel Hydraulics. The Blackburn Press, 2009 “Cle Elum River Instream Habitat and Side Channel Restoration Project.” Kittitas Conservation Trust, ENTRIX Environmental Consultants, 31 Jan. 2008, kittitasconservationtrust.org/cle-elum-river.php.

Coleman, S.E., Lauchlan, C.S., and Melville, B.W. (2003). "Clear-water scour development at bridge abutments." Journal of Hydraulic Research, 41(5), 521-531.

D’Aoust, S.G. (1998). Large woody debris fish habitat structure performance and ballasting requirements. Diss. University of British Columbia.

D'Aoust, S.G., and Millar, R.G. (2000). "Stability of ballasted woody debris habitat structures." Journal of Hydraulic Engineering, 126(11), 810-817.

Dey, S., and Barbhuiya, A.K. (2004). “Clear-Water Scour at Abutments in Thinly Armored Beds.” Journal of Hydraulic Engineering, 130(7), 622–634, doi:10.1061/(asce)0733-9429(2004)130:7(622).

Dey, S., and Barbhuiya, A.K. (2005a). “Time variation of scour at abutments.” Journal of Hydraulic Engineering, 131(1), 11–23.

Dey, S., and Barbhuiya, A.K. (2005b). “Flow Field at a Vertical-Wall Abutment.” Journal of Hydraulic Engineering, 131(12), 1126–1135, doi:10.1061/(asce)0733-9429(2005)131:12(1126).

Diab, R., Link, O. and Zanke, U. (2010). "Geometry of developing and equilibrium scour holes at bridge piers in gravel." Canadian Journal of Civil Engineering, 37(4), 544-552.

Drury, T. (1999). Stability and pool scour of engineered log jam structures in the North Fork Stillaguamish River, Washington. M.S. Thesis, University of Washington.

Duan, J.G., He, L., Fu, ,X., and Wang, Q. (2009). "Mean flow and turbulence around experimental spur dike." Advances in Water Resources, 32(12), 1717-1725.

Dubief, Y., and Delcayre, F. (2000). “On coherent-vortex identification in turbulence.” Journal of Turbulence, 1(11), 1-22.

Elhakeem, M., et al. (2017). “A Probabilistic Model for Sediment Entrainment: The Role of Bed Irregularity.” International Journal of Sediment Research, 32(2) 137–148, doi:10.1016/j.ijsrc.2016.11.001.

Ettema, R.E. (1980). “Scour at bridge piers.” Ph.D. Dissertation, The University of Auckland, Auckland, New Zealand.

Ettema, R., Kirkil, G., and Muste, M. (2006). “Similitude of large-scale turbulence in experiments on local scour at cylinders.” Journal of Hydraulic Engineering, 132(1), 33-40.

Ettema, R.E., Nakato, T., and Muste, M., (2010). NCHRP Report 24-20: ESTIMATION OF SCOUR DEPTH AT BRIDGE ABUTMENTS. Transportation Research Board of the National Academies, Washington D.C.

Eubanks, C., and Meadows, C. (2002). A soil bioengineering guide for streambank and lakeshore stabilization. Vol. 683. US Dept. of Agriculture Forest Service, Technology and Development Program.

Euler, T. and Herget, J. (2011). “Obstacle-Reynolds-number based analysis of local scour at submerged cylinders.” Journal of Hydraulic Research, 49(2), 267-271.

Federal Highway Administration (2012). “Evaluating scour at bridges, 5th Ed.” *Hydraulic Engineering Circular No. 18 (HEC-18)*, Publication No. FHWA-HIF-12-003, Washington, DC. (Arnesen, L.A., Zevenbergen, L.W., Lagasse, P.F., and Clopper, P.E.).

Fernandez Luque, R., and Van Beek, R. (1976). “Erosion and transport of bed-load sediment.” Journal of Hydraulic Research, 14(2), 127-144.

Ferro, V. (2003). "ADV measurements of velocity distributions in a gravel- bed flume." Earth Surface Processes and Landforms, 28.7: 707-722.

Fetherston, K.L., Naiman, R.J., and Bilby, R.E. (1995). "Large woody debris, physical process, and riparian forest development in montane river networks of the Pacific Northwest." Geomorphology, 13(1-4), 133-144.

Finney, K. (1993). "History of soil bioengineering." Eleventh annual California salmonid restoration federation conference, Eureka, CA.

Finnemore, E. J., and Franzini, J. B. (2002). Fluid mechanics with engineering applications, 9th Ed. McGraw-Hill.

Fox, J.F., Papanicolaou, A.N., Hobbs, B., Kramer, C., and Kjos, L. (2005a). "Fluid-sediment dynamics around a barb: an experimental case study of a hydraulic structure for the Pacific Northwest." Canadian Journal of Civil Engineering, 32(5), 853-867.

Fox, J.F., Papanicolaou, A.N., and Kjos, L. (2005b). “Eddy taxonomy methodology around a submerged barb obstacle within a fixed rough bed.” Journal of Engineering Mechanics, 10.1061/(ASCE)0733-9399(2005)131:10(1082), 1082-1101.

Fox, J.F., and Belcher, B.J. (2011). "Comparison of macroturbulence measured using decomposition of PIV, ADV and LSPIV data." Journal of Hydraulic Research, 49(1), 122-126.

Friedrich, H., Melville, B. W., Coleman, S. E., Nikora, V. I., and Clunie, T. M. (2005). Three-dimensional measurement of laboratory submerged bed forms using moving probes. In

Proceedings of XXXI International Association of Hydraulic Engineering and Research Congress (pp. 396-404).

Friedrich, H., Melville, B. W., Coleman, S. E., Clunie, T. M., Nikora, V. I., and Goring, D. G. (2006). Three-dimensional properties of laboratory sand waves obtained from two-dimensional autocorrelation analysis. In Int. Conf. on Fluvial Hydraulics, River Flow 2006, Lisbon, Portugal, 6-8 September 2006 (pp. 1013-1022).

Frissell, C.A., and Nawa, R.K. (1992). "Incidence and causes of physical failure of artificial habitat structures in streams of western Oregon and Washington." North American Journal of Fisheries Management, 12(1), 182-197.

Fujita, I., Muste, M. and Kruger, A. (1998). "Large-scale particle image velocimetry for flow analysis in hydraulic engineering applications." Journal of Hydraulic Research, 36(3), 397-414.

Gallisdorfer, M.S., et al. (2014). “Physical-Scale Model Designs for Engineered Log Jams in Rivers.” Journal of Hydro-Environment Research, 8(2), 115–128., doi:10.1016/j.jher.2013.10.002.

Gessler, J. (1971). "Beginning and ceasing of sediment motion." River mechanics 1: 7-1.

Ghodsian, M., and Tehrani, S.M.H. (2001). "Scour around groins." International Journal of Sediment Research, 16(1), 60-68.

Giri, S. and Shimizu, Y. (2005). “A method for local scour prediction at river structures considering time factor.” Annual Journal of Hydraulic Engineering, JSCE, 49, 781-786.

Green, T. PIV in practice (Doctoral dissertation, Luleå tekniska universitet), 2011.

Guan, D., Melville, B.W. and Friedrich, H. (2014). "Live-bed scour at submerged weirs." Journal of Hydraulic Engineering, 141(2), 04014071.

Hall, M. and Moler, S. (2006). “Mimicking Mother Nature.” Public Roads, Federal Highway Administration, 1 Jan., www.fhwa.dot.gov/publications/publicroads/06jan/05.cfm.

House, R., and Crispin, V. (1990). Economic analyses of the value of large woody debris as salmonid habitat in coastal Oregon streams. Bureau of Land Management.

Huijbers, C.M., Nagelkerken, I., Lossbroek, P.A.C., Schulten, I.E., Siegenthaler, A., Holderied, M.W., and Simpson, S.D. (2012). “A test of the senses: Fish select novel habitats by responding to multiple cues.” Ecology, 93(1), 46-55.

Ismael, A., et al. (2015). “Effect of Bridge Pier Position on Scour Reduction According to Flow Direction.” Arabian Journal for Science and Engineering, 40(6), 1579–1590, doi:10.1007/s13369-015-1625-x.

Jackson, E., Admiraal, D., Alexander, D., Stansbury, J., Guo, J., Rundkuist, D., Drain, M. (2009). “Thermal imaging for discharge and velocity measurements in open channels.” In: 33rd International Association of Hydraulic Research Symposium. International Association for Hydro-Environment Engineering and Research, Vancouver, Canada.

Judge, A. (2013). "Measurement of the hydraulic conductivity of gravels using a laboratory permeameter and silty sands using field testing with observation wells. University of Massachusetts Amherst.

Justice, C., et al. (2017). "Can stream and riparian restoration offset climate change impacts to salmon populations?" Journal of Environmental Management, 188, 212-227.

Kim, H.S., Kimura, I., and Shimizu, Y. (2016). “Experimental investigations of scour pools around porous obstructions.” Water, 8, 498 doi:10.3390/w8110498

Kimmerer, R.W., and Allen, T.F.H. (1982). "The role of disturbance in the pattern of a riparian bryophyte community." American Midland Naturalist, 370-383.

Kirkil, G., and Constantinescu, G. (2009). “Nature of flow and turbulence structure around an in-stream vertical plate in a shallow channel and the implications for sediment erosion.” Water Resources Research, 45, W06412, doi:10.1029/2008WR007363.

Koken, M., and Constantinescu, G. (2008). “An investigation of the flow and scour mechanisms around isolated spur dikes in a shallow open channel: 2. Conditions corresponding to the final stages of the erosion and deposition process.” Water Resources Research, 44, W08407, doi: 10.1029/2007WR006491.

Koken, M., and Constantinescu, G. (2014). “Flow and Turbulence Structure around Abutments with Sloped Sidewalls.” Journal of Hydraulic Engineering, 140(7), 04014031, doi:10.1061/(asce)hy.1943-7900.0000876.

Komar, P.D. (1987). "Selective gravel entrainment and the empirical evaluation of flow competence." Sedimentology, 34(6), 1165-1176.

Kothyari, U.C., Garde, R.C.J., and Ranga Raju, K.G. (1992). "Temporal variation of scour around circular bridge piers." Journal of Hydraulic Engineering, 118(8), 1091-1106.

Kothyari, U. C., and K. G. Ranga Raju. (2001), "Scour around spur dikes and bridge abutments." Journal of Hydraulic Research, 39(4), 367-374.

Kuhnle, R. A. (1993). Incipient motion of sand-gravel sediment mixtures, Journal of Hydraulic Engineering, 119, 1400-1415

Kuhnle, R.A., Alonso, C.V. and Shields, F.D. Jr. (2002). "Local scour associated with angled spur dikes." Journal of Hydraulic Engineering, 128(12), 1087-1093.

Kwan, T.F. (1988). "A study of abutment scour."

Lai, Y.G., et al. (2017). “Three-Dimensional Computational Modeling of Flows through an Engineered Log Jam.” World Environmental and Water Resources Congress 2017, doi:10.1061/9780784480625.003.

Landers, M., and Mueller, D. (1996). “Evaluation of Selected Pier-Scour Equations Using Field Data.” *Transportation Research Record: Journal of the Transportation Research Board*, 1523, 186–195, doi:10.3141/1523-23.

Latterell, J.J. (2005). The natural history and dynamics of large wood in the Queets River, Washington. Diss. University of Washington.

Lautz, L.K., Siegel, D.I., and Bauer, R.L. (2006). “Impact of debris dams on hyporheic interaction along a semi-arid stream.” Hydrological Processes, 20, 183-196.

Leu, J.-M., et al. (2008). “Hydraulic Characteristics of Flow over a Highly Permeable Porous Structure.” World Environmental and Water Resources Congress 2008, doi:10.1061/40976(316)211.

Lewis, L. (2000). Soil Bioengineering: An alternative for Roadside Management: A Practical Guide. San Dimas Technology & Development Center.

Li, C. (2016). “CFD Study of Decay Function of Wall Shear Stress with Scour around Complex-Shape Bridge Pier.” Ph.D. Dissertation, University of Nebraska - Lincoln.

Littell, J.S., et al. (2010). “Forest Ecosystems, Disturbance, and Climatic Change in Washington State, USA.” Climatic Change, 102(1-2), 129–158, doi:10.1007/s10584-010-9858-x.

“Lower Germany Creek Fish Assessment and Restoration.” Wild Fish Conservancy, Wild Fish Conservancy Northwest, 1 Sept. 2012, wildfishconservancy.org/projects/germany-creek.

Manners, R. B., Doyle, M.W., and Small, M.J. (2007). “Structure and hydraulics of natural woody debris jams.” Water Resources Research, 43(6), doi:10.1029/2006wr004910.

Maxwell, A.R., and Papanicolaou, A.N. (2001). “Step-pool morphology in high-gradient streams.” International Journal of Sediment Research, 16(3), 380-390.

McHenry, M., et al. (2007). "The physical and biological effects of engineered logjams (ELJs) in the Elwha River, Washington." Report to Salmon Recovery Funding Board and Interagency Committee for Outdoor Recreation, Port Angeles, WA: 82.

McQuivey, R.S. (1973). Summary of Turbulence Data from Rivers, Conveyance Channels, and Laboratory Flumes: Turbulence in Water. Vol. 802. US Government Printing Office.

Meffe, G.K. (1984). "Effects of abiotic disturbance on coexistence of predator- prey fish species." Ecology, 65(5), 1525-1534.

Melville, B.W (1993). "Closure to "Local Scour at Bridge Abutments" by BW Melville (April, 1992, Vol. 118, No. 4)." Journal of Hydraulic Engineering, 119(9), 1071-1073.

Melville, B.W., and Coleman, S.E. (2000). Bridge scour. Water Resources Publications, Highland Ranch, CO.

Molinas, A., Kheireldin, K., and Wu, B. (1998). "Shear stress around vertical wall abutments." Journal of Hydraulic Engineering, 124(8), 822-830.

Montgomery, D R, et al. (1996). "Stream-Bed Scour, Egg Burial Depths, and the Influence of Salmonid Spawning on Bed Surface Mobility and Embryo Survival." Canadian Journal of Fisheries and Aquatic Sciences, 53(5), 1061–1070, doi:10.1139/f96-028.

Montgomery, D.R., and Abbe, T.B (2006). "Influence of logjam-formed hard points on the formation of valley-bottom landforms in an old-growth forest valley, Queets River, Washington, USA." Quaternary Research, 65(1), 147-155.

Mosher, M.M. and Lunnum, K. (2003). Trees of Washington. Washington State University Extension Bulletin EB0440.

Neill, C. R. (1968). "Note on initial movement of coarse uniform bed-material." Journal of Hydraulic Research, 6(2), 173-176.

Nezu, I., and Nakagawa, H. (1986). "Investigation on Three-Dimensional Turbulent Structure in Uniform Open-Channel and Closed Duct Flows." Doboku Gakkai Ronbunshu, 369, 89–98, doi:10.2208/jscej.1986.369_89.

Nezu, I., and Sanjou, M. (2011). "PIV and PTV Measurements in Hydro-Sciences with Focus on Turbulent Open-Channel Flows." Journal of Hydro-Environment Research, 5(4), 215–230, doi:10.1016/j.jher.2011.05.004.

NHC. (2010). Hydrology Technical Memorandum for SR 20/Skagit River CED (MP 100.7), Northwest Hydraulic Consultants, Inc., October 12.

Oliveto, G., and Hager, W.H. (2002). "Temporal evolution of clear water pier and abutment scour." Journal of Hydraulic Engineering, 128(9), 811-820.

Papanicolaou, A. N., L. Kjos, and J. F. Fox. (2004). Investigation of flow and local scour characteristics around a partially submerged permeable WSDOT barb. Rep. WA-RD 581.1, Washington State Department of Transportation (TRAC).

Papanicolaou, A.N., and Maxwell, A.R. (2000). "Hydraulic performance of fish bypass-pools for irrigation diversion channels." Journal of Irrigation and Drainage Engineering, 126(5), 314-321.

Papanicolaou, A. N., et al. (2001). "Surface roughness effects in near-bed turbulence: Implications to sediment entrainment." Journal of Engineering Mechanics, 127(3), 211-218.

Papanicolaou, A. N., et al. (2011). "Depositional Patterns in Steep Mountainous Streams under Low Relative Submergence (LRS) Regime." World Environmental and Water Resources Congress 2011: Bearing Knowledge for Sustainability.

Papanicolaou, A.N., Bressan, F., Fox, J., Kramer, C.K. and Kjos, L. (2018). “Role of Structure Submergence on Scour Evolution in Gravel Bed Rivers: Application to Slope-Crested Structures” Journal of Hydraulic Engineering, 144(2), 03117008.

Parker, G., et al. (2003). “Effect of Floodwater Extraction on Mountain Stream Morphology.” Journal of Hydraulic Engineering, 129(11), 885–895, doi:10.1061/(asce)0733-9429(2003)129:11(885).

Parker, G., Klingeman, P.C., and McLean, D.G. (1982). “Bedload and size distribution in paved gravel-bed streams.” Journal of the Hydraulics Division, 108(4), 544-571.

Parker, G., and Wilcock, P.R. (1993). “Sediment Feed and Recirculating Flumes: Fundamental Difference.” Journal of Hydraulic Engineering, 119(11), 1192–1204, doi:10.1061/(asce)0733-9429(1993)119:11(1192).

Pattison, M. J. (2011). “Friction Velocity.” A-To-Z Guide to Thermodynamics, Heat and Mass Transfer, and Fluids Engineering, 2 Feb. 2011, doi:10.1615/atoz.f.friction_velocity.

Pess, G.R., Liermann, M.C., McHenry, M.L., Peters, R.J., and Bennett, T.R. (2012). “Juvenile salmon response to the placement of engineered log jams (ELJs) in the Elwha River, Washington State, USA. River Research and Applications, 28: 872-881.

Prancevic, Jeff P., and Michael P. Lamb. (2015). “Particle Friction Angles in Steep Mountain Channels.” Journal of Geophysical Research: Earth Surface, 120(2), 242–259, doi:10.1002/2014jf003286.

Raikar, R.V., and Dey, S. (2005). "Clear-water scour at bridge piers in fine and medium gravel beds." Canadian Journal of Civil Engineering, 32(4), 775-781.

Raudkivi, A.J. (1986). “Functional Trends of Scour at Bridge Piers.” *Journal of Hydraulic Engineering*, 112(1), 1–13, doi:10.1061/(asce)0733-9429(1986)112:1(1).

Raudkivi, A. J. and Ettema, R. (1977) “Effect of Sediment Gradation on Clear Water Scour” Journal of the Hydraulics Division, 103(10), 1209-1213.

Raudkivi, A.J., and Ettema, R. (1983). "Clear-water scour at cylindrical piers." Journal of Hydraulic Engineering, 109(3), 338-350.

Reyff, J.A. (2017). “A Brief History of Underwater Construction Noise.” The Journal of the Acoustical Society of America, 141(5), 3846-3846, doi:10.1121/1.4988574.

Rice, C. E., Kadavy, K. C., and Robinson, K. M. (1998). "Roughness of loose rock riprap on steep slopes." Journal of Hydraulic Engineering, 124(2), 179-185.

Robinson, L. (2002). The lowdown on riprap: option for preventing erosion in channels and streambanks. In Erosion Control. Forester Communications, Inc. Santa Barbara, CA.

Rosgen, D.L. (2001). "The cross-vane, w-weir and j-hook vane structures... their description, design and application for stream stabilization and river restoration." Wetlands Engineering & River Restoration, 1-22.

Rouse, H. (1939). "An analysis of sediment transportation in the light of fluid turbulence."

Sadeque, M.A.F., Rajaratnam, N., and Loewen, M.R. (2008). “Flow around cylinders in open channels.” Journal of Hydraulic Engineering, 134(1), 60-71.

Schultz, R. C., Collettil, J. P., Isenhart, T. M., Simpkins, W. W., Mize, C. W., and Thompson, M. L. (1995). “Design and placement of a multi-species riparian buffer strip system”. Agroforestry Systems, 29(3), 201-226.

Shields, A. (1936). "Application of similarity principles and turbulence research to bed-load movement." CalTech library.

Shields Jr, F.D., and Gippel, C.J. (1995). "Prediction of effects of woody debris removal on flow resistance." Journal of Hydraulic Engineering, 121(4), 341-354.

Shields Jr, F.D., Cooper, C.M. and Testa, S. (1995). "Towards greener riprap: environmental considerations from microscale to macroscale." River, coastal and shoreline protection: Erosion control using riprap and armourstone, 557-574.

Shields, Jr. F.D., et al. (2001). “Effect of Large Woody Debris Structures on Stream Hydraulics.” Wetlands Engineering and River Restoration, doi:10.1061/40581(2001)76.

Skagit River Bank Protection 90% Design Support: SR 20 at Milepost 100.7. Cardno Entrix, 2011, Skagit River Bank Protection 90% Design Support: SR 20 at Milepost 100.7.

Smith, M. E. (2004). “Noise-Induced Stress Response and Hearing Loss in Goldfish (Carassius Auratus).” Journal of Experimental Biology, 207(3), 427–435, doi:10.1242/jeb.00755.

Sommerfeld, A. (1908). "Ein beitrag zur hydrodynamischen erklaerung der turbulenten fluessigkeitsbewegungen." Atti del 4, 116-124.

Song, T., Graf, W.H., and Lemmin, U. (1994). "Uniform flow in open channels with movable gravel bed." Journal of Hydraulic Research, 32(6), 861-876.

SonTek. (1998). “Acoustical Doppler Velocimeter (ADV): Sampling Volume Size and Velocity Accuracy.” SonTek Technical Notes.

Streeter, V. L., and E. B. Wylie. (1979). "Fluid Mechanics, 562 pp."

Sturm, T.W. (2010). Open Channel Hydraulics. McGraw-Hill.

Suszka, L. (1991). “Modification of transport rate formula for steep channels. In: Armanini, A., Di Silvio, G. (eds) Fluvial Hydraulics of Mountain Regions. Lecture Notes in Earth Sciences, 37, Springer, Berlin, Heidelberg.

Suaznabar, O., Chen, Li. and Kerenyi, K. (2014). "Feather River Bridge Pier Scour Study."

Svensson, A. (2014). "Estimation of Hydraulic Conductivity from Grain Size Analyses." Chalmers University of Technology: Gothenburg, Sweden.

Svoboda, C. D., and Russell, K. (2011). "Flume analysis of engineered large wood structures for scour development and habitat." World Environmental and Water Resources Congress 2011: Bearing Knowledge for Sustainability.

Thompson, D.M. (2002). "Long-term effect of instream habitat-improvement structures on channel morphology along the Blackledge and Salmon rivers, Connecticut, USA." Environmental Management, 29(2), 250-265.

Transportation Research Board, 1989, "Abutment Scour Prediction," Presentation, Transportation Research Board, Washington, D.C. (Froehlich, D.C.).

Vanoni, V.A., and Brooks, N.H. (1957). "Laboratory studies of the roughness and suspended load of alluvial streams." California Institute of Technology , Pasadena, CA.

Vanoni, V. A., et al. (1966). "Sediment transportation mechanics: Initiation of motion." J. Hydraul. Div. Am. Soc. Civ. Eng 92(2), 291-314.

U.S. Department of Agriculture, Natural Resources Conservation Service. (2007a) Fish Passage and Screening Design. National Engineering Handbook, part 654, Stream Restoration Design, Technical Supplement 14N. Washington, DC.

U.S. Department of Agriculture, Natural Resources Conservation Service. (2007b). Project Implementation. National Engineering Handbook, part 654, Stream Restoration Design, Chapter 15. Washington, DC.

Wallerstein, N.P., et al. (2001). “Distorted Froude-Scaled Flume Analysis of Large Woody Debris.” Earth Surface Processes and Landforms, 26(12), 1265–1283, doi:10.1002/esp.271.

Wallerstein, N. P. (2003). “Dynamic Model for Constriction Scour Caused by Large Woody Debris.” Earth Surface Processes and Landforms, 28(1), 49–68, doi:10.1002/esp.426.

Ward, C. (2006). "Engineered logjams: an alternative bank-protection method for US 101 along the Hoh River, Washington." Road Ecology Center.

Washington State Recreation and Conservation Office. (2012). “Deschutes River ELJ / LWD Design Project.” HWS, Thurston Conservation District (LE), 30 Nov. 2012, hws.ekosystem.us/project/150/17578.

Washington State Recreation and Conservation Office. (2000). “Elwha River Engineered Log Jams.” HWS, North Olympic Peninsula LE for Salmon, 31 May 2000, hws.ekosystem.us/project/180/10995.

Washington State Recreation and Conservation Office. (2011). “South Fork Nooksack (Mouth to Skookum Cr.) Restoration.” HWS, WRIA 1 Salmon Recovery Board (LE), 1 July 2011, hws.ekosystem.us/project/360/7004

White, F. M. (1994). "Fluid mechanics,” McGraw-Hill, New York.

Whitehouse, R. J. S. (1997). "Scour at marine structures: a manual for engineers and scientists." Res. Rep. SR417, HR Wallingford Limited, Wallingford, UK, 216p.

Wolman, M.G. (1954). "A method of sampling coarse river-bed material." EOS, Transactions American Geophysical Union, 35(6), 951-956.

WSDOT. (2003). *Roadside Manual. Publication M25-30*. Washington State Department of Transportation.

WSDOT. (2010a). *Standard Specifications for Roads, Bridge, and Municipal Construction. Publication M41-10*. Washington State Department of Transportation.

WSDOT. (2010b). *Design Manual. Publication M22-01.07*. Washington State Department of Transportation.

WSDOT. (2010c). *Hydraulics Manual. Publication M23-03.03*. Washington State Department of Transportation.

WSDOT. (2011). *Biological Assessment State Route 20: Milepost 100 to 101 Skagit River Chronic Environmental Deficiency-Permanent Restoration*, Northwest Region Environmental Services Biology Program, Washington State Department of Transportation, January 2011.

Wu, B. and Molinas, A. (2005). Energy losses and threshold conditions for choking in channel contractions. Journal of Hydraulic Research, 43(2), 139-148.

Xu, Y. and Liu, X. (2017). “Effects of different in-stream structure representations in computational fluid dynamics models – taking engineered log jams (ELJ) as an example.” Water, 9(2), 110.

Yalin, M.S., and Karahan, E. (1979). "Inception of sediment transport." Journal of the Hydraulics Division, 105(11), 1433-1443.

Zang, Y., Street, R.L., and Koseff, J.R. (1994). “A non-staggered grid, fractional step method for time dependent incompressible Navier Stokes equations in curvilinear coordinates.” Journal of Computational Physics, 114(1), 18-33.

Zeller, J. (1963). Introduction into the sediment transport of open channels (Reprint). Switzerland. Bauzeitung, 81, 3-19.

Appendix A: Prototype ELJ and Revetment Details

Table A.1. Prototype log component volumes respective of dolotimber type.

Type	Prototype Log Description	Volume (ft^3)
a	24" DIA Log, 20' Long	62.83
b	18" DIA Log, 20' Long	35.34
c	18" DIA Log, 10' Long	17.67
d	18" DIA Log, 7' Long	12.37
e	16" DIA Log, 25' Long	34.91
f	16" DIA Log, 20' Long	111.70
g	12" DIA Log, 25' Long	78.54
h	12" DIA Log, 20' Long	62.83
i	6" DIA Log, 20' Long	15.71
j	16" DIA, 20' Long	111.70
l	6 - 4" DIA,18' Long	9.42
	5 - 8" DIA, 18' Long	31.42
	5 - 12" DIA, 18' long	70.69
	Racking Logs	111.53
m	18" DIA Log, 18' Long	31.81
n	4" DIA Log, 20' Long	1.75
o	8" DIA Log, 20' Long	6.98
p	12" DIA Log, 20' Long	15.71

Table A.2. Prototype ballast component volumes respective of dolotimber type.

Type	Ballast Component Description	Volume (ft^3)
T	8" streambed cobble	31.42
	70-4" DIA logs/bundle, 11' long	67.20
	26-6" DIA logs/bundle, 20' long	102.10
W	8" streambed cobble	62.83
V	8" streambed cobble	25.13
P	8" streambed cobble	94.25
P	LOGS 3-3.8' DIA ballasted racking bundles (log # for three bundles)	201.59
V	LOGS 1-3.8' DIA ballasted racking bundle	42.76
W	LOGS 2-3.8' DIA Ballasted racking bundle (log # for two bundles)	134.39

Table A.3. Prototype dolo component volumes from dimensioned construction drawings.

Component	Volume (ft^3)
Trunk	21.21
Fluke	75.68
Total	96.89

Table A.4. Prototype ELJ3 layering detail.

ELJ 3				
Layer 1				
Dolo Type	**Count**	**Dolo (Y/N)**	**Log**	
			Type	**Count**
A	5	Y	a	1
			b	1
B	91	Y	c	3
I	0	Y	c	2
			g	1
Layer 2				
Dolo Type	**Count**	**Dolo (Y/N)**	**Log**	
			Type	**Count**
B	24	Y	c	3
N	2	Y	c	2
T	0	Ballasted Bundle		
E	18	Y	h	1
			d	2
S	10	Y	e	1
J	4	Y	f	1
Q	7	Y	e	1
L	7	N	Racking Logs	
O	21	Y	d	2
W	7	Ballasted Bundle		
Layer 3				
Dolo Type	**Count**	**Dolo (Y/N)**	**Log**	
			Type	**Count**
H	0	Y	g	1
I	0	Y	c	2
			g	1
L	1	N	Racking Logs	
S	3	Y	e	1
J	2	Y	f	1

Table A.5. Prototype ELJ1 layering detail.

ELJ 1				
Layer 1				
Dolo Type	**Count**	**Dolo (Y/N)**	**Log**	
			Type	**Count**
A	1	Y	c	3
B	29	Y	c	2
P	0	Ballasted Bundle		
Q	0	Y	e	1
Layer 2				
Dolo Type	**Count**	**Dolo (Y/N)**	**Log**	
			Type	**Count**
B	18	Y	c	3
O	1	Y	d	2
P	7	Ballasted Bundle		
L	0	N	Racking Logs	
Q	6	Y	e	1
Layer 3				
Dolo Type	**Count**	**Dolo (Y/N)**	**Log**	
			Type	**Count**
E	0	Y	h	1
			d	2
J	1	Y	f	1
L	5	N	Racking Logs	
M	0	N	j	11
S	11	Y	e	1
V	5	Ballasted Bundle		

Table A.6. Prototype ELJ2 layering detail.

ELJ 2				
Layer 1				
Dolo Type	**Count**	**Dolo (Y/N)**	**Log**	
			Type	**Count**
A	3	Y	c	3
B	48	Y	c	2
Layer 2				
Dolo Type	**Count**	**Dolo (Y/N)**	**Log**	
			Type	**Count**
B	24	Y	c	3
O	8	Y	d	2
P	5	Ballasted Bundle		
E	4	Y	h	1
			d	2
Q	5	Y	e	1
Layer 3				
Dolo Type	**Count**	**Dolo (Y/N)**	**Log**	
			Type	**Count**
E	5	Y	h	1
			d	2
J	0	Y	f	1
L	7	N	Racking Logs	
M	0	N	j	11
S	17	Y	e	1
V	4	Ballasted Bundle		

Table A.7. Prototype Revetment 1 layering detail.

Revetment 1				
Layer 1				
Dolo Type	**Count**	**Dolo (Y/N)**	**Log**	
			Type	**Count**
A	3	Y	c	3
B	48	Y	c	2
D	42	Y	m	3
Layer 2				
Dolo Type	**Count**	**Dolo (Y/N)**	**Log**	
			Type	**Count**
B	21	Y	c	3
O	16	Y	d	2
C	21	Y	a	1
			i	1
E	21	Y	h	1
			d	2
K	16	N	f	3
M	5	N	n	4
			o	4
			p	3
Layer 3				
Dolo Type	**Count**	**Dolo (Y/N)**	**Log**	
			Type	**Count**
E	0	Y	h	1
			d	2
A	21	Y	c	3
H	21	Y	g	1
Y	0	N	j	11
S	0	Y	e	1
V	0	Ballasted Bundle		

Table A.8. Prototype Revetment 2 layering detail.

Revetment 2				
Layer 1				
Dolo Type	**Count**	**Dolo (Y/N)**	**Log**	
			Type	**Count**
A	21	Y	c	3
B	29	Y	c	2
D	34	Y	m	3
Layer 2				
Dolo Type	**Count**	**Dolo (Y/N)**	**Log**	
			Type	**Count**
H	1	Y	g	1
O	20	Y	d	2
T	10	Ballasted Bundle		
G	13	Y	a	1
			b	1
E	24	Y	h	1
			d	2
K	8	N	18" DIA	3
F	9	Y	b	2
Layer 3				
Dolo Type	**Count**	**Dolo (Y/N)**	**Log**	
			Type	**Count**
E	0	Y	h	1
			d	2
A	0	Y	c	3
H	0	Y	g	1
Y	0	N	j	11
S	0	Y	e	1
V	0	Ballasted Bundle		

Table A.9. Prototype Revetment 3 layering detail.

Revetment 3				
Layer 1				
Dolo Type	**Count**	**Dolo (Y/N)**	**Log**	**Count**
			Type	3
A	21	Y	c	2
B	41	Y	c	3
D	36	Y	m	
Layer 2				
Dolo Type	**Count**	**Dolo (Y/N)**	**Log**	
			Type	**Count**
H	27	Y	g	1
O	11	Y	d	2
T	8	Ballasted Bundle		
G	18	Y	a	1
			b	1
E	11	Y	h	1
			d	2
K	6	N	18" DIA	3
F	15	Y	b	2
A	3	Y	c	3
B	11	Y	c	2
L	3	N	Racking Logs	
M	4	N	n	4
			o	4
			p	3
Layer 3				
Dolo Type	**Count**	**Dolo (Y/N)**	**Log**	
			Type	**Count**
E	1	Y	h	1
			d	2
A	4	Y	c	3
D	1	Y	m	3
O	1	Y	d	2
S	0	Y	e	1
V	0	Ballasted Bundle		

Table A.10. Prototype Revetment 1 component breakdown and porosity.

Prototype Revetment 1			
Component	**Volume (ft^3)**	**Percent Structure Volume (%)**	
Cobble	0.0	0.0	
Logs	17782.2	46.2	
Dolos	20733.6	53.8	
Total Solids	38515.8	**Porosity**	78.6
Total Volume	180000.0		

Table A.11. Prototype Revetment 2 component breakdown and porosity.

Prototype Revetment 2			
Component	**Volume (ft^3)**	**Percent Structure Volume (%)**	
Cobble	314.2	1.1	
Logs	12426.6	45.4	
Dolos	14629.7	53.5	
Total Solids	27370.5	**Porosity**	76.8
Total Volume	117876.0		

Table A.12. Prototype Revetment 3 component breakdown and porosity.

Prototype Revetment 3			
Component	**Volume (ft^3)**	**Percent Structure Volume (%)**	
Cobble	251.3	0.7	
Logs	15738.4	44.4	
Dolos	19474.0	54.9	
Total Solids	35463.7	**Porosity**	80.8
Total Volume	185115.0		

Table A.13. Prototype ELJ1 component breakdown and porosity.

ELJ 1 Prototype			
Component	**Volume (ft^3)**	**Percent Structure Volume (%)**	
Cobble	785.4	8.2	
Logs	2271.8	23.8	
Dolos	6491.3	68.0	
Total Solids	9548.6	**Porosity**	78.6
Total Volume	44640.0		

Table A.14. Prototype ELJ2 component breakdown and porosity.

ELJ 2 Prototype			
Component	**Volume (ft^3)**	**Percent Structure Volume (%)**	
Cobble	571.8	3.4	
Logs	5228.4	31.0	
Dolos	11045.0	65.6	
Total Solids	16845.1	**Porosity**	77.2
Total Volume	73944.0		

Appendix B: Model ELJ and Revetment Details

Table B.1. Dimensions of model dolotimber ELJ components for volumetric calculations

Model Component Dimensions		
ELJ 3 Width	0.6329	ft
	7.5943	in
Dolo Width	1.2000	in
Trunk Length	0.4000	in
Trunk Diameter	0.4000	in
Trunk Volume	0.0503	in^3
Fluke Inner Diameter	0.1000	in
Fluke Outer Diameter	0.2000	in
Fluke Length	0.5150	in
Volume of Fluke	0.1510	in^3
Volume - Mid Fluke	0.0855	in^3
Dolo Volume	0.2867	in^3
Length of Logs	3.0000	in
Radius of Logs	0.1969	in
Volume of Logs	0.3652	in^3

Table B.2. Calculations of structure component percentage between prototype and model for ELJ3.

ELJ 3 Prototype			
Component	**Volume (ft^3)**	**Percent Structure Volume (%)**	
Cobble	440	1.4	
Logs	12024	39.3	
Dolos	18118	59.2	
Total Solids	30582	**Porosity**	72.0
Total Volume	109312		
ELJ 3 Model			
Component	**Volume (in^3)**	**Percent Structure Volume (%)**	
Logs	16.4	40.3	
Dolos	24.4	59.7	
Total Solids	40.8	**Porosity**	72.0
Total Volume	145.7		

Table B.3. **Calculations of structure component percentage between prototype and model for ELJ1.**

ELJ 1 Prototype			
Component	**Volume (ft^3)**	**Percent Structure Volume (%)**	
Cobble	785.4	8.2	
Logs	2271.8	23.8	
Dolos	6491.3	68.0	
Total Solids	9548.6	**Porosity**	78.6
Total Volume	44640.0		
ELJ 1 Model			
Component	**Volume (in^3)**	**Percent Structure Volume (%)**	
Logs	3.7	28.5	
Dolos	9.2	71.5	
Total Solids	12.8	**Porosity**	78.4
Total Volume	59.5		

Table B.4. Calculation of structure component percentage between prototype and model for ELJ2.

ELJ 2 Prototype			
Component	**Volume (ft^3)**	**Percent Structure Volume (%)**	
Cobble	571.8	3.4	
Logs	5228.4	31.0	
Dolos	11045.0	65.6	
Total Solids	16845.1	**Porosity**	77.2
Total Volume	73944.0		
ELJ 2 Model			
Component	**Volume (in^3)**	**Percent Structure Volume (%)**	
Logs	7.3	32.5	
Dolos	15.2	67.5	
Total Solids	22.5	**Porosity**	77.2

Table B.5. Calculation of model revetment porosity with proxy gravel.

Symbol	**Parameter**	**Location**		
		Revetment 1	**Revetment 2**	**Revetment 3**
n	Porosity [-]	0.785	0.765	0.807
d_{eff}	effective diameter (mm)	25	25	25
	effective diameter (m)	0.025	0.025	0.025
C_{SH}	shape factor [-]	9.5	9.5	9.5
τ	tortuosity {-}	2.5	2.5	2.5
C_{PK}	packing factor [-]	78.125	78.125	78.125
k	permeability (m^2)	9.28E-07	7.19E-07	1.25E-06
K	hydraulic conductivity (m/s)	9.08E+00	7.04E+00	1.22E+01

Appendix C: Estimating $C_{\alpha,p}$ from Bed Shear Stress

The amplification coefficient, α, is generically defined as:

$$Y_{\max,SC} = \alpha Y_{\max,LC} \tag{C1}$$

Long contraction equilibrium scour depth

First, bed shear stress is expressed as:

$$\tau = \frac{\rho g (Un)^2}{Y^{1/3}} \tag{C2}$$

Using equation (C2), the ratio of shear stresses between the approach section and the long contraction section is calculated as:

$$\frac{\tau_{ap}}{\tau_{LC}} = \frac{U_{ap}^2 / Y_{ap}^{1/3}}{U_{LC}^2 / Y_{LC}^{1/3}} \tag{C3a}$$

-or-

$$\frac{\tau_{ap}}{\tau_{LC}} = \left(\frac{U_{ap}}{U_{LC}}\right)^2 \left(\frac{Y_{LC}}{Y_{ap}}\right)^{1/3} \tag{C3b}$$

From continuity, we have $U_{ap} = Q/B_{ap}Y_{ap}$ and $U_{LC} = Q/B_C Y_{LC}$, which leads to:

$$\frac{\tau_{ap}}{\tau_{LC}} = \left(\frac{B_C}{B_{ap}}\right)^2 \left(\frac{Y_{LC}}{Y_{ap}}\right)^{7/3} \tag{C4a}$$

-or-

$$\frac{Y_{LC}}{Y_{ap}} = \left(\frac{\tau_{ap}}{\tau_{LC}}\right)^{3/7} \left(\frac{B_{ap}}{B_C}\right)^{6/7} \tag{C4b}$$

At equilibrium scour in the long contraction, we rewrite equation (C4b) by considering the maximum depth of flow at the long contraction, $Y_{max,LC}$, and by assuming $\tau_{LC} = \tau_{cr}$, which results in:

$$Y_{\max,LC} = Y_{ap} \left(\frac{\tau_{ap}}{\tau_{cr}}\right)^{3/7} \left(\frac{B_{ap}}{B_C}\right)^{6/7} \tag{C5}$$

Short contraction scour depth estimation

First, the following coefficient is defined to account for differences in shear stress between the short contraction and the long contraction at similar d_{sm}:

$$C_1 = \frac{\tau_{SC}}{\tau_{LC}} \tag{C6}$$

By making the appropriate substitution into equation (C4b), the following is determined

$$\frac{Y_{SC}}{Y_{ap}} = \left(C_1 \frac{\tau_{ap}}{\tau_{SC}} \right)^{3/7} \left(\frac{B_{ap}}{B_C} \right)^{6/7} \qquad \text{(C7)}$$

At equilibrium scour in a short contraction, the substitution $Y_{SC} = Y_{max,SC}$ is made and it is also assumed that $\tau_{SC} = \psi\tau_{cr}$ (where $\psi < 1$). This assumption is based on experimental findings that the equilibrium shear stress at localized scour is less than τ_{cr} due to the influences of strong vortex flow (Biron et al., 2004; Dey and Barbhuiya, 2005; Li, 2016). These substitutions yield:

$$Y_{\max,SC} = Y_{ap} \left(\frac{C_1}{\psi} \frac{\tau_{ap}}{\tau_{cr}} \right)^{3/7} \left(\frac{B_{ap}}{B_C} \right)^{6/7} \qquad \text{(C8a)}$$

-or-

$$Y_{\max,SC} = \left(\frac{C_1}{\psi} \right)^{3/7} \left[Y_{ap} \left(\frac{\tau_{ap}}{\tau_{cr}} \right)^{3/7} \left(\frac{B_{ap}}{B_C} \right)^{6/7} \right] \qquad \text{(C8b)}$$

Estimating $C_{\alpha,p}$ based on flow measurements

In order to allow scour depth predictions at a porous structure with the Ettema et al. (2010) formula, estimates are needed for the coefficient, $C_{\alpha,p}$, which is defined as:

$$C_{\alpha,p} = \frac{\alpha_p}{\alpha_{imp}} \qquad \text{(C9)}$$

Two methods for estimating $C_{\alpha,p}$ with flow measurements are considered herein. The first method is to estimate α_p from bed shear stress measurements made at equilibrium scour at a porous structure and then to compare this value with α_{imp}. This method requires a general equation for estimating α based on bed shear stress, which is developed by combining equations (C1), (C5) and (C8b), and expressing α as:

$$\alpha_p = \left(\frac{\tau_{SC,p}}{\psi\tau_{LC}} \right)^{3/7} \qquad \text{(C10)}$$

Thus, by estimating $\tau_{SC,p}$ from flow measurements near the porous structure and determining τ_{LC} from equation (2), α_p can be estimated using equation (C10).

The second method for estimating $C_{\alpha,p}$ is to directly compare the bed shear stresses estimates at both a permeable and an impermeable structure under otherwise identical conditions. The equation for estimating $C_{\alpha,p}$ in this manner is derived by applying equation (C10) to each α value in equation (C9) to find:

$$C_{\alpha,p} = \left(\frac{\tau_{SC,p}}{\tau_{SC,imp}} \right)^{3/7} \qquad \text{(C11)}$$

List of symbols:

$()_{ap}$ - quantity at the approach section
$()_{C}$ - quantity at the contracted section
$()_{imp}$ - quantity at an impermeable structure
$()_{p}$ - quantity at a permeable structure
$()_{LC}$ - quantity at a long contraction
$()_{SC}$ - quantity at a short contraction
B - channel width
C_1 - ratio of bed shear stress at a short contraction to the bed shear stress at a long contraction with identical scour depth
$C_{\alpha,p}$ - coefficient for correcting α to account for structure porosity
g - acceleration of gravity
n - Manning's roughness coefficient
Q - flow discharge
U - bulk velocity
Y - flow depth (including depth of scour at the contracted section)
Y_{max} - maximum flow depth at equilibrium scour
α - bed shear stress amplification coefficient
ρ - fluid density
τ - bed shear stress